

Human models of Parkinson's disease present
impaired autophagy, mitophagy and mitochondria
energy metabolism

Jonathan ARIAS

ジョナサン・アリアス

氏名

目次 Table of Contents

略語表 Abbreviation	9
要旨 Abstract	15
第一章 Chapter 1 序論 Introduction	17
1-1 遺伝的多様性 Genetic diversity	20
1-2 表現型 Phenotype modulation	21
1-3 パーキンソン病 Parkinson's disease	22
1-4 α -シヌクレイン α -Synuclein	23
1-5 Vacuolar protein sorting-associated protein 35 - VPS35	24
1-6 Leucine-rich repeat serine/threonine-protein kinase 2 - LRRK2	25
1-7 PTEN-induced putative kinase 1 - PINK1	26
1-8 オートファジー Autophagy	27
1-9 マイトファジーMitophagy	28
1-10 人工多能性幹細胞 - iPS 細胞 Human induced pluripotent stem cells – iPS cells	30
1-11 神経上皮幹細胞 – NESCs Neuroepithelial stem cells – NESCs	32
1-12 ゲノム編集 Genome editing	33
1-13 pHluorin and Rosella	34
1-14 Extracellular energy flux analysis	35

1-15 Automated high-throughput and high-content image acquisition and analysis	37
第二章 Chapter 2 結果 1 - Results 1	39
2-1 Genetically-encoded Rosella-LC3 and ATP5C1-Rosella systems allow for the visualization of the complete autophagy and mitophagy pathways	41
2-2 3D reconstruction of reporter lines confirms complete reconstruction of autophagy and mitophagy pathways	44
2-3 Human iPS cells present dynamic autophagy activity	47
2-4 Human iPS cells present a dynamic mitochondria network and mitophagy activity	50
2-5 Generation of image analysis algorithms to identify autophagy structures	53
2-6 Generation of image analysis algorithms to identify mitochondria and mitophagy structures.....	58
2-7 Generation of image analysis algorithms to identify lysosomes	61
2-8 PD-mutant lines present a reduced autophagy capacity in basal conditions.....	64
2-9 PD-mutant lines present an impaired autophagy reaction constant	67
2-10 Responsiveness of reporter lines to autophagy and mitophagy modulation ..	70
2-11 Differential phagophore responsiveness to autophagy blockage	73
2-12 Regulation of phagophore upstream pathways: CaMK- β /AMPK and mTOR..	76
2-13 Evaluation of mitophagy contribution to general autophagy	80
2-14 Definition of autophagy fingerprints in control and PD mutants	84
2-15 Quantification of mitochondria network and mitophagic vacuole volume	87

2-16 Evaluation of the mitophagy levels	90
2-17 Distribution of autophagy resources upon mitochondrial stress: mitophagy, non-mitochondrial autophagy, and general autophagy	93
2-18 Evaluation of lysosome capacity in control and mutant lines	96
第三章 Chapter 3 結論及び考察 1 - Conclusion & Discussion 1	99
第四章 Chapter 4 結果 2 - Results 2	107
4-1 Fluorescent proteins – SNP pairs enable achievement of deterministic genotype outcomes	109
4-2 Similar reporter expression levels are achieved in different genomic regions	113
4-3 Repetitive elements reduce on-target genome editing efficiency by increasing random integration	116
4-4 FACS purification increases speed and yield of isogenic derivation	120
4-5 Transposase-mediated generation of footprint-free isogenic lines	123
4-6 Edited polyclones preserve genome stability and pluripotency properties	127
4-7 Human iPS cell derived NESCes express α -Synuclein	130
4-8 SNCA mutants present reduced mitochondrial performance	133
第五章 Chapter 5 結論及び考察 2 - Conclusion & Discussion 2	137
第六章 Chapter 6 材料及び方法 Materials and Methods	143
6-1 Human iPS cell culture, electroporation and selection	145
6-2 Polyclones composition characterization	145
6-3 NESCes differentiation and culture	146

6-4 Extracellular energy flux analysis	146
6-5 Cloning of sgRNA containing vectors and donor vectors.....	147
6-6 Autophagy and mitophagy reporter platform.....	147
6-7 In-vitro RNA transcription and mRNA transfection	148
6-8 Pathway contribution dissection	148
6-9 Lysosome quantification and nuclear contrast	149
6-10 FACS analysis	149
6-11 Time-lapse live cell imaging	149
6-12 Microscopy for Rosella-LC3, ATP5C1-Rosella, and Lysotracker	150
6-13 Image analysis for Rosella-LC3 autophagy, ATP5C1-Rosella mitophagy assay and Lysotracker assay	150
6-14 mRNA Microarray	151
6-15 Microarray Karyotype	151
6-16 Immunostaining	151
6-17 Western Blotting	152
文献 Bibliography	153
謝辭 Acknowledgment.....	167

略語表

Abbreviations

Adenosine diphosphate (ADP)

Adenosine triphosphate (ATP)

Adeno-associated virus integration site 1 (AAVS1)

Alpha-Synuclein, α -Synuclein (SNCA)

Ataxia telangiectasia mutated erine/threonine kinase (ATM)

ATP synthase, proton transporting, mitochondrial F1 complex, γ polypeptide 1 (ATP5C1)

Bone morphogenetic protein (BMP)

Calcium/calmodulin dependent protein kinase II β (CaMK- β)

Carbonyl cyanide m-chlorophenyl hydrazone (CCCP)

Cation independent mannose 6 phosphate receptor (CIMPR)

Ceroid lupofuscinosis 3 (CLN3)

Clustered regulatory interspersed short palindromic repeats Cas9 (CRISPR-Cas9)

Coding sequence (CDS)

Copy number variants (CNV)

Diisopropyl fluorophosphate (DFP)

Dimethyl sulfoxide (DMSO)

Discosoma sp. red fluorescent protein (DsRED)

DNA cross-link repair 1C (DCLRE1C)

Double stranded DNA (dsDNA)

DsRED-pHluorin fusion protein (Rosella)

Earle's balanced salt solution (EBSS)

Estrogen receptor 2 (ESRB)

FACS assisted CRISPR-Cas9 genome editing (FACE)

Fluorescent activated cell sorting (FACS)

Forward scattering (FSC)

F-box only protein 7 (FBX07)

Genome wide association studies (GWAS)

Glycogen synthase kinase 3 β (GSK3- β)

Homology directed repair (HDR)

Induced pluripotent stem (iPS)

Insertion or deletion (indel)

IGF2R insulin like growth factor 2 receptor (CIMPR)

Knock in (KI)

Kruppel like factor 2 (KLF2)

Kruppel like factor 4 (KLF4)

Leucine-rich repeat serine/threonine-protein kinase 2 (LRRK2)

Ligase IV (LIGIV)

Long interspersed nuclear element (LINE)

Long terminal repeat (LTR)

Mechanistic target of rapamycin (mTOR)

Microtubule associated protein 1 light chain 3 alpha (LC3)

Mitofusin 2 (MFN2)

Mitogen-activated protein kinase 1 (ERK)

Mitogen-activated protein kinase kinase 7 (MEK)

MRE11 homolog, double strand break repair nuclease (MRE11)

MRN (MRE11, RAD50 and Nbs1)

MRN complex interacting protein (MRNIP)

Nicotinamide adenine dinucleotide (NAD)

NAD protonated (NADH)

Nanog homeobox (NANOG)

NBN nibrin (NBN)

Nestin intermediate filament (NESTIN)

Neuroepithelial stem cell (NESC)

Non-homologous end joining (NHEJ)

Non-homologous end joining factor 1 (NHEJ1)

Numerical aperture (NA)

Parkin (PRKN)

Parkinson's disease (PD)

Proton concentration responsive green fluorescent protein (pHluorin)

Protospacer adjacent motif (PAM)

POU class 5 homeobox 1 (OCT4)

Probable cation-transporting ATPase 13A2 (ATP13A2)

Protein deglycase DJ-1 (PARK7)

Protein kinase AMP-activated catalytic subunit α 1 (AMPK)

Protein kinase, DNA-activated, catalytic polypeptide (PRKDC)

Puromycin resistance CDS (Puro)

RAD50 double strand break repair protein (RAD50)

RAD51 recombinase (RAD51)

Ras homolog family member T1 (RHOT1)

Reactive oxygen species (ROS)

Replication protein A1 (RPA1)

Serine/threonine-protein kinase PTEN-induced putative kinase 1 (PINK1)

Short interspersed element (SINE)

Side scattering (SSC)

Single nucleotide polymorphisms (SNP)

Single-nucleotide variants (SNV)

SMAD family member (SMAD)

Sodium-dependent dopamine transporter (SLC6A3)

Sonic hedgehog (SHH)

SRY-box 1 (SOX1)

SRY-box 2 (SOX2)

Standard deviation (SD)

Substantia nigra (SN)

Synthetic guide RNA (sgRNA)

T-box 3 (TBX3)

Transcription activator-like effector nucleases (TALEN)

Transcription initiation factor TFIID subunit 1 (TAF1)

Unc-51 like autophagy activating kinase 1 (ULK1)

Vacuolar protein sorting-associated protein 26 (VPS26)

Vacuolar protein sorting-associated protein 29 (VPS29)

Vacuolar protein sorting-associated protein 35 (VPS35)

Wild type (WT)

Wingless family member (WNT)

X-ray repair complementing defective repair in Chinese hamster cells 4 (XRCC4)

X-ray repair complementing defective repair in Chinese hamster cells 5 (XRCC5)

X-ray repair complementing defective repair in Chinese hamster cells 6 (XRCC6)

Zinc-finger nucleases (ZFN)

要旨

Abstract

Neuronal models for human neurodegenerative diseases are of critically important to understand pathologies in central nervous system cells of all types, with inherent restricted accessibility. Parkinson's disease is second most prevalent neurodegenerative disease worldwide. This pathology imposes a large economic burden in patients and families that suffer from it. Parkinson's disease is a multifactorial genetic and environmentally-induced pathology. The genetic factors that most significantly influence its phenotypic outcome has been defined to ten genes. These genes affect multiple cellular processes, but they have common factors such as inducing a reduction in protein homeostasis. These impairments are manifested by the accumulation of protein aggregates in the midbrain region substantia nigra pars compacta. The protein aggregates have been attributed as both the cause and the result of the selective degeneration in the substantia nigra and associated neuronal paths of the brain. In the present work three components are studied that reduce protein homeostasis, namely autophagy, mitophagy and mitochondria energy metabolism. These pathways are analyzed for Parkinson's disease-associated mutants in the genes *LRRK2*, *VPS35*, *PINK1* and *SNCA*. Using human induced pluripotent stem cells, neuroepithelial stem cells, as well as genome editing tools and reporter systems, is demonstrated that Parkinson's disease mutants not only share autophagy, mitophagy and mitochondria energy metabolism impairments, but they also present a characteristic fingerprint that classify them and define the pathways that modulate their phenotype.

第一章

Chapter 1

序論

Introduction

The present section will introduce the concepts of genetic diversity (section 1-1), how the genetic variant composition results in phenotype modulation (section 1-2), and an example of pathogenic genetic variants that result in neurodegeneration, namely PD (section 1-3). A subset of the genes involved in PD pathology, including *SNCA* (section 1-4), *VPS35* (section 1-5), *LRRK2* (section 1-6), and *PINK1* (section 1-7). The pathways of autophagy (section 1-8), and mitophagy (section 1-9) will be introduced, taking into account how they are affected during PD. Then, cellular models used for early development disease modelling, such as human iPS cells (section 1-10), and NESCes (section 1-11). Next, strategies for genome editing (section 1-12) in order to achieve isogenic disease models, and the development of genetically encoded pH sensors pHluorin and Rosella (section 1-13). Finally, an overview of extracellular energy flux analysis and its relation to mitochondria electron transport chain (section 1-14) and a summary of the technologies for automated high-throughput and high-content analysis (section 1-15), will be covered in this introduction.

1-1 遺伝的多様性

Genetic diversity

Genetic diversity in human population is composed by combinations of at least 15 million SNVs and CNVs (Genomes Project et al., 2010). Such variations include coding sequence and non-coding sequence variations (Shiina et al., 2006; Zhang and Lupski, 2015). First, coding sequence variants can result in (i) missense (ii) nonsense or (iii) silent mutations. Missense mutations lead to changes in amino acid sequence. Mutant amino acid chains different in their physicochemical properties can result in protein misfolding, loss of function or emergent functions (Valastyan and Lindquist, 2014). Nonsense mutations lead to stop codons, and produce truncated proteins. The truncated proteins can miss structural domains, which affects their function or subcellular localization (Hogervorst et al., 1995). Silent mutations affect the nucleotide sequence yet result in the same amino acid sequence. Second, non-coding mutations can affect transcriptional regulatory regions (Melton et al., 2015), non-coding RNA regulatory sequences (Khurana et al., 2016), splicing regulatory regions (Ward and Cooper, 2010) or non-functional sequences.

1-2 表現型

Phenotype modulation

Phenotype can be represented as a multifactorial function composed of the partial contribution of all polymorphism variants. Polymorphism variants can enhance or decrease this phenotype output. Polymorphic variants that enhance the phenotype output are called risk factors (Liou et al., 2016), while variants that decrease the phenotype output are called protective factors (Wirdefeldt et al., 2005). Then, polymorphism composition modulates the phenotype output of an organism and its cellular model. Hence, the composition of polymorphic variants play a critical role when comparing cellular models from different genetic backgrounds (Kalinderi et al., 2016). Comparison of cellular models does not only compare a genotype of interest, but also the known and unknown, risk or protective factors of that defined model. The diversity in human genome and the variability of polymorphisms make necessary the use of cellular models that share the same genetic background – isogenic cellular models (Ryan et al., 2013). In that way, the phenotype observed can be attributed exclusively to the genetic difference studied. Here are developed isogenic models for PD-associated mutations in the *SNCA* gene.

1-3 パーキンソン病

Parkinson's Disease

PD is a neurodegenerative disorder characterized by non-motor and motor symptoms. The non-motor symptoms include sleep disorders, cognitive changes, mood disorders and hallucinations. The motor symptoms include postural instability, rigidity, resting tremor and bradykinesia (Barker et al., 2015; Lotharius and Brundin, 2002). PD patients can be diagnosed as sporadic or familial - genetically defined. In sporadic cases, the genetic cause is unknown with the disease resulting from exposure to environmental insults. Familial or genetically-defined PD cases can be attributed to at least 18 defined genes. These genes include *SNCA* (Polymeropoulos et al., 1997), *LRRK2* (Funayama et al., 2002; Paisan-Ruiz et al., 2004; Zimprich et al., 2004), *VPS35* (Lesage et al., 2012; Sharma et al., 2012a; Sheerin et al., 2012; Vilarino-Guell et al., 2011; Zimprich et al., 2011), *SLC6A3* (Kurian et al., 2009), *PINK1* (Valente et al., 2004; Valente et al., 2001), *PARK7* (van Duijn et al., 2001), *ATP13A2* (Ramirez et al., 2006), *FBX07* (Di Fonzo et al., 2009; Paisan-Ruiz et al., 2010), *PRKN* (Kitada et al., 1998) and *TAF1* (Graeber and Muller, 1992; Lee et al., 1991). GWAS demonstrate that at least 28 loci modulate the onset and phenotype strength of PD (Do et al., 2011; Edwards et al., 2010; Hamza et al., 2010; Hernandez et al., 2012; International Parkinson Disease Genomics et al., 2011; Lill et al., 2012; Nalls et al., 2014; Pankratz et al., 2012; Pankratz et al., 2009; Saad et al., 2011; Satake et al., 2009; Sharma et al., 2012b; Simon-Sanchez et al., 2011). Here are studied the cellular phenotypes for PD associated mutations in the genes *SNCA*, *VPS35*, *LRRK2* and *PINK1*.

1-4 SNCA, α -シヌクレイン

SNCA, α -Synuclein

In physiological conditions, α -Synuclein is located in the presynaptic terminal and vesicles of neurons. α -Synuclein is involved in synaptic transmission, fusion of membranes, exocytosis, endocytosis and regulation of vesicle curvature (Lautenschlager et al., 2017). In PD, aggregates of α -Synuclein are observed in SN dopaminergic neurons. α -Synuclein aggregates can be classified as Lewy bodies and Lewy neurites (Goedert et al., 2013). α -Synuclein mutations in PD patients have been described in familial early onset cases. *SNCA* mutations are autosomal dominant, they include and increase in gene dosage (Devine et al., 2011) and the missense mutations *SNCA* p.A30P (Kruger et al., 1998), *SNCA* p.E46K (Zarranz et al., 2004), *SNCA* p.H50Q (Proukakis et al., 2013), *SNCA* p.G51D (Lesage et al., 2013) and *SNCA* p.A53T (Polymeropoulos et al., 1997). These mutations disrupt the KTKEGV repeat motifs interactions (Dettmer et al., 2015b) and affect α -Synuclein native conformation. α -Synuclein is present as tetramers in its native conformation (Bartels et al., 2011). Tetramers are dependent on KTKEGV repeat motifs. Mutations in the repeat motifs modify the balance from tetramer to monomer form (Dettmer et al., 2015a). The tetramer and monomer are abundant in alpha helix structures, as demonstrated by circular dichroism experiments (Bartels et al., 2011; Luth et al., 2015). In pathological conditions, the alpha helix rich monomer shifts to a beta rich structure (Luth et al., 2015), which in turn acts as a template for further unfolding of native monomers in a process similar to amyloidogenic crystal seeds.

1-5 Vacuolar protein sorting-associated protein 35 - VPS35

VPS35 is a core member protein of the retromer complex. The retromer complex core members include VPS26, VPS29, and VPS35. The retromer complex is a structure essential for the formation of the retromer. The retromer is a membrane-composed structure responsible for sorting and recycling vesicular cargo (Seaman, 2004). Transport is mediated between the late endosome, trans Golgi network, endoplasmic reticulum (Tang et al., 2015) and cell membrane (Tabuchi et al., 2010). The vesicular mobilization mediated by the retromer facilitates the recycling of membrane-bound receptors such as CIMPR. Importantly, some of the retromer receptors transport mediators of protein degradation such as the lysosomal acid hydrolase enzyme cathepsin D. Hence, VPS35 plays a central role in the modulation of intracellular vesicle trafficking and of autophagy (Zavodszky et al., 2014). VPS35 alterations have been associated with multiple neurodegenerative diseases such as Alzheimer's disease, Ceroid lipofuscinosis and PD. Mutations in VPS35 protein were first identified in a late onset PD kindred (Vilarino-Guell et al., 2011), and thereafter regarded as one of the well-defined factors inducing PD.

1-6 Leucine-rich repeat serine/threonine-protein kinase 2 - LRRK2

LRRK2 protein is a highly ubiquitous and large protein consisting of six structural domains. It contains a central tridomain composed of: 1) Ras of complex GTPase, 2) carboxy-terminal of Roc, and 3) kinase domain (Mata et al., 2006). All pathological mutations on LRRK2 are located within the central tridomain region, and present segregation in a Mendelian manner. Such observations suggest that pathology induced by LRRK2 is restricted to its enzymatic activity modification (Cookson, 2010). LRRK2 protein exerts its function as a dimer complex (Berger et al., 2010; Greggio et al., 2008). Furthermore, the dimerization properties of LRRK2 enable its self-regulation through the kinase domain. LRRK2 has been shown to be an interacting partner for multiple cellular processes including cytoskeleton assembly with tubulin, protein translation, cellular trafficking with Rab7, and response to protein misfolding with heat shock proteins (Cookson, 2015). Importantly, LRRK2 interacts with two proteins linked to pathological mechanisms - microtubule-associated protein tau and α -Synuclein (Cookson, 2010). LRRK2 has been associated with the endosomal pathway (Steger et al., 2016) and the transition between the early and late endosome, converging in the lysosomal pathways (Roosen and Cookson, 2016). Hence, those studies linked LRRK2 function with control of autophagy and cellular homeostasis. Mutations in LRRK2 have been directly associated to neurodegeneration in PD (Funayama et al., 2002; Paisan-Ruiz et al., 2004; Zimprich et al., 2004), and regarded as a risk modulator in Gaucher's disease (Woodard et al., 2014).

1-7 PTEN-induced putative kinase 1 - PINK1

PINK1 protein kinase plays essential roles in mitochondrial surveillance. The monitoring aspects include regulation of mitochondria network dynamics, mitochondria maintenance (Bertolin et al., 2015), removal of damaged mitochondria fragments (McLelland et al., 2016), local protein translation (Gehrke et al., 2015), mitophagy (Jin and Youle, 2012), and mitochondria biogenesis (Mouton-Liger et al., 2017). PINK1 presents a mitochondria targeting sequence, single transmembrane helix and kinase domain. Upon loss of mitochondrial membrane potential, it is translocated to the inner mitochondria membrane and degraded (de Vries and Przedborski, 2013). Active PINK1 interacts with PARKIN and phosphorylates it (Koyano et al., 2014). PARKIN phosphorylation promotes its E3 ubiquitin ligase activity, and activation of mitophagy (Georgakopoulos et al., 2017). Furthermore, active PINK1 and PARKIN promotes mitochondria release from the cytoskeleton through RHOT1 degradation (Wang et al., 2011). In addition, PINK1 and PARKIN promote mitochondria fission through degradation of MFN2 (Chen and Dorn, 2013). Mutations in PINK1 result in increased accumulation of mitochondrial damage. As consequence of such accumulation, intracellular ROS generation is continuous (Requejo-Aguilar et al., 2014) and mitochondria energy performance hindered. Both aspects are a consequence of mutant PINK1-induced mitophagy impairments (Allen et al., 2013). Mutations on PINK1 that result in its loss of function have been directly linked to neurodegeneration in PD (Valente et al., 2004; Valente et al., 2001).

1-8 オートファジー

Autophagy

The term autophagy is derived from the Greek words *self* (*autos*) and *eat* (*phagein*). It refers to the cellular process in which intracellular material is degraded during normal development or disease. Pioneering studies first identified autophagy in yeast models (Takeshige et al., 1992). In human physiological conditions, different cell types adjust their intracellular composition by autophagy (Kundu et al., 2008). In addition, autophagy participates in maintaining a basal level of protein turnover that can account for 2% per hour in stem cells (Mizushima and Klionsky, 2007; Mizushima et al., 2001). Upon environmental insults, cells can be subjected to oxidative stress resulting in the accumulation of damaged cellular components (Poillet-Perez et al., 2015). The intracellular structures involved in autophagy are phagophores, autophagosomes, autolysosomes and lysosomes. Phagophore membranes are nucleated and assembled by the ATG family of proteins (Abreu et al., 2017). The first step towards the generation of the phagophore complex is the activation cleavage of LC3 (Mizushima and Klionsky, 2007). Phagophores are subjected to membrane enclosure that engulf the protein and lipid components aimed for degradation (Karanasios et al., 2016). The double membrane autophagosomes and autophagic cargoes fuse to lysosomes, giving rise to autolysosomes (Tooze and Yoshimori, 2010). The autolysosomes present an acidified luminal space and abundant hydrolases that enable disassembly. Subsequently, the luminal proteins of autolysosomes are degraded and recycled. Mutations in proteins involved in autophagy have been reported in conjunction with multiple neurodegeneration diseases, such as Alzheimer and Huntington's disease (Jiang and Mizushima, 2014; Levine and Kroemer, 2008). In this work, autophagy is assessed in the context of PD using LC3 fusion reporters.

1-9 マイトファジー

Mitophagy

Mitophagy is the selective engulfment of a mitochondrion or mitochondrial fragments by the autophagic machinery (Jin and Youle, 2012). During physiological conditions and development, mitochondria are degraded in order to adjust their numbers to specific cellular requirements (Kundu et al., 2008). As part of their ATP-producing function or environmental insults, mitochondria can be subjected to oxidative stress, resulting in damage of structural proteins and lipids (Kim et al., 2007). A set of regulatory mechanisms exists to monitor the oxidative levels and protein integrity. Upon detection of loss in membrane-potential, a degradative response is activated that includes the PARKIN-dependent ubiquitination of integral transmembrane proteins (Narendra et al., 2008), PINK1-dependent phosphorylation of regulatory proteins and the disassembly of the microtubule anchorage. Mitochondrial surface proteins tag parts of the mitochondrion for degradation. The selected fraction of the mitochondrion is excised from the mitochondrial network and incorporated into the autophagic pathway (Narendra et al., 2008). Thus, mitophagy is a sub-group of autophagic events restricted to degrading mitochondria or their components. Upon integration of mitochondrial cargoes into the autophagosome lumen, lysosomes are fused releasing hydrolases, and the luminal pH decreases. Upon lysosome fusion, the autophagosome is called an autolysosome. The early autolysosome continues to degrade its luminal cargo and its internal membrane, progressing to a mature late autolysosome. Mutations that affect mitochondrial homeostasis and mitophagy result in metabolic and degeneration pathologies. PD has been associated with mutations in PINK1, which, as described above, is involved in

mitophagy regulation (Pickrell and Youle, 2015). In this work, mitophagy in the context of PD is assessed using mitochondrial fusion reporters.

1-10 人工多能性幹細胞 – iPS 細胞

Human induced pluripotent stem cells – iPS cells

Pluripotent stem cells are a transient population during early embryo development. In humans, cells from the embryo inner cell mass present a pluripotent naive state (Nichols and Smith, 2009). The inner cell mass differentiates into a disk-like structure that gives rise to the epiblast and hypoblast. The epiblast presents a reduced degree of pluripotency level called primed state (Nichols and Smith, 2009). Successively, the epiblast gives rise to all the tissues from the embryo proper. The assistance of mouse models enabled the derivation of the first embryonic stem cells from the inner cell mass (Evans and Kaufman, 1981; Martin, 1981). Embryonic stem cells are defined operationally by their ability to derive all germ layers *in vitro* or *in vivo* (Martin, 1981). The culture of conventional mouse ground state naive stem cells require the use of LIF (Yoshida et al., 1996), ERK/MEK inhibitors (Burdon et al., 1999) and GSK3- β inhibitor (Ying et al., 2008). The human *in vitro* equivalent of inner cell mass-derived mouse naive stem cells has been achieved only recently (Gafni et al., 2013; Takashima et al., 2014; Theunissen et al., 2014). The minimal key transcriptional factors required to induce the conversion from terminally differentiated cells to primed pluripotent stem cells in mice (Takahashi and Yamanaka, 2006), and in humans (Takahashi et al., 2007) have been identified. Accordingly, the transcription-factors converted stem cells have been called induced pluripotent stem cells or iPS cells (Takahashi et al., 2007; Takahashi and Yamanaka, 2006). The transcriptional network controlling pluripotency has been extensively characterized, and the key regulator proteins defined as NANOG, SOX2, OCT4, KLF4, KLF2, TBX3 and ESRRB (Takashima et al., 2014; Yu and Thomson, 2008). A multitude of studies have used iPS cells for mechanistic, early developmental model and disease modelling studies. Importantly, such

studies include mature neuronal (Kriks et al., 2011), and early neuronal (Reinhardt et al., 2013) disease models. Similarly, in this work iPS cells are used for disease modelling in the context of PD.

1-11 神經上皮幹細胞 - NESCs

Neuroepithelial stem cells - NESCs

Neuronal progenitors relate to the neuronal plate and neural tube stage of embryo development (Conti and Cattaneo, 2010). There is a multitude of *in vitro* models of neuronal progenitors. Such *in vitro* models correlate to different temporal stages, and hallmarks of neuronal development. The current neuronal progenitor models can be classified as: primitive neuroepithelial progenitors (Smukler et al., 2006), neuronal rosette cells (Elkabatz et al., 2008), primitive neural stem cells (Li et al., 2011), radial glial-like cells (Bibel et al., 2007), and NESCs (Reinhardt et al., 2013). Neuronal progenitors are of great value for disease modeling and as a source of biological material equivalent to early neuronal development. Access to such *in vivo* material is ethically restricted and limited. Additionally, neuronal progenitors provide an experimental source for the generation of mature neurons (Reinhardt et al., 2013). NESC derivation from human iPS cells is based on the addition of a set of small-molecule inducers of neuronal lineage. Those modulators result in SMAD pathway inhibition (Chambers et al., 2009), BMP pathway inhibition (Kim et al., 2010), WNT pathway activation by GSK3- β inhibitor (Chambers et al., 2012), and SHH pathway activation by a SHH agonist (Chen et al., 2002; Sinha and Chen, 2006). NESCs are characterized by the expression of neuronal progenitor markers SOX1, SOX2 and NESTIN (Reinhardt et al., 2013). NESCs are used in the present work as an early neurodevelopmental disease model.

1-12 ゲノム編集

Genome editing

The advent of genome editing tools such as ZFN (Soldner et al., 2011), TALEN (Ding et al., 2013) and CRISPR-Cas9 (Mali et al., 2013) have enabled targeting nucleases to specific genomic regions to induce dsDNA breaks. Events of dsDNA breaks can be resolved through NHEJ or HDR. The NHEJ repair mechanism is dependent on protein complexes XRCC5, XRCC6, MRN (MRE11, RAD50 and NBN)-complex, PRKDC, DCLRE1C, NHEJ1, XRCC4 and LIGIV. The HDR repair mechanism is dependent on protein complexes of ATM, MRNIP, RAD51, RPA1 and dsDNA template. NHEJ results in high frequency indel events (Lei et al., 2012). HDR results in high frequency sequences with high identity (Chu et al., 2015). The NHEJ process can be used to harvest gene knock-out engineered lines, while HDR can serve the derivation of precise transversion or transition mutant lines. Hence, combinations of precise nucleases like ZFN, TALEN or CRISPR-Cas9 with dsDNA templates enable the modification of the genome to introduce polymorphism variants. This enables the generation of isogenic cellular models (Miyaoaka et al., 2014). This study used CRISPR-Cas9 nuclease for the generation of *SNCA* isogenic mutants.

1-13 pHluorin and Rosella

The use of fluorescent proteins has enabled a multitude of developments in cellular biology. They include cell tracing (Cai et al., 2013; Livet et al., 2007), cell tracking (Hatta et al., 2006), subcellular localization (Rizzo et al., 2009), gene activity (Theunissen et al., 2014), protein conformational changes (Aoki et al., 2008), and protein-protein interaction (Frommer et al., 2009; Kenworthy, 2001). The structural characterization of the chromophore component and their environment allowed the generation of synthetic variants with shifted absorbance or emission wavelength (Bindels et al., 2017). Furthermore, point mutation studies have enabled the generation of monomer, smaller, and tandem dimer variants (Shaner et al., 2005). Importantly, the quantum yield of the chromophore can be affected by the proton concentration of the internal barrel. This enabled the generation of pH-responsive fluorescent proteins (Miesenbock et al., 1998; Shen et al., 2014). Furthermore, the addition of targeting sequences enabled restricting the spatial location of the fluorescent proteins. Targeting sequences for all organelles and membranes have been successfully used (Rizzo et al., 2009). Of special relevance to autophagy and mitophagy are the phagophore and mitochondria targeting sequences LC3 and ATP5C1 proteins (Sankaranarayanan et al., 2000; Tanida et al., 2014). The fusion of the targeting sequence of LC3 or ATP5C1 with DsRED-pHluorin Rosella enabled the generation of a traceable pH sensor (Sargsyan et al., 2015). In this work, Rosella reporters are used for the generation of stable lines in conjunction with genome editing tools.

1-14 Extracellular energy flux analysis

Extracellular energy flux analysis is a widely accepted assay to define mitochondria performance in cellular models (Cooper et al., 2012; Ryan et al., 2013). It is based on the sequential blockage of the mitochondria complexes. The mitochondria complexes are an integral part of the electron transport chain of mitochondria. The electron transport chain plays a crucial role in cellular energy generation. This is represented as a proton gradient, ATP production and fumarate production. The mitochondria electron transport chain is composed of five complexes. Complex-I is a NADH-ubiquinone oxidoreductase, responsible for transferring electrons from NADH to the ubiquinone carrier. Additionally, it transfer protons across the membrane creating a proton gradient (Zhu et al., 2016), and can be inhibited by rotenone. Complex-II is a succinate dehydrogenase coupled to the citric acid cycle. Complex-II catalyzes the conversion from succinate to fumarate (Sun et al., 2005). Complex-III is a cytochrome BC1 complex. Complex-III transfer electrons from the ubiquinone QH₂ to cytochrome C. In addition, it transfer protons across the membrane contributing to the proton gradient (Solmaz and Hunte, 2008). Complex-III can be inhibited by antimycin A. Complex-IV is a cytochrome C oxidase. Complex-IV transfer electrons from cytochrome C to molecular oxygen, and contributes to the creation of the proton gradient (Yoshikawa et al., 1998). Complex-V is an ATP-synthase responsible for coupling the proton gradient dissipation with the generation of ATP from ADP and inorganic phosphate (Jonckheere et al., 2012). Complex-V can be inhibited with oligomycin. An additional component of the electron transport chain is the mitochondrion inner membrane, which maintains the proton gradient created by complex-I, complex-III and complex-IV. The impermeability of the membrane is essential for energy efficiency. The ionophore CCCP can disrupt the membrane potential by dissipating the

proton gradient. Hence, CCCP can uncouple this gradient generation from ATP synthesis. Therefore, as described above, there are four steps in which the electron transport chain can be modulated to evaluate mitochondria performance. The sequential blockage of complex-V, the membrane potential, complex-I and complex-III allow for deriving important conclusions about the cellular state. These parameters are the non-mitochondrial respiration, basal respiration, maximal respiration, proton leak, ATP production capacity, spare respiratory capacity, acute response and coupling efficiency. The sequential steps described above are the root of extracellular energy flux analysis. This work used such methodology to establish comparisons within isogenic disease models in the context of PD.

1-15 Automated high-throughput and high-content image acquisition and analysis

The use of automated approaches to assess biological hypotheses enable high control of experimental conditions, contribute to the reproducibility, and provide high statistical power. Automation can be incorporated in controlling culture conditions by using laboratory stations connected with robotic arms (Check Hayden, 2014). In addition, acquisition of data can be automated by incorporating programmable experimental pipelines and computer level protocols (Carvalho, 2013; Linshiz et al., 2013). Furthermore, data analysis can be performed in a supervised automatic manner or unsupervised manner. Supervised automatic approaches require human coding of the algorithms on part of a dataset to implement it in bigger datasets. In contrast, in unsupervised approaches, machine learning and neuronal networks develop non-monitored code solutions to optimize a set of outputs. The three layers of automation described above - maintenance automation, acquisition automation and analysis automation - constitute the next generation of precision research. Multiple examples of automated data acquisition and analysis exist for live-monitoring of single cell dynamics (Skylaki et al., 2016). Here, two layers of automation are used: automated acquisition and supervised automated analysis.

第二章

Chapter 2

結果 1

Results 1

2-1 Genetically-encoded Rosella-LC3 and ATP5C1-Rosella systems allow for the visualization of the complete autophagy and mitophagy pathways

Generation of stable lines expressing Rosella sensors allowed the reconstruction of the complete autophagy and mitophagy pathways (Figure 2-1). In the case of the autophagy reporter lines, it is possible to observe all autophagy structures (Figure 2-1 A). First, it is possible to observe phagophores, as evident on punctate-like structures with pHluorin-positive and DsRED-positive signals (Figure 2-1 B). Furthermore, early-closure autophagosomes and mature autophagosomes correspond to semi-spheres and sphere-like structures, respectively. They present both pHluorin-positive and DsRED-positive double membrane peripheries, with pHluorin-negative and DsRED-negative centers (Figure 2-1 B). In addition, it is possible to define early autolysosomes, as noted on spherical structures with pHluorin-positive and DsRED-positive single membrane edges, with pHluorin-negative and DsRED-positive center (Figure 2-1 B). Finally, detection of mature autolysosomes is evidenced by spheres of DsRED-positive center without signals in its membrane (Figure 2-1 B). In the case of the mitophagy reporter lines, both mitochondria and mitophagic vacuoles can be visualized (Figure 2-1 C). Firstly, it is possible to observe mitochondria and the mitochondria network as evidenced by the rod-like structures with pHluorin-positive and DsRED-positive signals (Figure 2-1 D). Secondly, there are mitophagic vacuoles with partly digested mitochondria in their lumen, as evidenced by sphere structures with pHluorin-negative and DsRED-positive body, surrounding pHluorin-positive and DsRED-positive rod-like structures (Figure 2-1 D). Finally, mature mitophagic vacuoles are detected as sphere-like structures pHluorin-negative and DsRED-positive body (Figure 2-1 D).

Figure 2-1

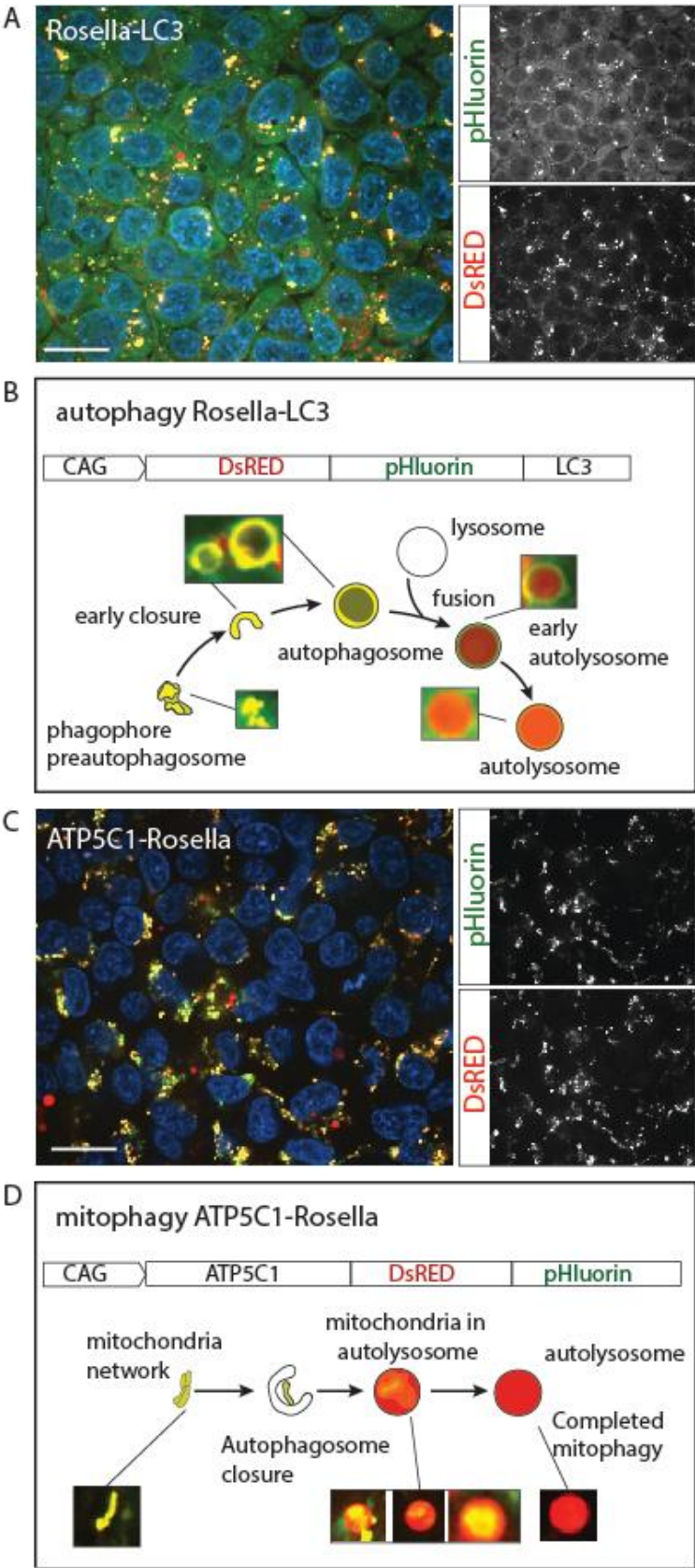
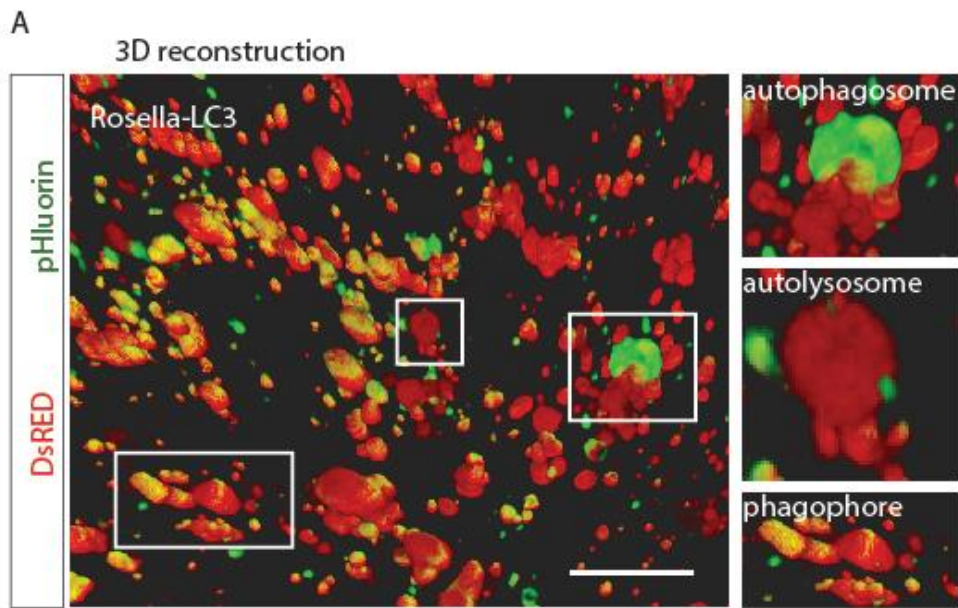


Figure 2-1. Genetically-encoded Rosella-LC3 and ATP5C1-Rosella systems allow for the visualization of the complete autophagy and mitophagy pathways. **A.** Representative image of Rosella-LC3 healthy control line. The pHluorin and DsRED channels are shown separately. Scale bar indicates 10µm. **B.** Structure of the Rosella autophagy reporter system. It is possible to identify all autophagy structures, including phagophores, autophagosomes, and autolysosomes. **C.** Representative image of ATP5C1-Rosella healthy control line. The pHluorin and DsRED channels are shown separately. Scale bar indicates 10 µm. **D.** Structure of the Rosella mitophagy reporter system. It is possible to determine mitochondrial network structure and mitophagy events.

2-2 3D reconstruction of reporter lines confirms complete reconstruction of autophagy and mitophagy pathways

3D reconstruction analysis confirmed that the structures described in **section 2-1** match (Figure 2-2). Spinning-disk microscopy z-stacks were used for the 3D reconstruction of the autophagy reporter line (Figure 2-2 A). For the autophagy reporter lines, pHluorin-positive and DsRED-positive phagophores (Figure 2-2 A), autophagosomes with pHluorin-positive and DsRED-positive cortex (Figure 2-2 A), and autolysosomes with pHluorin-negative and DsRED-positive body (Figure 2-2 A) are observed. A navigation video can be visualized by scanning the QR code provided (Figure 2-2 A). Confocal microscopy z-stacks were used for 3D reconstruction of the mitophagy reporter line (Figure 2-2 B). Mitophagy reporter lines were treated with valinomycin, a mitochondria stress modulator, to increase the rate of mitophagy events. A representative z-stack shows a DsRED-positive mitophagic vacuole surrounding partially digested mitochondria in an acidic environment (Figure 2-2 B). The partially digested mitochondria are evident by pHluorin-negative DsRED-positive rod-like structures (Figure 2-2 B). Beside the mitophagic vacuole is a pHluorin-positive DsRED-positive phagophore cluster (Figure 2-2 B).

Figure 2-2



Scan this QR code to access online video 2-2A

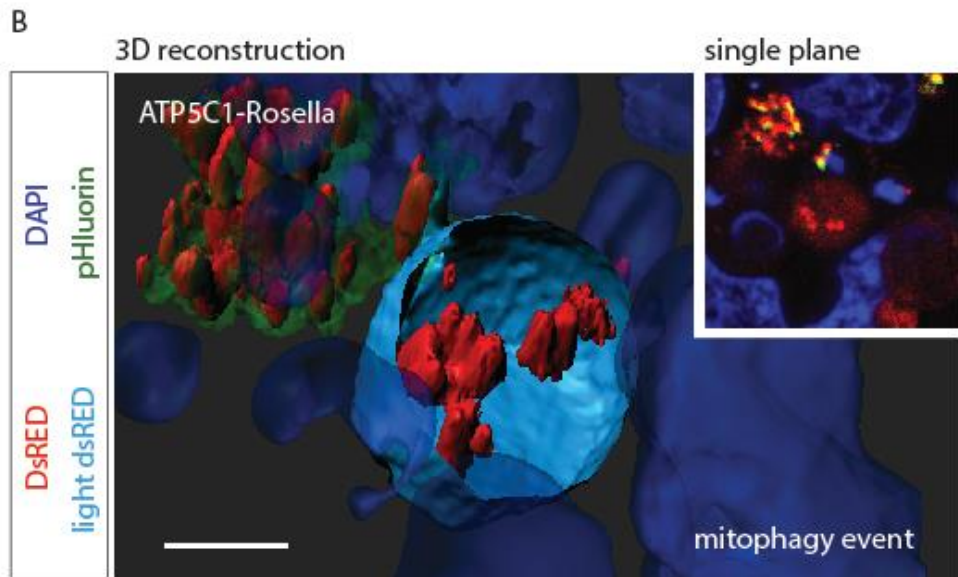


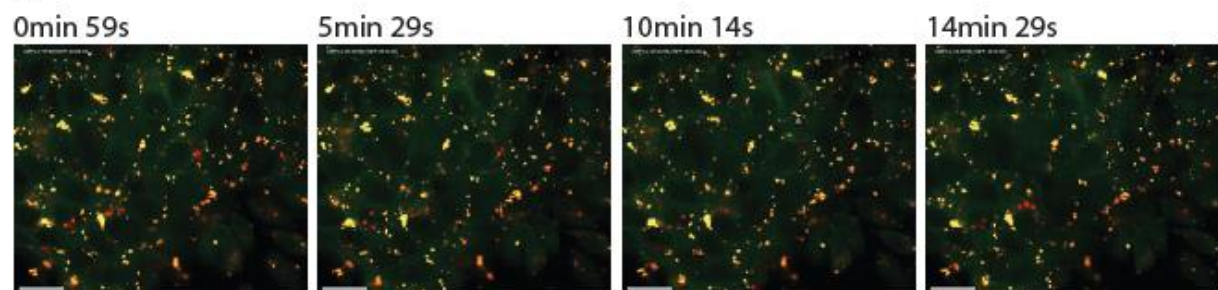
Figure 2-2. 3D reconstruction of reporter lines confirms complete reconstruction of autophagy and mitophagy pathways. **A.** 3D reconstruction based on the autophagy reporter healthy control line. The insets show pHluorin-positive DsRED-positive autophagosome structures, pHluorin-negative DsRED-positive autolysosome structures, and pHluorin-positive DsRED-positive phagophores. Scanning the QR code will provide a navigation video of the 3D reconstruction. Scale bar indicates 10 μ m. **B.** 3D reconstruction based on the mitophagy healthy control line. An autolysosome with an ongoing mitophagy process is shown. The autolysosome is represented with an equatorial cross section and the light intensity DsRED volume is represented in cyan. The partly digested mitochondria inside the autolysosome maintains the pH-resistant DsRED signal and is pHluorin-negative in this acidic environment. A pHluorin-positive DsRED-positive phagophore cluster is located in the upper left corner. The inset shows a single plane overlay. High frequency mitophagy conditions were induced with 5 μ M valinomycin. Scale bar indicates 4 μ m.

2-3 Human iPS cells present dynamic autophagy activity

Using spinning-disk microscopy live imaging, a remarkably active autophagy dynamic in healthy control human iPS cells was observed (Figure 2-3). Representative frames from the time-lapse are shown (Figure 2-3). Time-lapse videos can be accessed with the provided QR codes (Figure 2-3). Movement of autophagic vesicles range to approximately 5 μ m per second (Figure 2-3 A). Higher magnification of autophagy reporter lines allowed the observation of the emergence of autophagic vacuoles (Figure 2-3 B). Early autolysosomes present transient association to mature autolysosomes and phagophores (Figure 2-3 B). This suggests fusion of autophagic structures (Figure 2-3 B). The membrane of autolysosomes is partially deformed when associated to filament-like structures reminiscent of cytoskeleton (Figure 2-3 B). It was possible to observe that during cell division events, autophagic vacuoles are segregated to cell poles and separated by the metaphase plate (Figure 2-3 C). These observations are in agreement with the essential roles assigned to autophagy during development. Mutations in autophagy components result in lethality during pre-implantation development (Tsukamoto et al., 2008).

Figure 2-3

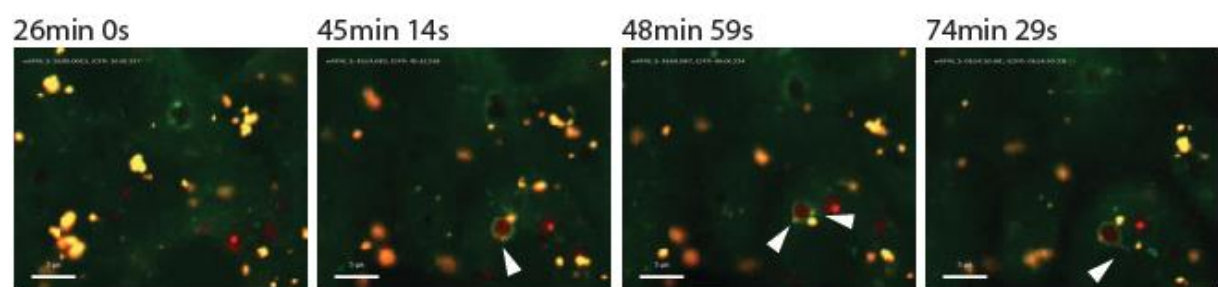
A



Scan this QR code to access online video 2-3A



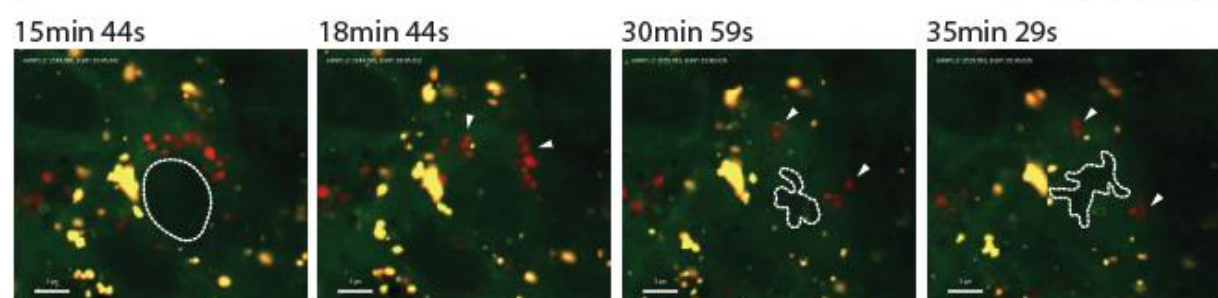
B



Scan this QR code to access online video 2-3B



C



Scan this QR code to access online video 2-3C



Figure 2-3. Human iPS cells present dynamic autophagy activity. **A.** The autophagy reporter healthy control line was imaged for 1 hour 15min. Representative frames from the time-lapse video are shown. Phagophores dynamically fuse and are mobilized throughout the cell. Autophagosomes grow and transform to autolysosomes. Speed 25fps. Scale bar indicates 20µm. Time-lapse video can be accessed with the provided QR code. **B.** Close-up of the autophagy reporter healthy control line from A. Representative frames from the time-lapse video. Arrows heads indicate the association between multiple autophagic structures and the early autophagosome. The generation of pHluorin-positive DsRED-positive autophagosomes and the maturation to autolysosomes of pHluorin-negative DsRED-positive lumen are observed. Speed 25fps. Scale bar indicates 5 µm. Time-lapse video can be accessed with the provided QR code. **C.** Close-up of the autophagy reporter healthy control line from A. Representative frames from the time-lapse video. After the nucleus (indicated with a dashed line) is disassembled, the autophagic structures are segregated to both cell poles (indicated with arrow heads). The condensed chromosomes (indicated with a dashed line) migrate to the cell equator and establish the metaphase plate (indicated with a dashed line). Speed 25fps. Scale bar indicates 5 µm. Time-lapse video can be accessed with the provided QR code.

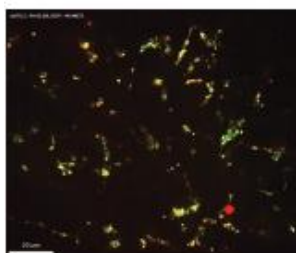
2-4 Human iPS cells present a dynamic mitochondria network and mitophagy activity

Using live imaging, a dynamic mitochondrial network in human iPS cells can be seen (Figure 2-4). Mitochondria network re-structuring and splitting can be seen (Figure 2-4 A). Furthermore, abundant mitophagy events occur (Figure 2-4 A). This observation is consistent with studies that demonstrate the importance of mitochondria homeostasis in pluripotent stem cells, both during development and in adult cells (Jahreiss et al., 2008; Lorenz et al., 2017; Ma et al., 2015; Wang et al., 2015). Autolysosomes that were responsible for mitophagy are visible as pHluorin-negative and DsRED-positive vesicles (Figure 2-4 A). Higher magnification of the time-lapse revealed mitochondrial network re-structuring and splitting (Figure 2-4 B). In addition, mitochondria network monitoring through the “kiss and run” mechanism was observed (Figure 2-4 C) as previously described (Jahreiss et al., 2008).

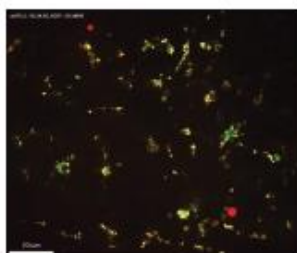
Figure 2-4

A

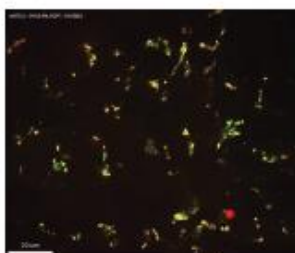
25min 15s



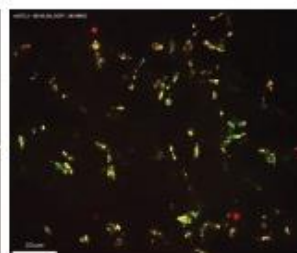
38min 45s



50min 0s



66min 15s

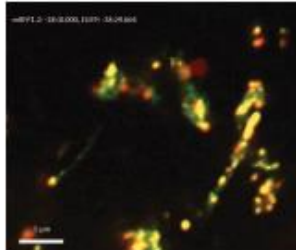


Scan this QR code to access online video 2-4A

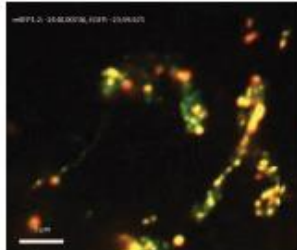


B

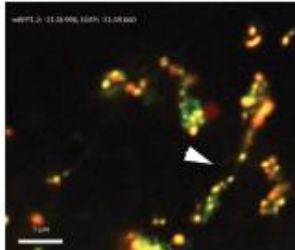
46min 30s



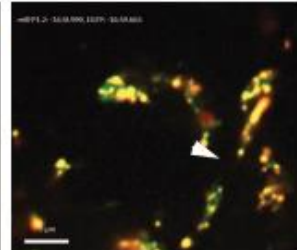
51min 0s



53min 0s



58min 0s

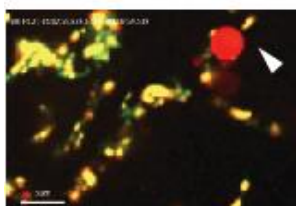


Scan this QR code to access online video 2-4B

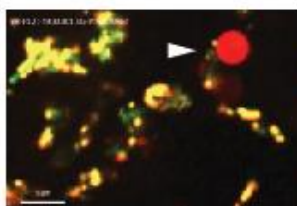


C

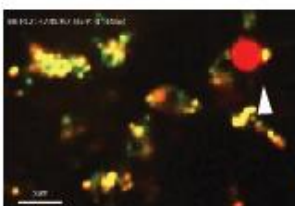
12min 0s



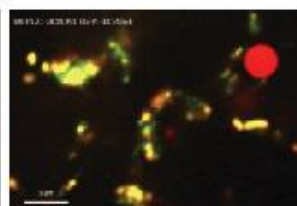
15min 30s



27min 15s



37min 45s



Scan this QR code to access online video 2-4C



Figure 2-4. Human iPS cells present a dynamic mitochondria network and mitophagy activity. **A.** The mitophagy healthy control reporter line was imaged for 1 hour 15min. Mitochondria network dynamically reorganized and split. Autolysosomes that were responsible for mitophagy are visible as pHluorin-negative DsRED-positive vesicles. Speed 25fps. Scale bar indicates 20 μm . Time-lapse video can be accessed with the provided QR code.

B. Close-up of the mitophagy healthy control reporter line in A. Mitochondria network restructured and split. Splitting point indicated with arrow head. Speed 25fps. Scale bar indicates 20 μm . Time-lapse video can be accessed with the provided QR code.

C. Close-up of the mitophagy healthy control reporter line in A. Autolysosomes associate with the mitochondrial network and monitor it with the “kiss and run” mechanism (indicated with arrow head). Mitochondrial networks dynamically reorganize. Speed 25fps. Scale bar indicates 20 μm . Time-lapse video can be accessed with the provided QR code.

2-5 Generation of image analysis algorithms to identify autophagy structures

Evaluating autophagy differences between healthy control and mutant lines requires the development of quantification tools. For this purpose, image analysis algorithms were developed. These tools allow for the classification and quantification of autophagy structures automatically and in an unbiased way. Automated high-throughput imaging platforms (Opera, Perkin Elmer) produce live images in a reproducible and high-throughput manner for all the reporter lines in controlled incubation conditions (37°C and 5%CO₂). The algorithms used for image analysis were implemented in Matlab code. This process is described below. The raw images (Figure 2-5 A) were flat-field corrected and deconvolved with the Richards-Wolf optical model (Figure 2-5 B). Then, a series of difference of Gaussian curves were applied in both channels (Figure 2-5 C-D), and both channels were assessed with Boolean OR logical operations (Figure 2-5 C-D). Watershed functions with Euclidean distance was implemented for DsRED (Figure 2-5 C). Ratio images were calculated, and top-hat functions included in both channels to detect potentially missed autolysosomes (Figure 2-5 E). To detect autophagosomes based on their cavity vesicle property, a chain of: Fourier transform, Euler filtering, Butterworth high-pass filter, binarization, maximum projection, and erosion were all implemented. Components containing cavities have an Euler number 0 and are autophagosomes (Figure 2-5 F). To detect the remaining autophagosomes, Hough transforms for circles were included (Figure 2-5 G). The mask of all autophagosome candidates was computed by combining Fourier-Euler and Hough-derived autophagosomes (Figure 2-5 F-G). For classification, all vesicles detected via the different approaches shown above were combined with Boolean operations. For the remaining vesicles, the eccentricity was assessed (Figure 2-5 H). The classification of the segmented vesicles was defined to consider four vesicle types: phagophores, autophagosomes, early autolysosomes, and late autolysosomes. For this

purpose, a progressive exclusion algorithm based on logical operations was implemented and is exemplified (Figure 2-5 I).

Figure 2-5

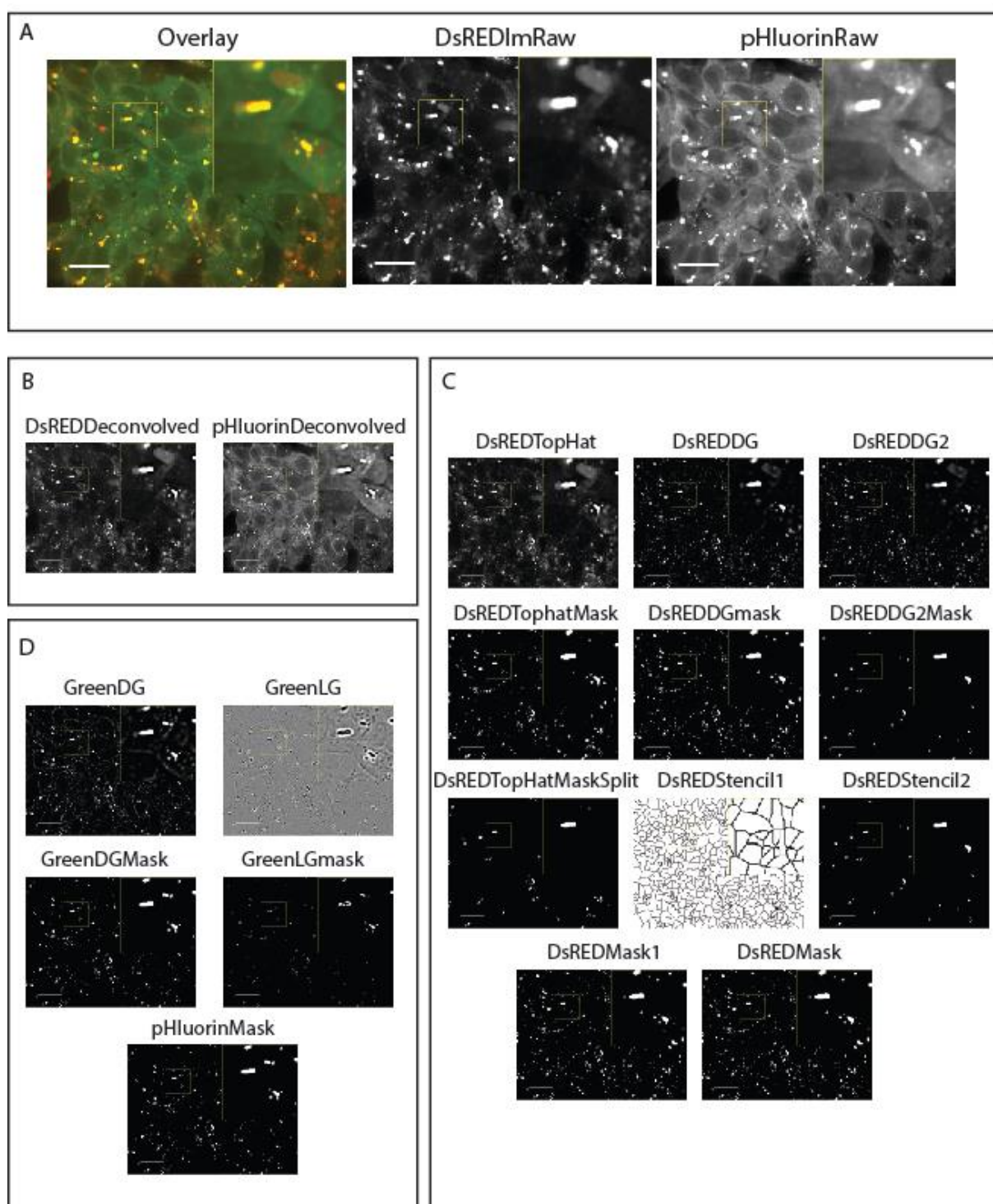


Figure 2-5 (continuation)

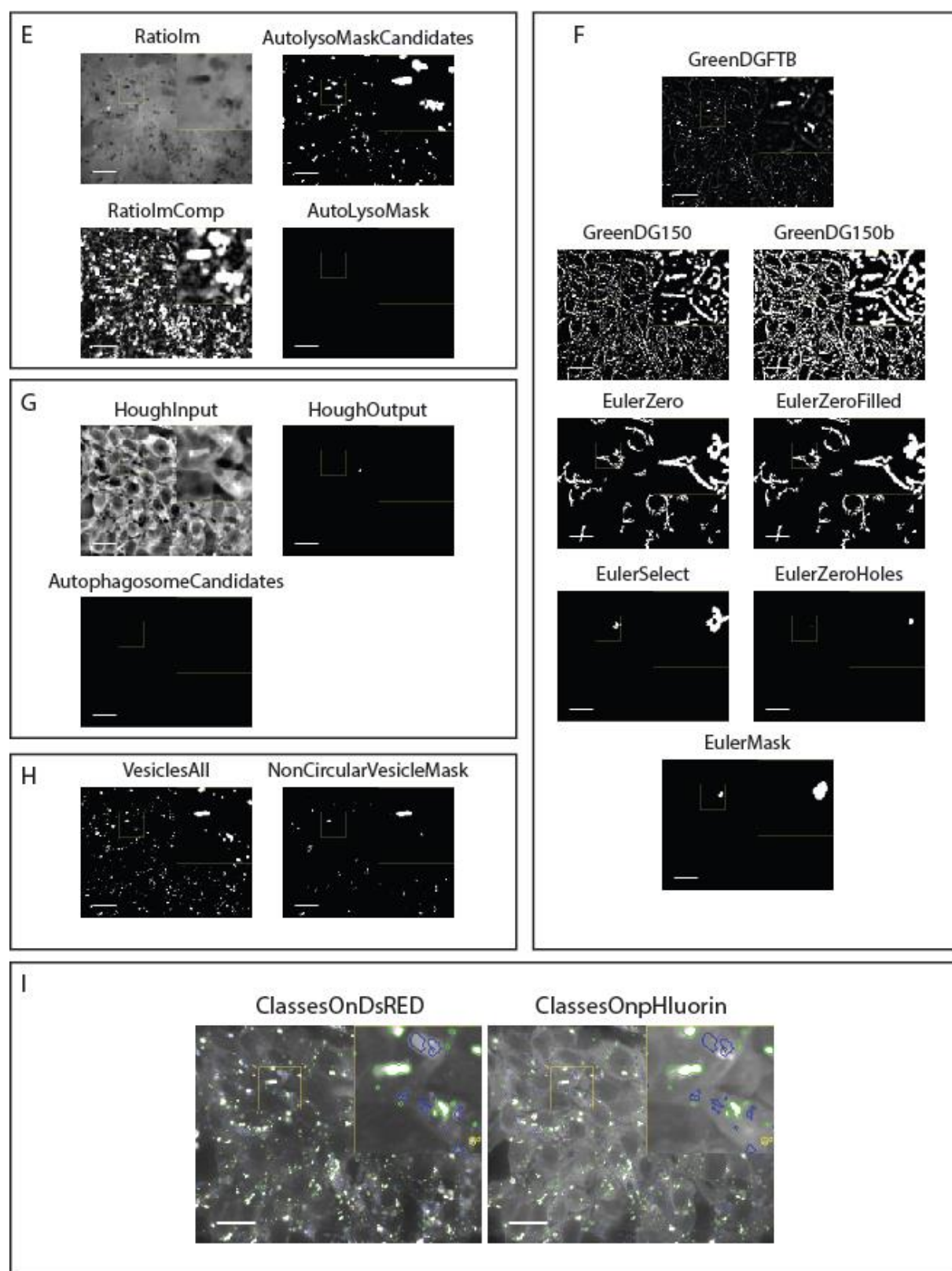


Figure 2-5. Generation of image analysis algorithms to identify autophagy structures. Image analysis workflow for autophagy reporter lines. **A.** Overlay of raw DsRED and pHluorin channels, raw image for DsRED and raw image for pHluorin channel. **B.** Flat field and deconvolved images for channel DsRED and pHluorin. **C.** Difference of Gaussian, top hat filter and stencil filter for DsRED channel. **D.** Difference of Gaussian and Laplacian of Gaussian analysis for pHluorin channel. **E.** Ratio of intensities to identify autolysosomes. **F.** Difference of Gaussians and Euler analysis on pHluorin channel to identify autophagosomes. **G.** Hough transforms to identify autophagosomes. **H.** Composed mask of all vesicles identified and non-circular vesicles. **I.** All vesicles mapped on pHluorin and DsRED channel. Scale bar indicates 20 μ m and 3x zoomed insets are highlighted with yellow boxes.

2-6 Generation of image analysis algorithms to identify mitochondria and mitophagy structures

Evaluating mitophagy differences between healthy control and mutant lines requires the development of quantification tools. For this purpose, and similarly to **section 2-5**, image analysis algorithms were developed. They allow the classification and quantification of mitophagy structures automatically and in an unbiased way. The algorithms used for image analysis were implemented in Matlab code, and the process for mitophagy reporters is described below. Representative raw images are shown (Figure 2-6 A-C). The DsRED channel is subjected to difference of Gaussians (Figure 2-6 D), and a grey tone threshold applied to define mitochondria mask (Figure 2-6 E). Mitophagy vacuoles were defined by intensity ratio analysis and morphological filters based on difference of Gaussian thresholds (Figure 2-6 F). Mitophagy vacuole mask was optimized with shape reconstruction functions (Figure 2-6 G). A base difference of Gaussians was established in the DsRED channel to identify the mitophagic vacuoles (Figure 2-6 H). Finally, the resulting segmented mitochondria (Figure 2-6 I) and autophagic vacuole masks (Figure 2-6 J) were defined.

Figure 2-6

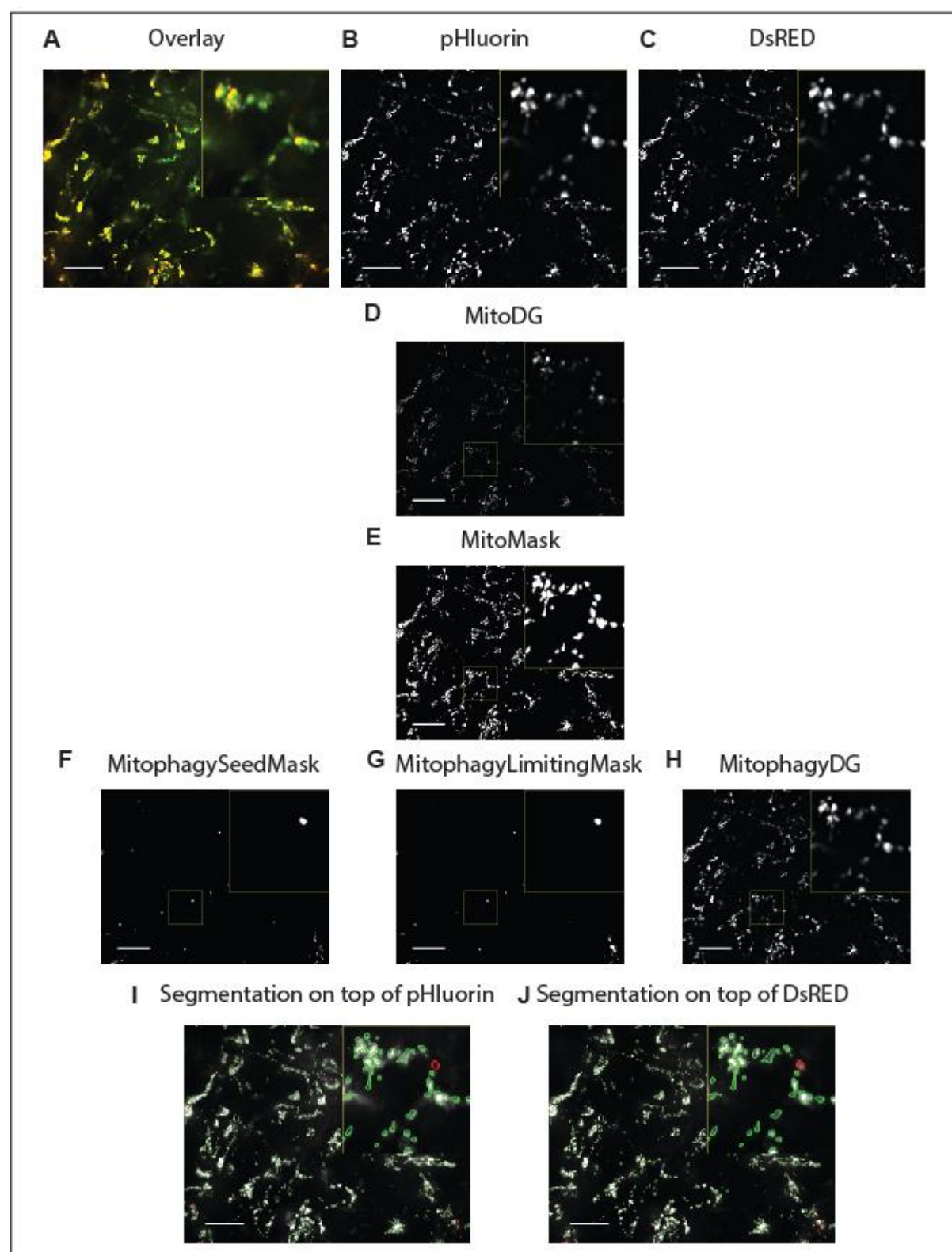


Figure 2-6. Generation of image analysis algorithms to identify mitochondria and mitophagy structures. Image analysis workflow for mitophagy with ATP5C1-Rosella reporter lines. **A.** Overlay of raw DsRED and pHluorin channels. **B.** Raw image for pHluorin channel. **C.** Raw image for DsRED channel. **D.** Difference of Gaussian for pHluorin channel. **E.** Mitochondria network mask. **F.** Mitophagic vacuoles mask by intensity ratio threshold. **G.** Refinement of Mitophagic vacuole mask with reconstruction function. **H.** Difference of Gaussian in the DsRED channel. **I.** All mitochondria and mitophagic vacuoles mapped on pHluorin channel. **J.** All mitochondria and mitophagic vacuoles mapped on DsRED channel. Scale bar indicates 20 μ m and 3x zoomed insets are highlighted with yellow boxes.

2-7 Generation of image analysis algorithms to identify lysosomes

The interpretation of autophagy and mitophagy modulation in some cases is dependent on the lysosome capacity of a cell. Hence, a lysosome recognition algorithm was developed (Figure 2-7). The autophagy and mitophagy reporter lines were treated with lysosomal tracking dyes and images used for pattern recognition. The raw images in deep red (Figure 2-7 A) were deconvolved (Figure 2-7 B). A set of difference of Gaussians were used for convolving the foreground and subtracting the background (Figure 2-7 C). A partial mask for lysosomes was obtained by threshold functions (Figure 2-7 E). Additionally, a set of Laplacian of Gaussians were applied on the deconvolved images (Figure 2-7 D). A second mask of lysosomes is detected with grey tone threshold functions (Figure 2-7 F). The combination of both lysosome masks with Boolean functions allows for the detection of lysosomes (Figure 2-7 G).

Figure 2-7

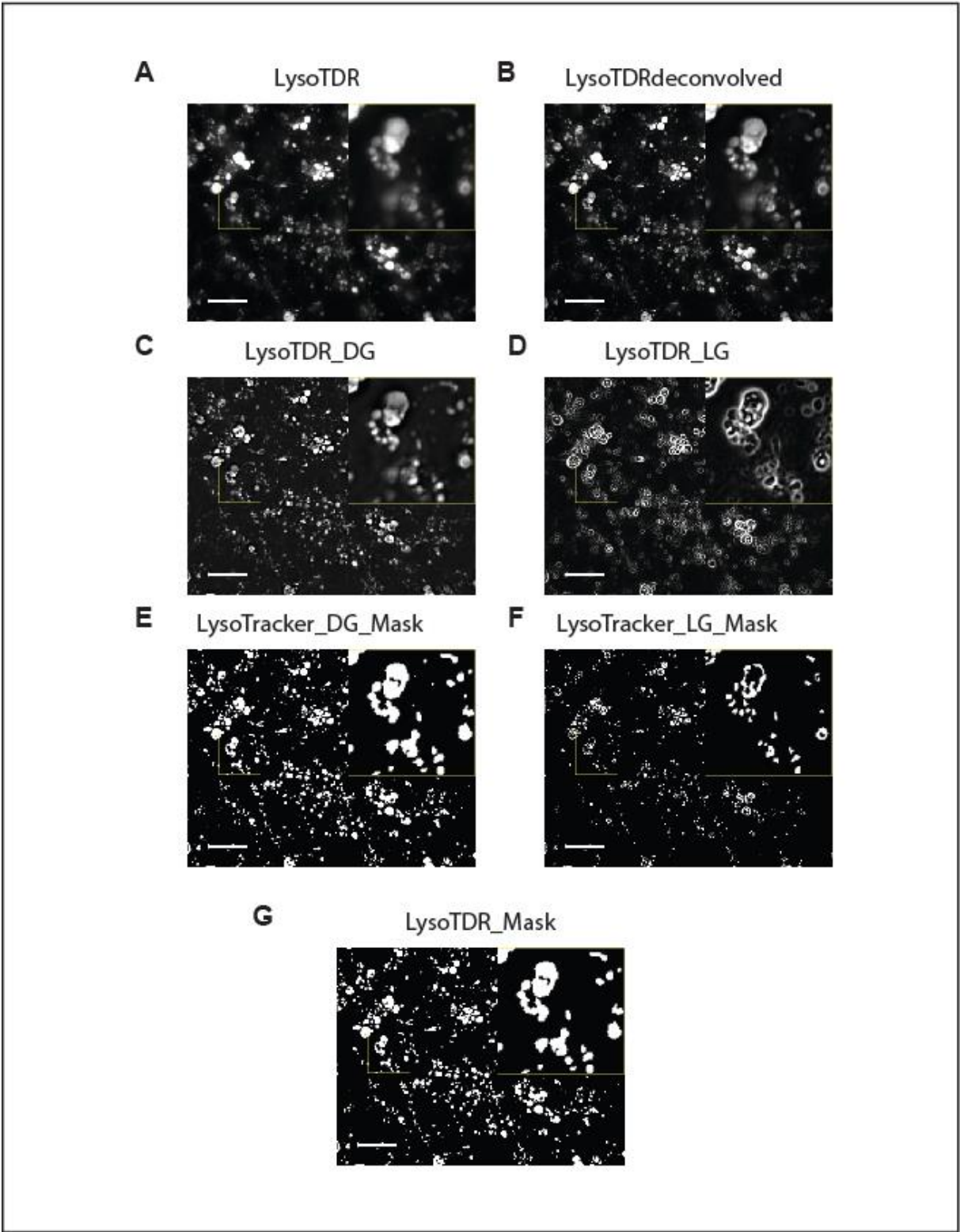


Figure 2-7. Generation of image analysis algorithms to identify lysosomes. Image analysis workflow for the LysoTracker assay in reporter lines. **A.** Raw image for lysotracker in deep red channel. **B.** Deconvolved image of lysosomes. **C.** Difference of Gaussian for deep red channel. **D.** Laplacian of Gaussian for deep red channel. **E.** Lysosome mask from difference of Gaussians. **F.** Lysosome mask from Laplacian of Gaussians. **G.** Combined lysosome mask. Scale bar indicates 20 μ m and 3x zoomed insets are highlighted with yellow boxes.

2-8 PD-mutant lines present a reduced autophagy capacity in basal conditions

Making use of the automated image analysis tools developed, quantification of the autophagic structures in healthy control and PD-mutant lines was performed in human iPS cells: PINK1(p.I368N), VPS35(p.D620N), and LRRK2(p.G2019S). First, all mutants were compared with healthy controls in basal conditions. The absolute frequency of phagophores was reduced in PINK1(p.I368N) and VPS35(p.D620N) mutants with respect to the healthy control line (Figure 2-8 A). Autophagosomes are transient, therefore their detection was infrequent. The frequency of autophagosomes was significantly reduced in the LRRK2(p.G2019S) mutant with respect to healthy control (Figure 2-8 B). Early autolysosomes were significantly reduced in PINK1(p.I368N) and VPS35(p.D620N) mutants (Figure 2-8 C). Furthermore, late autolysosomes were significantly reduced in all the mutants (Figure 2-8 D). Autophagic vacuoles are defined as the sum of all autophagosomes, early autolysosomes, and late autolysosomes in a cell, a convention widely accepted by the autophagy community (Klionsky et al., 2016). The autophagic vacuoles of all mutants were reduced in comparison to the healthy control (Figure 2-8 E). Therefore, these results indicate that LRRK2(p.G2019S), PINK1(p.I368N), and VPS35(p.D620N) mutations result in an overall decreased autophagy capacity in basal conditions.

Figure 2-8

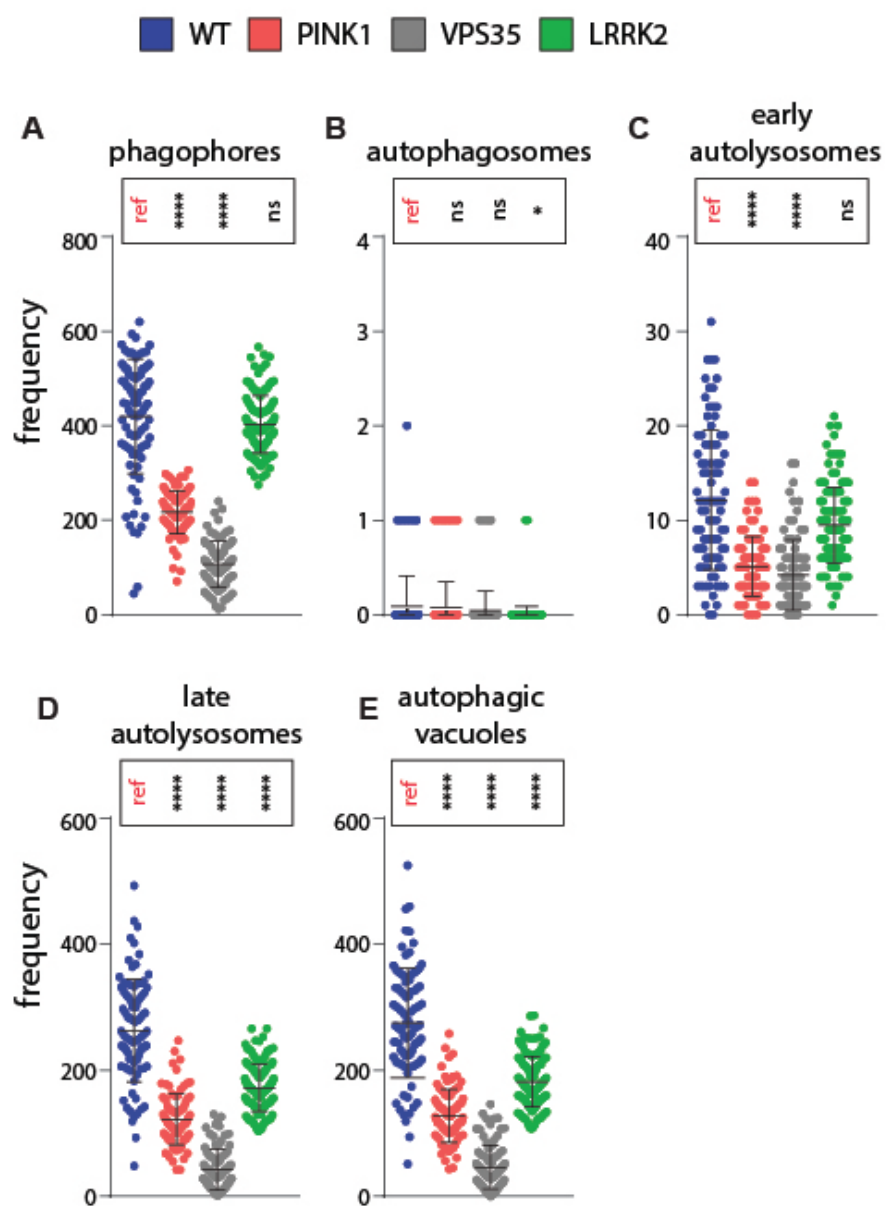


Figure 2-8. PD-mutant lines present a reduced autophagy capacity in basal conditions. A.

Frequency of phagophores for healthy control and mutant lines. **B.** Frequency of autophagosomes. **C.** Frequency of early autolysosomes. **D.** Frequency of late autolysosomes. **E.** Frequency of autophagic vacuoles. Kruskal-Wallis and Dunn's multiple comparison test for all the lines with respect to its reference (ref) healthy control counterpart. All structures were measured in basal conditions. Significance levels are * $p < 0.05$, ** $p < 0.01$, *** $p < 0.001$, and **** $p < 0.0001$.

2-9 PD-mutant lines present an impaired autophagy reaction constant

A reaction constant is defined as the ratio between products and reagents. Hence, an autophagy reaction constant can be established. This can be achieved by calculating the experimental frequency of phagophores and the autophagic vacuoles in basal conditions. Approximations of this concept have been previously conducted by western blotting of stage-specific protein forms (Klionsky et al., 2016). The autophagy reaction rate constant for healthy control and PINK1(p.I368N) cells were 0.41 and $0.37s^{-1}$, respectively (Figure 2-9 A). In basal conditions, the healthy control and PINK1(p.I368N) autophagy reaction rate constant has no significant difference (Figure 2-9 A). The VPS35(p.D620N) and LRRK2(p.G2019S) mutant cell lines present higher proportions of phagophores in comparison to autophagic vacuoles, hence, they have a decreased ability to progress through autophagy in basal conditions. Their autophagy reaction rate constants were $0.28s^{-1}$ and $0.31s^{-1}$, respectively (Figure 2-9 A).

Figure 2-9

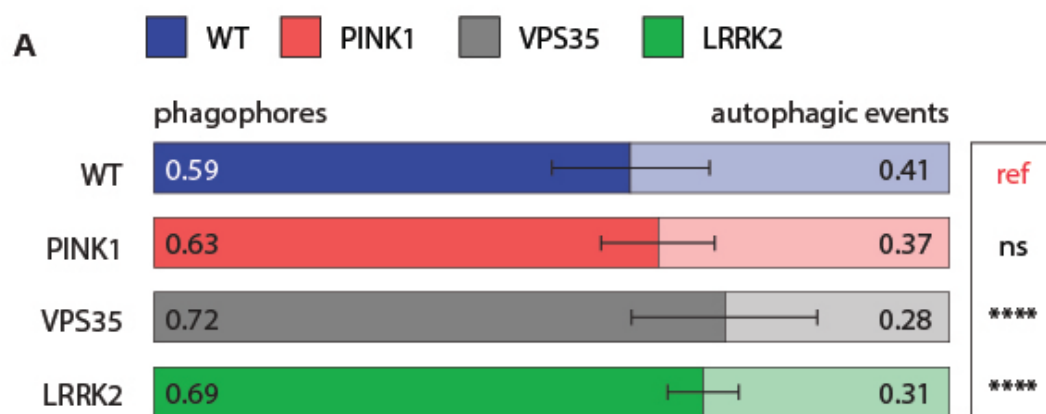


Figure 2-9. PD-mutant lines present an impaired autophagy reaction constant. A. Autophagy reaction rate constant for healthy control and mutant lines. The reaction rate constant is calculated as the ratio of autophagic vacuoles and phagophores. Kruskal-Wallis and Dunn's multiple comparison test for all the lines with respect to its reference (ref) healthy control counterpart. All structures were measured in basal conditions. Significance levels are * $p < 0.05$, ** $p < 0.01$, *** $p < 0.001$, and **** $p < 0.0001$.

2-10 Responsiveness of reporter lines to autophagy and mitophagy modulation

Autophagy and mitophagy pathways can be modulated at several points, including the pathways upstream of phagophore formation, fusion of lysosomes to autophagosomes and mitochondria integrity (Figure 2-10 A-B). In order to evaluate the responsiveness of the studied mutant lines, multiple autophagic and mitophagic small-molecule modulators were used. These modulators included: bafilomycin, chloroquine, rapamycin, thapsigargin, CCCP, DFP, oligomycin and valinomycin. Here indicates the quantification results of autophagic vesicles types, as in the previous section, for all the lines and treatments (Figure 2-10 C-F). This includes: healthy control (Figure 2-10 C), PINK1(p.I368N) mutant (Figure 2-10 D), VPS35(p.D620N) mutant (Figure 2-10 E) and LRRK2(p.G2019S) mutant (Figure 2-10 F). Detailed description of each treatment is indicated in the following sections.

A autophagy Rosella-LC3

B mitophagy ATP5C1-Rosella

C

D

E

F

Figure 2-10. Responsiveness of reporter lines to autophagy and mitophagy modulation. A.

Schematic representation of the autophagy pathway and the points at which small-molecules can modulate it. Compounds are indicated in blue. An antagonist relationship is indicated with a bar and an agonist reaction with an arrowhead. **B.** Schematic representation of the mitophagy pathway and the points at which small-molecules can modulate it. Compounds are indicated in blue. An antagonist relationship is indicated with a bar and agonist reaction with an arrowhead. **C.** Absolute frequency quantification of autophagic structures for all the autophagy (orange background) and mitophagy (light orange background) modulators used on the healthy control line. **D.** PINK1(p.I368N) mutant. **E.** VPS35(p.D620N) mutant. **F.** LRRK2(p.G2019S) mutant. Oligomycin (oligo), valinomycin (val) bafilomycin (baf), chloroquine (chlo), rapamycin (rapa) and thapsigargin (thap). Kruskal-Wallis and Dunn's multiple comparison test for all the structures with respect to its reference (ref) basal condition. Significance levels are * $p < 0.05$, ** $p < 0.01$, *** $p < 0.001$, and **** $p < 0.0001$.

2-11 Differential phagophore responsiveness to autophagy blockage

The accumulation of phagophores was evaluated by blocking the progression through the autophagy pathway with bafilomycin and chloroquine. Upon addition of the proton ATPase inhibitor bafilomycin, acidification of lysosomes is impaired. This results in the blockage of the degradation pathway as previously described (Klionsky et al., 2016). An increased level of phagophores for PINK1(p.I368N) (Figure 2-10 D and Figure 2-11 A) and VPS35(p.D620N) (Figure 2-10 E and Figure 2-11 A) mutants was observed with respect to their respective basal references (Figure 2-10 D-E and Figure 2-11 A). The concentration of bafilomycin used did not result in accumulation of phagophores in the healthy control with respect to its basal conditions (Figure 2-10 C and Figure 2-11 A). Bafilomycin resulted in decreased abundance of autophagic vacuoles for healthy control (Figure 2-10 C and Figure 2-11 B) and LRRK2(p.G2019S) cells (Figure 2-10 F and Figure 2-11 B), when compared to their respective basal conditions. For healthy control, this is in agreement with blockage of lysosome fusion and progression through autophagy (Klionsky et al., 2016). Similarly, addition of chloroquine resulted in increased levels of phagophores for PINK1(p.I368N) (Figure 2-10 D and Figure 2-11 A) and VPS35(p.D620N) (Figure 2-10 E and Figure 2-11 A) cells. Chloroquine resulted in decreased levels of autophagic vacuoles for healthy control (Figure 2-10 C and Figure 2-11 B) and LRRK2(p.G2019S) cells (Figure 2-10 F and Figure 2-11 B) as it was for bafilomycin.

Figure 2-11

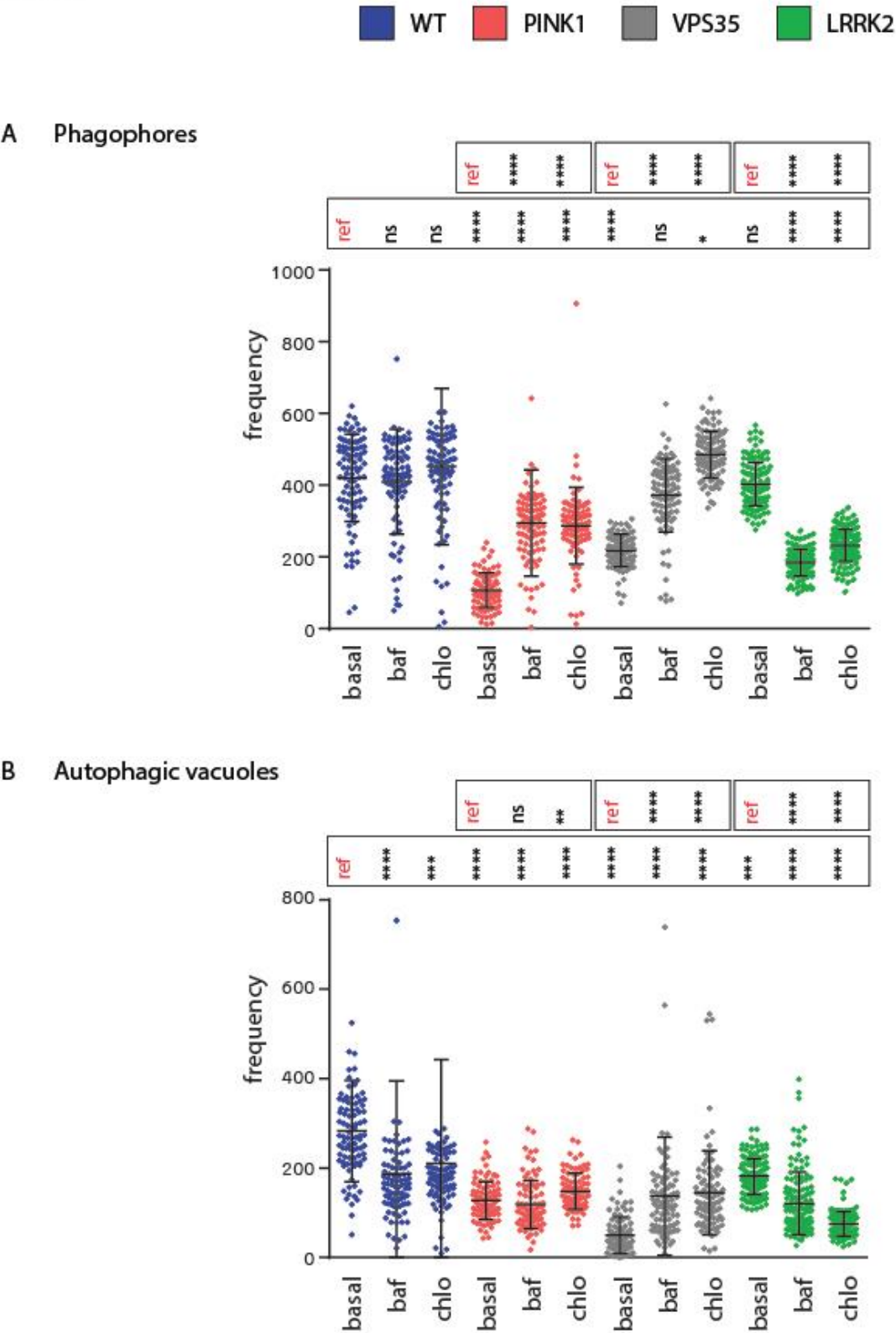


Figure 2-11. Differential phagophore responsiveness to autophagy blockage. **A.** Absolute quantification of phagophores in healthy control, PINK1(p.I368N), VPS35(p.D620N) and LRRK2(p.G2019S) mutants. **B.** Absolute quantification of autophagic vacuoles in healthy control, PINK1(p.I368N), VPS35(p.D620N) and LRRK2(p.G2019S) mutants. Bafilomycin (baf) and chloroquine (chlo). Kruskal-Wallis and Dunn's multiple comparison test for all cell types with respect to its reference (ref) basal condition. Significance levels are * $p < 0.05$, ** $p < 0.01$, *** $p < 0.001$, and **** $p < 0.0001$.

2-12 Regulation of phagophore upstream pathways: CaMK-β/AMPK and mTOR

The CaMK-β protein regulates the autophagy pathway upstream of phagophore formation (Hoyer-Hansen et al., 2007). CaMK-β activates AMPK, and subsequently AMPK inhibits the mTOR complex. Since mTOR is an inhibitor of phagophore formation, inhibition of the inhibitor results in promotion of autophagy (Kim et al., 2011). Together these three pathways result in combined regulation of the autophagy flow. Thapsigargin increases the intracellular concentration of Ca^{+2} , and was used to quantify CaMK-β/AMPK axis-dependent autophagy and mitophagy (Figure 2-10 A-B). Thapsigargin resulted in increased phagophore levels in VPS35(p.D620N) (Figure 2-10 E and Figure 2-12 A) and PINK1(p.I368N) mutants (Figure 2-10 D and Figure 2-12 A). This suggests that there is a spare CaMK-β/AMPK capacity on VPS35(p.D620N) and PINK1(p.I368N) mutants. The concentration of thapsigargin used resulted in no modification of the phagophore level for healthy control (Figure 2-10 C and Figure 2-12 A). Furthermore, in VPS35(p.D620N) and PINK1(p.I368N) cells, the AMPK input resulted not only in increased phagophore levels but also in increased abundance of autophagic vacuoles (Figure 2-10 D-E and Figure 2-12 B). This result highlights a latent demand for phagophore generation in the mutant lines, which results in a burst of mature autophagic structures, upon CaMK-β/AMPK input (Figure 2-10 D-E and Figure 2-12 B). As mentioned above, mTOR complex 1 inhibits autophagy by its interaction with ULK1, which results in reduced formation of the phagophore complex (Kim et al., 2011). Rapamycin is an inhibitor of mTOR, hence its use allowed quantification of the direct extent of autophagy controlled by the mTOR pathway. Addition of rapamycin resulted in increased phagophore levels in VPS35(p.D620N) and PINK1(p.I368N) mutants (Figure 2-12 A). This suggested that modulation of mTOR could increase the phagophore generation in other VPS35 and PINK1 mutant types. Remarkably, treatment of PINK1(p.I368N) cells with rapamycin restored phagophore levels to

healthy control basal levels (Figure 2-10 D Figure 2-12 A). As reported in the literature (Kim et al., 2011), there was an increased level in phagophore formation for healthy control cells (Figure 2-12A). As discussed in **section 2-8** autophagic vesicle levels are significantly higher in healthy control lines compared to all mutants under basal conditions. It is possible that the combined addition of thapsigargin and rapamycin could have synergistic effects on autophagy because of the double input provided by the CaMK- β /AMPK and mTOR pathways. However, further increase in phagophore formation was not observed when compared to rapamycin alone (Figure 2-10 C-F and Figure 2-12 A). This can be due to ubiquitous effects of the mTOR pathway (Kim et al., 2011). Moreover, rapamycin alone or in combination with thapsigargin resulted in an increase in autophagic vacuoles for PINK1(p.I368N) and VPS35(p.D620N) mutants (Figure 2-12 B).

Figure 2-12

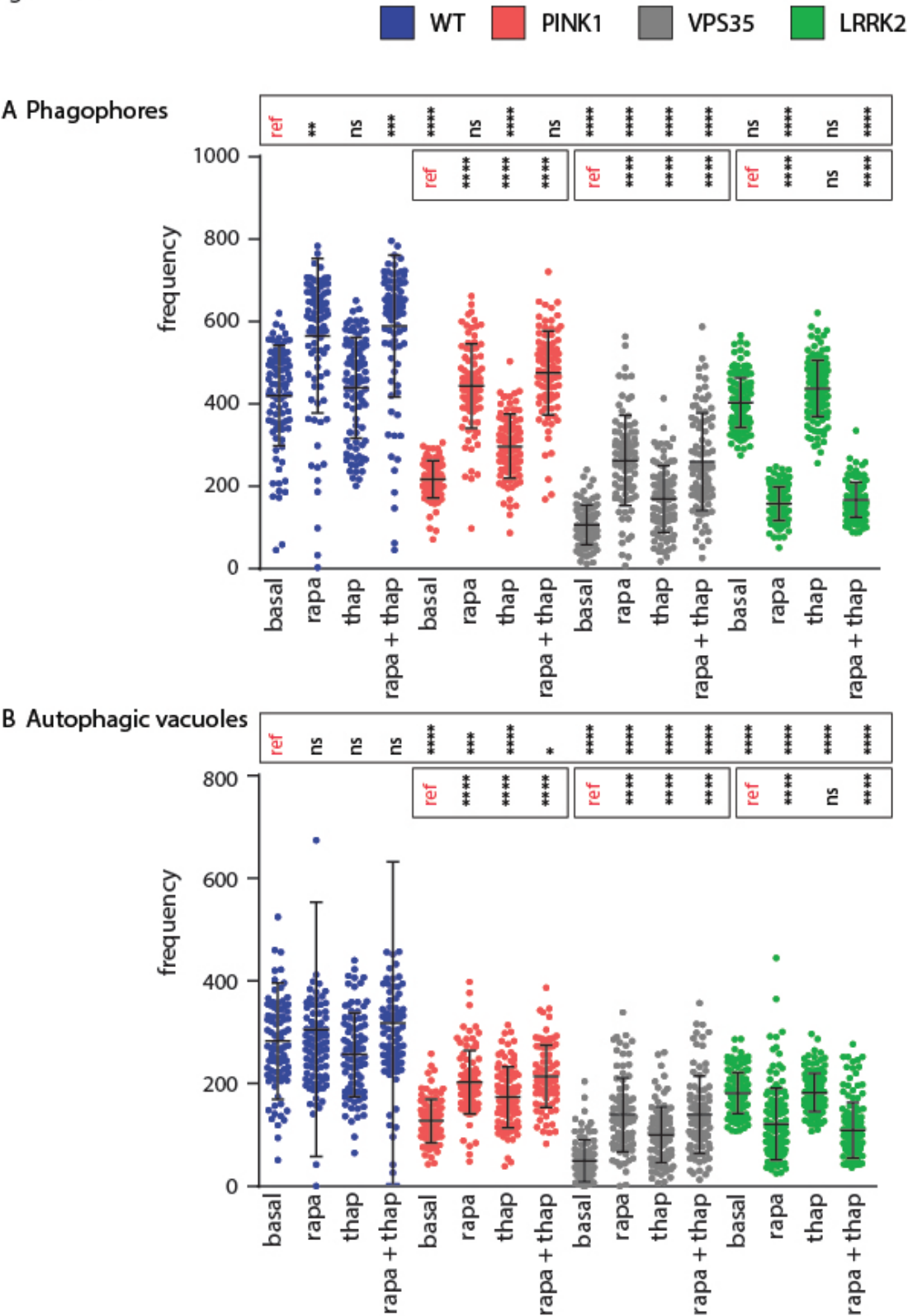


Figure 2-12. Regulation of phagophore upstream pathways: CaMK- β /AMPK and mTOR. A.

Absolute quantification of phagophores in healthy control, PINK1(p.I368N), VPS35(p.D620N) and LRRK2(p.G2019S) mutants upon the addition of upstream-phagophore modulators. **B.**

Absolute quantification of autophagic vacuoles in healthy control, PINK1(p.I368N), VPS35(p.D620N) and LRRK2(p.G2019S) mutants upon the addition of upstream-phagophore modulators. Rapamycin (rapa) and thapsigargin (thap). Kruskal-Wallis and Dunn's multiple comparison test for all cell types with respect to its reference (ref) basal condition. Significance levels are * $p < 0.05$, ** $p < 0.01$, *** $p < 0.001$, and **** $p < 0.0001$.

2-13 Evaluation of mitophagy contribution to general autophagy

The reporter system Rosella-LC3, described in **section 2-1**, quantifies the level of all autophagic structures of general autophagy. General autophagy is the composition of both, mitochondrial autophagy, also called mitophagy, and non-mitochondrial autophagy. The reporter system ATP5C1-Rosella quantifies the mitophagy contribution to general autophagy. Hence, comparisons of the Rosella-LC3 and ATP5C1-Rosella reporter readouts indicate the distribution of autophagic resources when exposed to mitochondrial stress. In order to establish the mitophagy contribution to general autophagy and the cellular responsiveness to mitochondrial stress, a panel of widely accepted mitophagy inducers was used (Bendor et al., 2013; Sargsyan et al., 2015). The compounds oligomycin, valinomycin, and CCCP induce stress through regulation of the mitochondrial membrane potential, resulting in PINK1-dependent mitophagy. On the other hand, the compound DFP induces mitophagy through Fe^{+2} chelation and PINK1-independent mechanisms (Bendor et al., 2013). Upon addition of membrane potential-mitophagy modulators, the levels of phagophore and autophagic vacuoles increased in VPS35(p.I368N) and PINK1(p.I368N) mutants (Figure 2-13 A). Mitophagy can be induced through PINK1-dependent and PINK1-independent mechanisms. Phagophore and autophagic vacuole levels increased for the PINK1(p.I368N) mutant when PINK1-dependent mitochondrial stressors CCCP, oligomycin and valinomycin (Figure 2-13 A-B) were used. This could be explained by the activation of PINK1-independent mitophagy mechanisms (Bendor et al., 2013). In addition, the PINK1-independent inducer of mitophagy, DFP, increased the levels of autophagic vacuoles in PINK1(p.I368N) and VPS35(p.I368N) mutants (Figure 2-13 A). For the LRRK2(p.G2019S) mutant, distinct modulators of mitophagy consistently decreased the levels of all autophagic structures (Figure 2-13 A-B). This is in agreement with the observations of a reduced tolerance to stress in this mutant. Increased levels of autophagic

and mitophagic structures are expected upon stress induction, however, the basal levels of autophagic structures for LRRK2 mutant are significantly lower than healthy control, and an additional stress might result in complete loss of homeostasis. From the mitochondria stressors used, only oligomycin and valinomycin were able to induce an increase in phagophore levels in the healthy control (Figure 2-13 A). When analyzing the levels of autophagic vacuoles, CCCP, DFP and valinomycin induced an increase of autophagic vacuoles in the healthy control (Figure 2-13 B). Finally, all mitochondria stressors increased autophagic vacuole levels for PINK1(p.I368N) and VPS35(p.D620N) mutants (Figure 2-13 B).

Figure 2-13

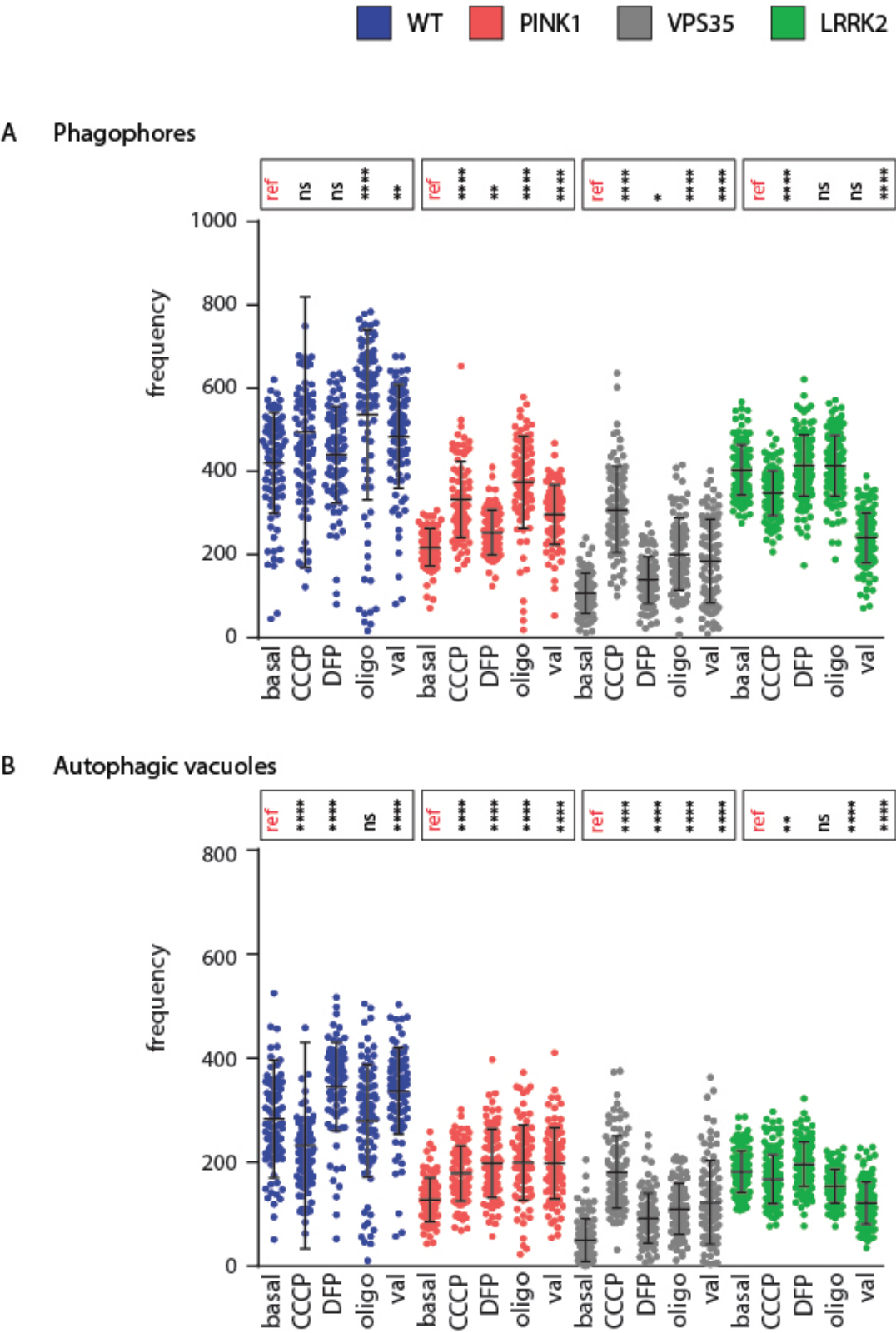


Figure 2-13. Evaluation of mitophagy contribution to general autophagy. **A.** Absolute quantification of phagophores in healthy control, PINK1(p.I368N), VPS35(p.D620N) and LRRK2(p.G2019S) mutants upon the addition of mitophagy modulators. **B.** Absolute quantification of autophagic vacuoles in healthy control, PINK1(p.I368N), VPS35(p.D620N) and LRRK2(p.G2019S) mutants upon the addition of mitophagy modulators. Oligomycin (oligo) and valinomycin (val). Kruskal-Wallis and Dunn's multiple comparison test for all cell types with respect to its reference (ref) basal condition. Significance levels are * $p < 0.05$, ** $p < 0.01$, *** $p < 0.001$, and **** $p < 0.0001$.

2-14 Definition of autophagy fingerprints in control and PD mutants

As hypothesized, the pharmacological tests described above define responsiveness patterns, or fingerprints, and establish global relationships between the PD mutants. Heatmap clustering analysis for phagophores and autophagic vacuoles was conducted for all the lines and all the conditions used. The analysis demonstrated a distinctive branch for chemical perturbations for the healthy control line (Figure 2-14 A). Interestingly, VPS35(p.D620N) and PINK1(p.I368N) clustered together in a different branch enriched in PD mutants (Figure 2-14 A). The basal conditions for LRRK2(p.G2019S) clustered in the healthy control branch (Figure 2-14 A). However, upon stress perturbations the LRRK2(p.G2019S) autophagic patterns clustered in the mutant branch. This suggests an increased susceptibility in LRRK2(p.G2019S) mutant for autophagy or mitophagy-stress perturbations. Importantly, conditions that demonstrated rescue for mutants lines, as shown by rapamycin for PINK1(p.I368N) mutant, grouped in the healthy control line branch. Overall, these results indicate there are distinctive autophagic staging fingerprint alterations in the studied PD mutants.

Figure 2-14

A

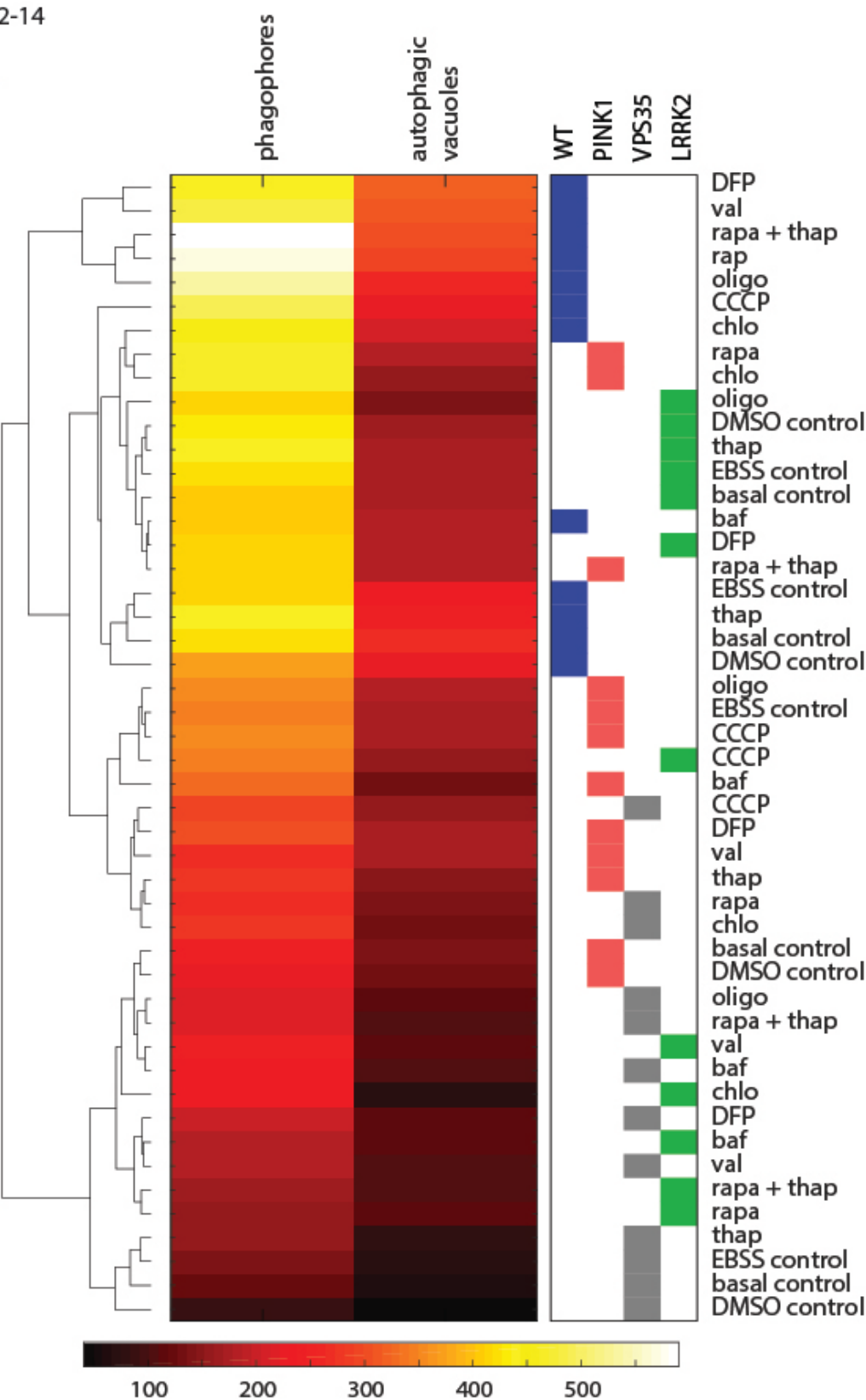


Figure 2-14. Definition of autophagy fingerprints in control and PD mutants. A. Heatmap clustering for healthy control and mutant lines across all mitophagy and autophagy modulating treatments. Valinomycin (val), rapamycin (rapa), thapsigargin (thap), oligomycin (oligo), chloroquine (chlor), bafilomycin (baf). Color scale in absolute event frequency.

2-15 Quantification of mitochondria network and mitophagic vacuole volume

Mitochondrial network and mitophagic vacuole volumes were quantified for healthy control and mutant lines (Figure 2-15). The mitochondria network volume of PINK1(p.I368N) mutant was significantly higher than healthy control cells (Figure 2-15 A-B). This characteristic is in agreement with previous reports that show elongated mitochondria for PINK1 inactivation mutants, as PINK1(p.I368N) (Yu et al., 2011). In contrast, VPS35(p.D620N) and LRRK2(p.G2019S) mutants presented significantly decreased mitochondrial network volumes (Figure 2-15 A-B). This observation is in agreement with previous reports, which demonstrated that LRRK2 mutants have fragmented mitochondria (Su and Qi, 2013). The autophagic vacuoles resulting from mitophagy events are defined as mitophagic vacuoles. Next, the properties of the mitophagic vacuoles resulting from such abnormal mitochondria networks was evaluated. In agreement with the previous results of mitochondrial network volume, there was an increased volume for PINK1 mutant in comparison to healthy control (Figure 2-15 A-C). Likewise, LRRK2 mitophagic vacuoles presented smaller volumes, consistent with a reduced mitochondrial network volume and fragmented mitochondria (Figure 2-15 A-C). Overall, these results are logical in relation to the steps of the mitophagy pathway. Since autolysosomes that process mitochondria are downstream of mitochondria, mitophagic vacuole volumes follow the same pattern as mitochondria. Hence, for both parameters healthy control and VPS35(p.D620N) presented similar volumes (Figure 2-15 B-C).

Figure 2-15

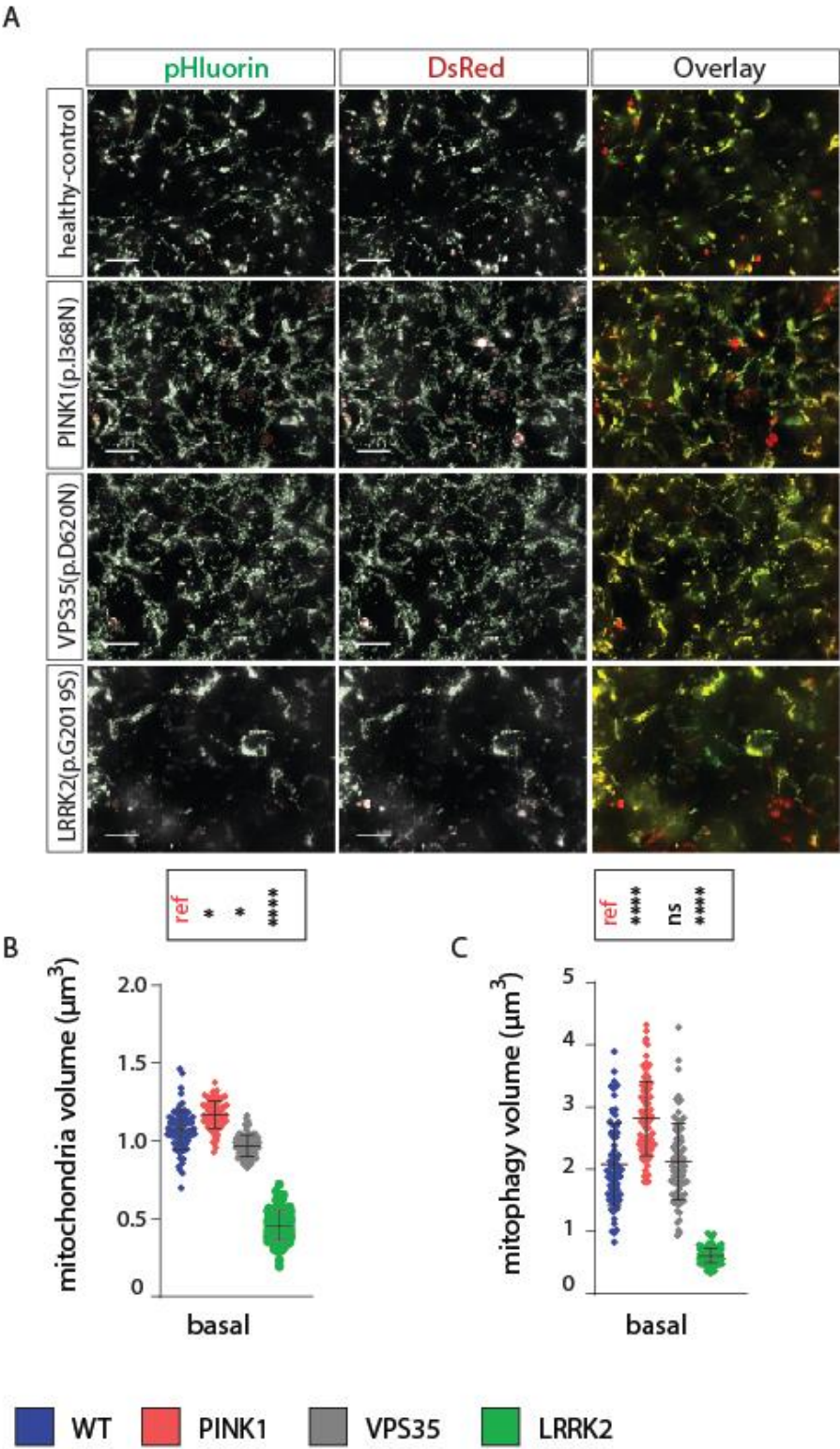


Figure 2-15. Quantification of mitochondria network and mitophagic vacuole volume. A. Representative images of ATP5C1-Rosella reporter lines for healthy control and mutants. Mitochondria network mask on green perimeter and mitophagic vacuole mask on red perimeter. Scale bar indicates 20 μ m. **B.** Mitochondrial volumes for each line in basal conditions. Kruskal-Wallis and Dunn's multiple comparison tests were performed for all the lines with respect to the healthy control reference (ref). **C.** Mitophagy volumes for each line in basal conditions. Kruskal-Wallis and Dunn's multiple comparison tests were performed for all the lines with respect to healthy control reference (ref). Significance levels are * $p < 0.05$, ** $p < 0.01$, *** $p < 0.001$, and **** $p < 0.0001$.

2-16 Evaluation of the mitophagy levels

Section 2-13 described the results of autophagy reporter Rosella-LC3 lines when exposed to mitochondria stressing agents. Here, the mitophagy levels are presented as direct measurement from the mitophagy reporter ATP5C1-Rosella for each mutant line in basal and stressed conditions. Mitophagy is a sub-component of general autophagy; therefore increase in its levels influence the overall degradation capacity. Analysis of the mitophagy levels further complement the observations of the general autophagy reporter lines. The validated mitochondria stressor CCCP provided robust results in the autophagy assays, therefore it was used as a mitophagy-inducing agent for quantification. In basal conditions, all mutants presented higher mitophagic vacuole frequencies than healthy control (Figure 2-16 A). Furthermore, CCCP-stressed healthy control mutant presented mitophagy levels similar to mutants in basal conditions (Figure 2-16 A). Accordingly, CCCP-stressed mutants presented mitophagy levels exceeding healthy control stressed levels (Figure 2-16 A). Stressed mutants reached a mitophagy level of approximately two fold that of stressed healthy control (Figure 2-16 A).

Figure 2-16

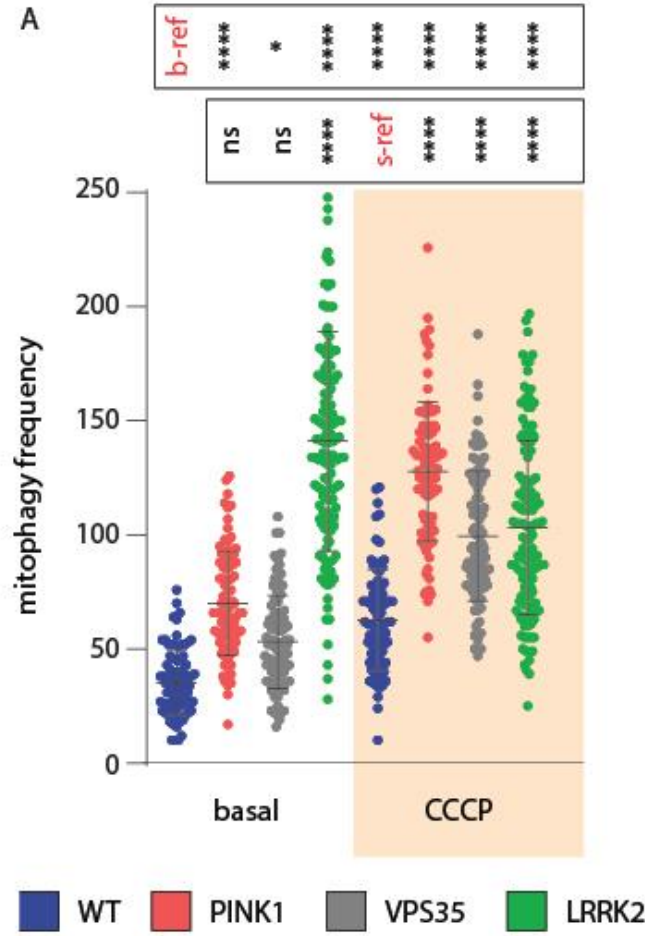


Figure 2-16. Evaluation of the mitophagy levels. A. Mitophagy frequencies for all lines in basal conditions and after mitochondrial stress induction. Kruskal-Wallis and Dunn's multiple comparison tests were performed for all the lines with respect to the basal healthy control reference (b-ref) and stressed healthy control reference (s-ref). Significance levels are * $p < 0.05$, ** $p < 0.01$, *** $p < 0.001$, and **** $p < 0.0001$.

2-17 Distribution of autophagy resources upon mitochondrial stress: mitophagy, non-mitochondrial autophagy, and general autophagy

Section 2-13 described the modulation of general autophagy. Those results summarized conditions upon mitochondrial stress induction and were obtained using the autophagy reporter Rosella-LC3 lines. They demonstrate the combined effect on non-mitochondrial autophagy and mitophagy. Furthermore, **section 2-16** presented the modulation of mitophagy levels. Those results presented conditions upon mitochondrial stress induction and were obtained using the mitophagy reporter ATP5C1-Rosella lines. Non-mitochondrial autophagy is determined by subtracting the ATP5C1-Rosella data (**section 2-16**) from the Rosella-LC3 data (**section 2-13**). Here, those analyses are combined to establish a consolidated overview of both general autophagy and mitophagy. In addition, the way in which the autophagic resources are distributed upon mitochondria perturbations is evaluated. Upon stress induction in healthy control cells, the frequency of autophagic vacuoles was reduced to 70% and mitophagy increased to 170% (Figure 2-17 A). The frequency of general autophagy increased to 380% in VPS35(p.D620N) cells (Figure 2-17 A). The frequency of mitophagy in the VPS35(p.D60N) mutant indicates that general autophagy was primarily dedicated to degradation of mitochondria in basal conditions (Figure 2-17 A). Similarly, the mitophagy level increased to 180% for PINK1(p.I368N) cells. The absolute frequency of general autophagy for PINK1(p.I368N) increased to 140% (Figure 2-17 A).

Figure 2-17

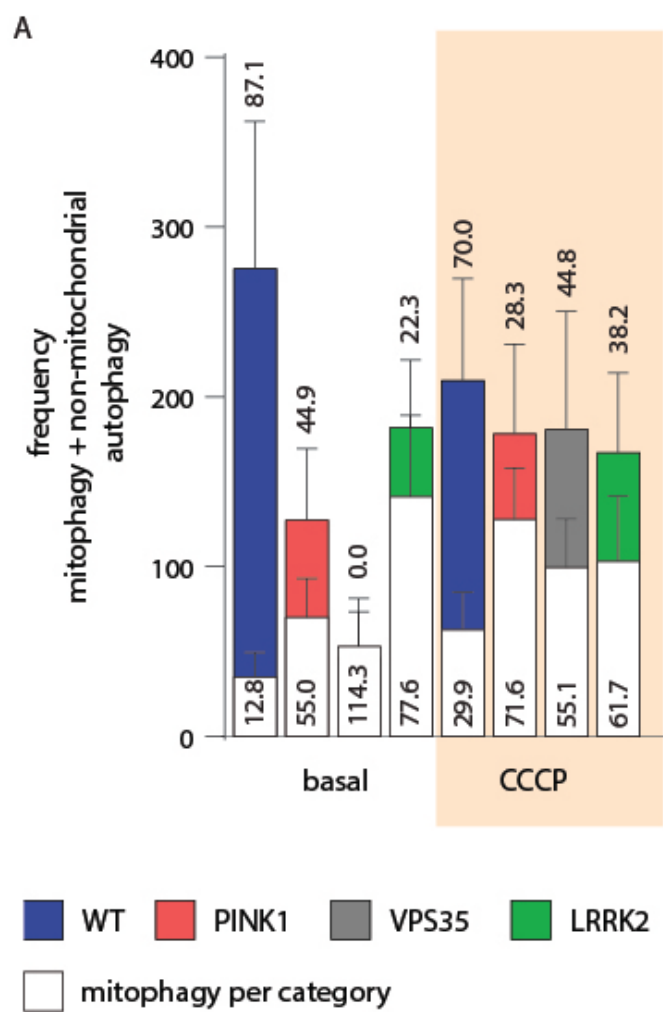


Figure 2-17 Distribution of autophagy resources upon mitochondrial stress: mitophagy, non-mitochondrial autophagy, and general autophagy. A. Mitophagy and non-mitochondrial autophagy fractions for each line before and after mitochondria stress induction. Percentages for mitophagy and non-mitochondrial autophagy are indicated on each bar section. This figure corresponds to a composition analysis of **section 2-13** and **section 2-16**.

2-18 Evaluation of lysosome capacity in control and mutant lines

The acidification of autophagosomes depends on lysosomal fusion. Therefore, the progression through autophagy is affected by the reservoir of lysosomes. Correspondingly, the pool of lysosomes is reduced by increased speed of autophagic flow when lysosome synthesis is constant. To determine the acidification capacity of control and mutant lines, the autophagy and mitophagy reporter lines were combined with lysosomal dyes (Figure 2-18 A). For this purpose, lysosome quantification algorithms were developed and described in **section 2-7**. This allowed for the determination of the acidification capacity available for the autophagic vacuoles (Figure 2-18 A). The lysosome frequency in PINK1(p.I368N) mutant was elevated in comparison to healthy control cells (Figure 2-18 B). In contrast, the VPS35(p.D620N) mutant presented decreased lysosome frequency (Figure 2-18 B) with the LRRK2(p.G2019S) mutant showing similar lysosome frequencies to the healthy control cells (Figure 2-18 B). Next, the lysosome diameter was evaluated for control and mutant lines. If lysosome luminal pH is similar across lines, the diameter and frequency account for the overall cellular acidification capacity. The analysis revealed reduced lysosome size for all the mutants compared to healthy control cells (Figure 2-18 C). In addition, the diameter of autophagic vacuoles was quantified. These results revealed that VPS35(p.I368N) cells present larger autophagic vacuoles than healthy control cells (Figure 2-18 D). The combination of these factors - reduced lysosome frequency with reduced lysosomal volume and increased autophagic vacuole volume - could result in decreased acidification of autolysosomes in the VPS35(p.I368N) mutant (Figure 2-18 B-D).

Figure 2-18

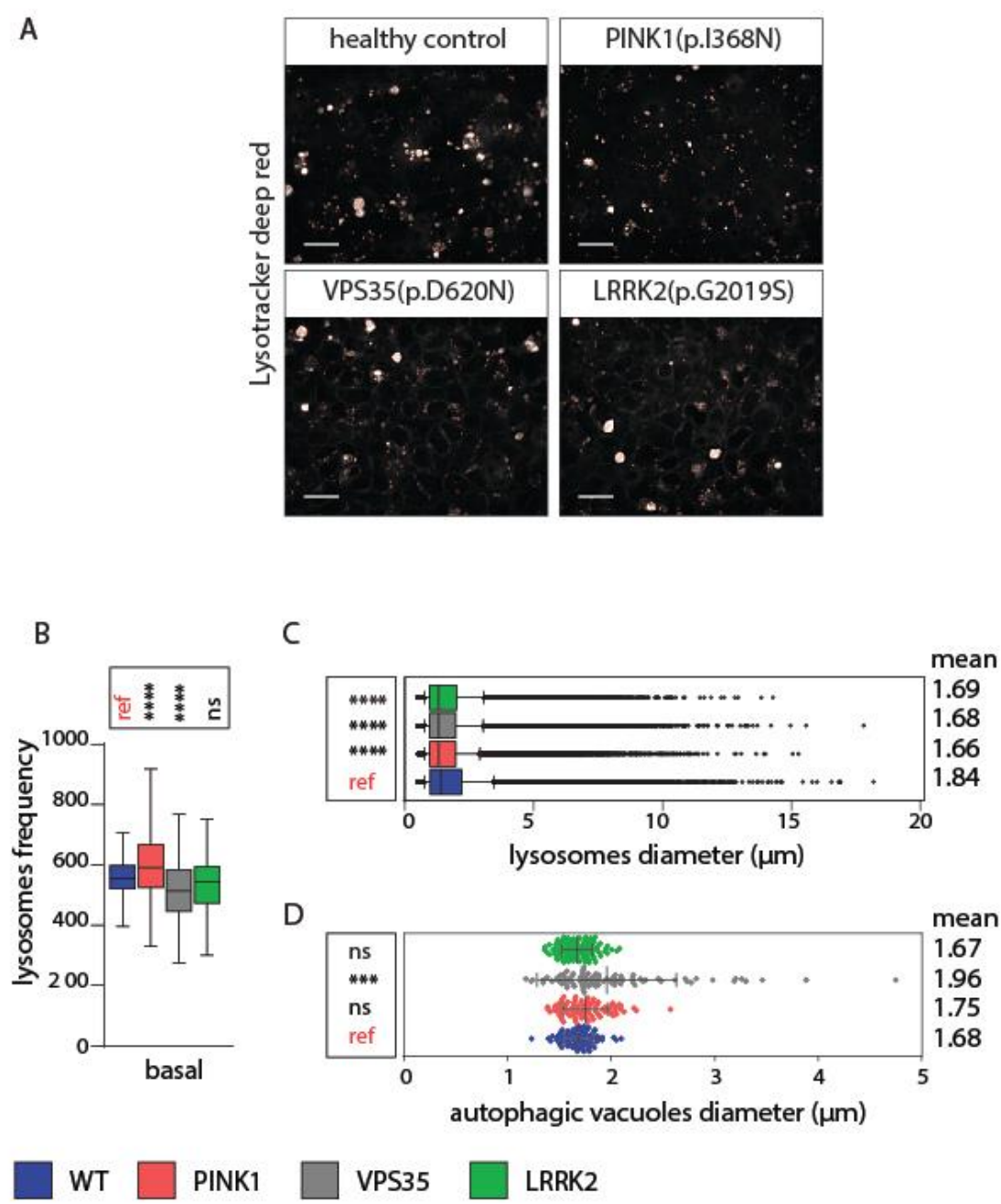


Figure 2-18. Evaluation of lysosome capacity in control and mutant lines. **A.** Representative lysotracker staining for healthy control and mutant lines. Lysosome mask on red perimeter. Scale bar indicates 20 μ m. **B.** Lysosome frequency for each line in basal conditions. One way ANOVA and Dunnett's multiple comparison tests were performed for all the lines with respect to the healthy control reference (ref). **C.** Lysosome diameter for healthy control and mutants. Percentiles 10 to 90 are represented in the boxplot range. Non-parametric Kruskal-Wallis test ($p<0.0001$) and Dunn's multiple comparison test were performed for all the lines with respect to the healthy control reference (ref). **D.** Autophagic vacuole diameter for healthy control and mutants. Non-parametric Kruskal-Wallis and Dunn's multiple comparison tests were performed for all the lines with respect to the basal healthy control reference (ref). Significance levels are * $p<0.05$, ** $p<0.01$, *** $p<0.001$, and **** $p<0.0001$.

第三章

Chapter 3

結論及び考察 1

Conclusion & Discussion 1

In this work, the development of two recent technologies are utilized: genome editing on human iPS cells, and genetically encoded pH sensors. This enables the evaluation of the autophagy and mitophagy activity of a set of healthy control and PD-associated mutants. Complete reconstruction of the autophagy and mitophagy pathways were achieved using the LC3 and ATP5C1-bound pHluorin sensors. Interestingly, an active autophagy and mitophagy pathway was observed in this early developmental state. In basal conditions, there were abundant autophagic and mitophagic structures. Furthermore, time-lapse microscopy allowed for the visualization of the distribution of autophagic resources during cell division. These observations are in agreement with previous studies that demonstrate essential roles of autophagy pathways during pre-implantation development (Tsukamoto et al., 2008), maintenance of pluripotency, and resistance to senescence.

Reports from the autophagy community have highlighted the need to develop tools to define pathway stages and quantification of their structures (Klionsky et al., 2016). This is essential to draw correct interpretations from the phenotypic traits observed. In this work a set of algorithms was developed to automatically, and, in a high-throughput manner, identify autophagic and mitophagic structures using high-content microscopy imaging technology. Namely, these structures are phagophores, autophagosomes, early autolysosomes, late autolysosomes, mitochondria network, mitophagic vacuoles, and lysosomes. Furthermore, the algorithms allowed the identification of properties such as frequency, diameter, volume, eccentricity and intensity ratio. Overall, this achieved a resolution on autophagy and mitophagy composition not reached before by conventional or high-throughput methods.

The sensitivity of the platform was evaluated using a set of well-characterized modulators of autophagy (Allen et al., 2013; Galluzzi et al., 2017). The selection of compounds used

modulated autophagy and mitophagy at different stages of the pathway. This setup compared the experimental observations with previous reports and evaluated well-described pathway mechanisms (Galluzzi et al., 2017). The assortment of compounds used can be classified in four groups: (1) autophagosome-autolysosome blockers, (2) phagophore formation modulators, (3) PINK1-dependent mitochondria stressors, and (4) PINK1-independent mitochondria modulators. The patterns observed reproduced the well-described mechanisms for all the categories.

When comparing the healthy control and PD mutants in basal conditions, a reduced autophagic capacity was observed in all mutants as accounted by the absolute frequency of phagophores, autophagosomes, early autolysosomes and late autolysosomes. The evaluation of the autophagy rate constant demonstrated a reduced capacity to progress through the autophagy pathway for LRRK2(p.G2019S) and VPS35(p.D620N) mutants. Although the absolute frequency of autophagic structures for the PINK1(p.I368N) mutant was lower than healthy control, the proportion of phagophores to autophagic vacuoles was similar between them.

The evaluation of the autophagosome-autolysosome blockers bafilomycin and chloroquine demonstrated that healthy control, PINK1(p.I368N) and VPS35(p.D620N) can build up phagophore resources upon blockage of autophagy progression. In contrast, LRRK2(p.G2019S) mutant presented an increased sensitivity to the blockage and resulted in further decrease of phagophore levels compared to its basal condition. Evaluation of the phagophore formation modulators thapsigargin and rapamycin demonstrated that mutants are responsive to both an increase via the CaMK- β /AMPK pathway activation and mTOR pathway repression. Remarkably, PINK1(p.I368N) phagophore levels reached healthy control levels upon mTOR

inhibition. This result indicates that modulators of mTOR are potential rescue candidates for autophagy-related traits in PINK1 mutants. Similarly, rapamycin further increased the phagophore level in healthy control. The evaluation of PINK1-dependent and independent mitochondria stressors demonstrated that PINK1(p.I368N) and VPS35(p.D620N) increased the phagophore levels with respect to their basal conditions. This observation indicates that their basal phagophore resources are not sufficient to cope with the increasing mitochondria degradation demand. In agreement with previous reports, healthy control, PINK1(p.I368N), and VPS35(p.D620N) were able to increase autophagic vacuole levels in response to mitochondria stress. Consolidation of the compound dataset analysis using clustering analysis demonstrated that the basal LRRK2(p.G2019S) pattern groups within the healthy control branch and, upon stress induction, shifts towards the mutant branch. Conversely, basal PINK1(p.I368N) pattern groups in the mutant branch and upon treatment with mTOR inhibitor or other phagophore builder compounds shifts toward the healthy control branch.

The analysis of mitochondria network and mitophagic vacuoles demonstrated that PINK1(p.I368N) mutant presents increased mitochondria volume, in agreement with previous reports that linked elongated mitochondria to *PINK1* loss of function (Yu et al., 2011). Such elongated mitochondria result in mitophagic vacuoles with higher volumes compared to healthy control and might result in reduced acidification capacity of the vacuoles. Conversely, LRRK2(p.G2019S) mutant displayed reduced mitochondria network volume. This observation confirms reports that associate *LRRK2* mutations with fragmented mitochondria (Su and Qi, 2013). Such fragmented mitochondria resulted in mitophagic vacuoles with reduced volume. Comparisons of the mitophagic vacuole frequencies demonstrated that all mutants present higher basal levels when compared to healthy control. Furthermore, the stressed healthy control is lower or similar to the mutants. This suggests a higher demand for mitochondria

degradation under basal conditions. A continuous state of high degradation demand might result in an overall decrease in the autophagic resources if *de novo* synthesis of autophagic structures is impaired. Combined analysis of autophagy, mitophagy, and their ratio demonstrated that mitophagic resources impose a higher energetic demand. This observation is supported by a consequential loss of energy-generating mitochondrial volume. The mutant lines presented an overall higher proportion of mitophagy than autophagy.

The inclusion of lysosomal dyes to the autophagy and mitophagy analysis gives further insight into potential phenotypic interpretations. The lysosome frequency for VPS35(p.D620N) mutant was lower. Furthermore, its volume was lower than healthy control and its autophagic vacuoles presented higher volumes compared to all lines. These observations demonstrate that VPS35 mutant presents a significantly reduced acidification capacity and suggests that modulation of lysosome pathways could alleviate the phenotypic traits present in this mutant. Remarkably, all the mutants presented smaller lysosome volumes compared to healthy control. This global reduction in lysosome volume and acidification capacity could be a direct or indirect consequence of the mutations.

Currently, the autophagy field faces the challenge of identifying the different stages of autophagy and mitophagy in a high-throughput manner (Klionsky et al., 2016). The steps and sub-cellular structures of autophagy and mitophagy are important for the proper interpretation of phenotypic traits. This compartmentalization cannot be accounted for when using bulk population analysis techniques such as western blotting. Here, a platform that accounts for vesicular compartmentalization was developed. The platform uses unbiased automated analysis in combination with automated high-content imaging, providing high statistical power and assay sensitivity. The autophagy and mitophagy staging analyses

highlighted that the mutations LRRK2(p.G2019S), VPS35(p.D620N) and PINK1(p.I368N) not only share autophagy and mitophagy homeostasis impairments as a common trait characteristic of PD but also reveal mutant-specific phenotypic fingerprints.

While the present study focused on the development of autophagy staging in PD, it should be noted that the methodology could be leveraged for autophagy research on other metabolic pathologies. Due to the substantial level of automation, this platform can be used for genetic and chemical screening and thereby accelerate current endeavors in precision medicine.

第四章

Chapter 4

結果 2

Results 2

4-1 Fluorescent proteins – SNP pairs enable achievement of deterministic genotype outcomes

Homology-directed repair allows for the integration a selection module cassette alongside a designer mutation (Figure 4-1 A). The use of a donor pair, containing different fluorescent protein reporter cassettes associated with a defined SNP enables outcomes of a known genotype (Figure 4-1 B). The deterministic genotype outcomes include: heterozygous, homozygous healthy, and homozygous pathogenic (Figure 4-1 B). One-step biallelic targeting occurs with a mean frequency of 37.5% using dsDNA donor vectors (Table 1). Such high frequency allows the purification of biallelic-targeting events, as defined above (Figure 4-1 B). Moreover, the incorporation of a tagBFP-negative selection module excludes random integration events (Figure 4-1 C). Pathologic mutations on the *SNCA* gene are dominant, and are therefore of heterozygous genotype (Bozi et al., 2014; Kruger et al., 1998). Two well-defined *SNCA* mutations are *SNCA* p.A30P and *SNCA* p.A53T. Those mutations are located far from each other in different exons, namely exon 2 and exon 3. Hence, two pairs of donors with heterozygous a combination were produced as described above and matching the design of population type 1A (Figure 4-1 B). The heterozygous combinations in *SNCA*-mutant donors contain rs104893878 (p.A30P), and rs104893877 (p.A53T). In the case of *SNCA* exon 2, an EGFP-mutant donor carried the transversion c.88g>c. Likewise for *SNCA* exon 3, an EGFP-mutant donor carried the transition c.209g>a. For both loci a corresponding dTOMATO wild-type donor was included. After the knock-in and antibiotic selection tagBFP^{pos} random integrations events were excluded from the polyclonal population using FACS (Figure 4-1 D). In the non-random-tagBFP^{neg} population, a similar reporter expression level was observed from both alleles in chromosome 4, *SNCA* gene (Figure 4-1 E). This is evidenced by a proportion of ~50% for both EGFP^{pos} and dTOMATO^{pos} populations in the FACS analysis (Figure 4-1 E).

Figure 4-1

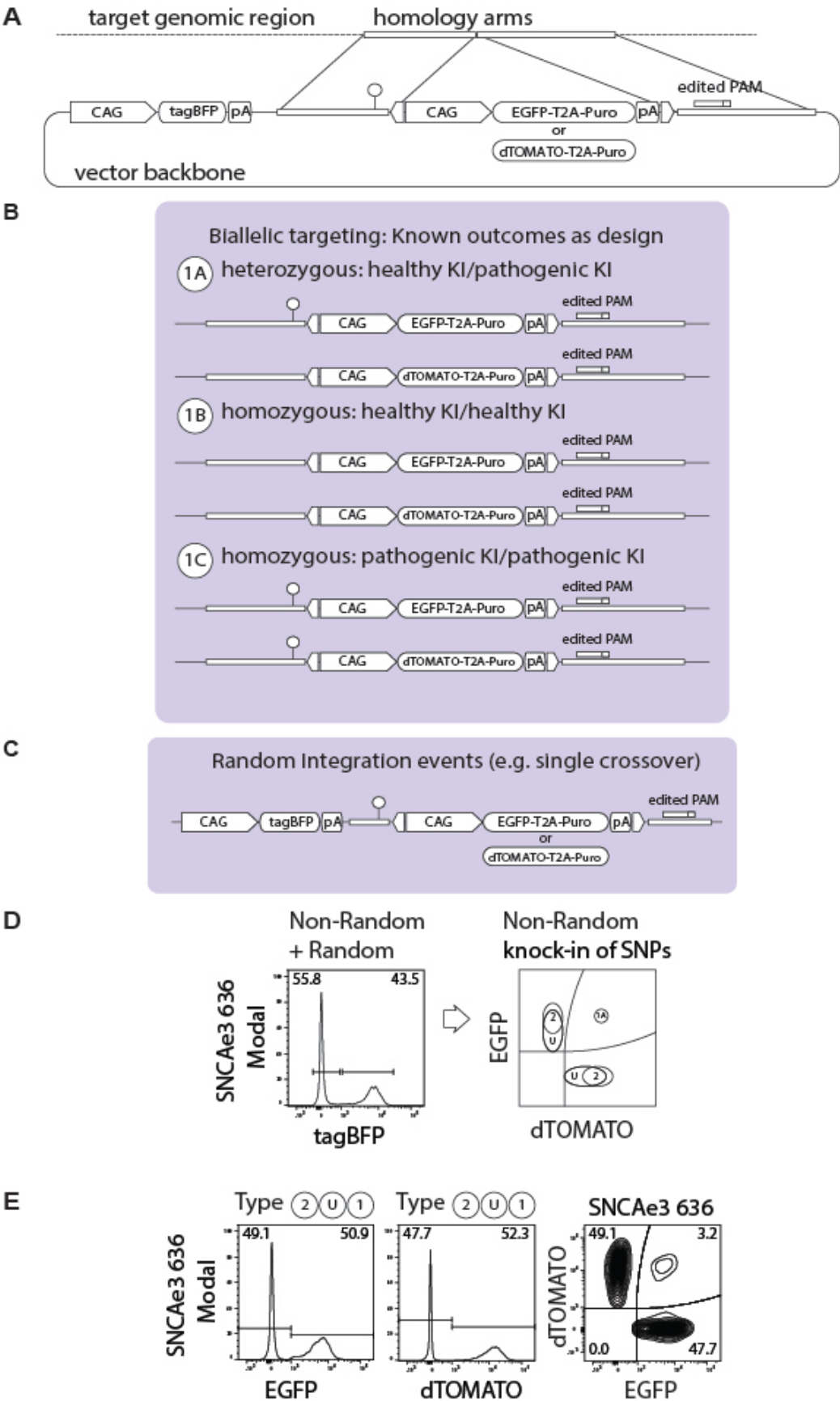


Figure 4-1 Fluorescent proteins – SNP pairs enable achievement of deterministic genotype outcomes. **A.** Standard donor vector structure. It contains a fluorescent-positive selection module expressing EGFP or dTOMATO, and a negative selection module expressing tagBFP. Positive selection modules contain a puromycin resistance gene (Puro). **B.** Outcomes of the derived population are defined according to donor vector combination design. Knock-in (KI). **C.** The tagBFP negative selection module allows removal of random integration events, assisting in the derivation of defined outcomes. **D.** Representative example of *SNCA* exon 3 polyclone 636. Random integration tagBFP^{pos} cells are excluded from the correctly edited on-target cells tagBFP^{neg}. **E.** Representative example of *SNCA* exon 3. On-target EGFP^{pos} and dTOMATO^{pos} cells include homozygous populations, EGFP^{pos}/EGFP^{pos} and dTOMATO^{pos}/dTOMATO^{pos} (type 2), and heterozygous populations of undefined second-allele state EGFP^{pos}/WT-NHEJ or dTOMATO^{pos}/WT-NHEJ (type U). Wild type (WT).

Table 1. Biallelic targeting frequency

Polyclone sample	Frequency composed biallelic (a)	Frequency single channel biallelic (b)	Frequency total biallelic (c)
<i>SNCA</i> exon 3 636	0.032	0.179	0.390
<i>SNCA</i> exon 2 630	0.021	0.145	0.311
<i>SNCA</i> exon 2 632	0.022	0.148	0.319
<i>SNCA</i> exon 3 634	0.056	0.237	0.529
<i>SNCA</i> exon 3 636	0.012	0.110	0.231
<i>PINK1</i> exon 5 517	0.033	0.182	0.396
<i>PINK1</i> exon 5 526	0.042	0.205	0.452
Mean total			0.375

(a) Frequency composed biallelic is defined as the experimentally measured EGFP^{pos}/dTOMATO^{pos} population.

(b) Frequency of single channel biallelic represents the EGFP^{pos}/EGFP^{pos} and dTOMATO^{pos}/dTOMATO^{pos} populations separately, calculated as $\sqrt{\text{frequency composed biallelic}}$.

(c) Frequency total biallelic corresponds to frequency composed biallelic + 2*frequency of single channel biallelic.

4-2 Similar reporter expression levels are achieved in different genomic regions

In order to test whether similar expression levels occur in other genomic regions, the gene *PINK1* of chromosome 1 was targeted. A well-characterized *PINK1* mutation is p.I368N, which affects its stability and kinase activity (Ando et al., 2017). The mutation coding p.I368N is located in exon 5 of the *PINK1* gene. In contrast to PD patients with *SNCA* mutations, *PINK1* PD patients are homozygotes or compound heterozygotes (Ishihara-Paul et al., 2008). Hence, the target population for the *PINK1* mutant corresponds to type 1C from the previous section (Figure 4-1 B). For *PINK1* exon 5, both EGFP and dTOMATO donors carried the pathogenic transversion c.1197t>a. The alleles of chromosome 4 *SNCA* exon 2, chromosome 4 *SNCA* exon 3 and chromosome 1 *PINK1* exon 5 showed similar reporter expression levels as evidenced by comparative FACS analysis (Figure 4-2 A-B). The ratio of EGFP to dTOMATO was ~50% in all cases analyzed, which is consistent with a comparable efficiency for both donors. The quantifications were conducted independently and used different sgRNAs (Figure 4-2 A-B). Furthermore, the biallelic targeted populations separated clearly from the other genotype populations in both genes (Figure 4-2). These results validate the presented approach to purify biallelic-targeted populations of known genotype, in different genomic regions. For all FACS experiments, it was essential to ensure single cell gating structures (Figure 4-2 D) and single cell sample preparation (Figure 4-2 E).

Figure 4-2

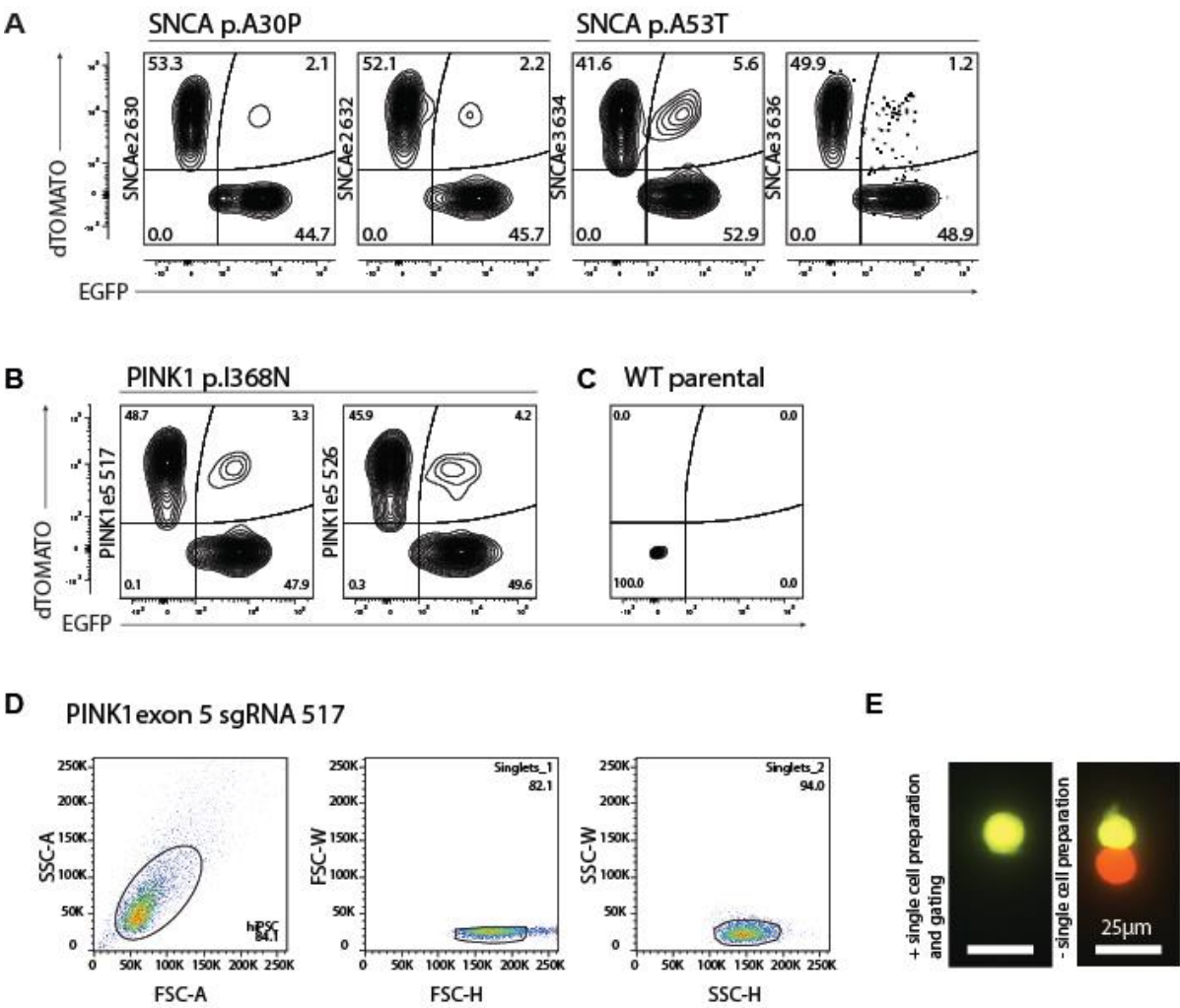


Figure 4-2. Similar reporter expression levels are achieved in different genomic regions. A.

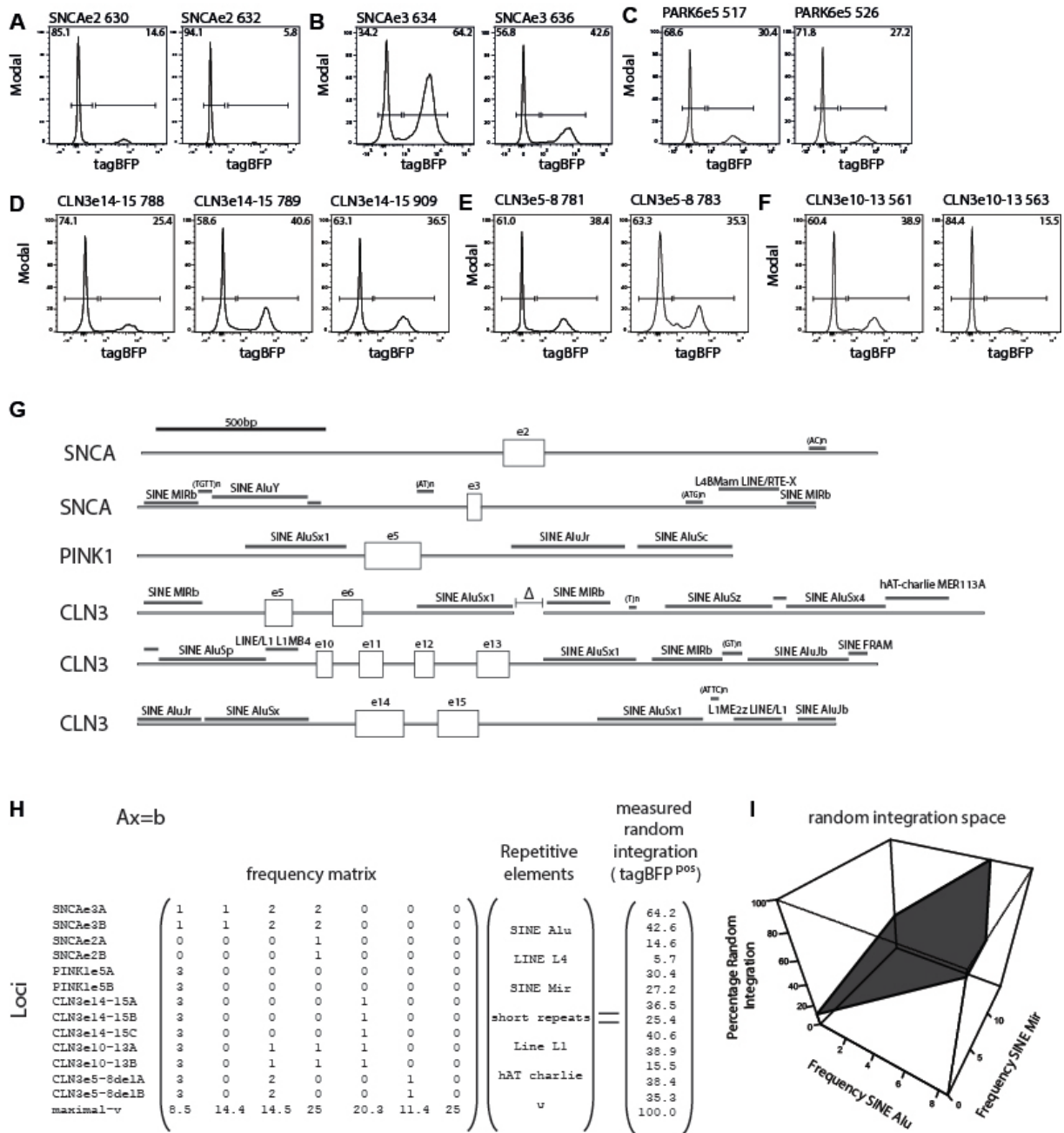
Post-selection sorting of double-positive biallelic edited cells for *SNCA* exon 2 and *SNCA* exon 3 using independent sgRNAs: sgRNA 630, sgRNA 632, sgRNA 634 or sgRNA 636. FACS plots are represented with 2% contour lines. For *SNCA* exon 3 sgRNA 636, a dot plot is included to show the distribution of 1.2% of Q2. **B.** Post-selection sorting of double-positive biallelic edited cells for *PINK1* exon 5, using independent sgRNAs: sgRNA 517 and sgRNA 526. FACS plots are represented with 2% contour lines. **C.** Wild-type parental control. **D.** Representative hierarchical single cell gating structure of SSC and FSC wide and high for single cell preparations. Example for *PINK1* exon 5 sgRNA 517 polyclone. **E.** Single cell preparation of cells and single cell gating structure is essential to ensure high quality sorting. Scale bar indicates 25µm.

4-3 Repetitive elements reduce on-target genome editing efficiency by increasing random integration

Linear DNA has been previously associated with increased frequency of random integration. Hence, silent point mutations were introduced in one or several PAM sequences of donors to protect the template DNA from CRISPR-Cas9-induced linearization. Consequently, properly targeted alleles are protected from secondary CRISPR-Cas9 cleavage events and the risk of on-target indels is eliminated (Merkle et al., 2015). As mentioned in **section 4-1**, the inclusion of tagBFP in the negative selection module allowed quantification, visualization, and exclusion of random integration events (Figure 4-1 C). The tagBFP negative selection module avoids bystander toxicity or incomplete negative selection from systems such as thymidine kinase (Ruby and Zheng, 2009). The percentage of tagBFP^{pos} random integration ranged from 5.8-14.6% for *SNCA* exon 2, from 42.6-64.2% for *SNCA* exon 3, and from 27.2-30.4% for *PINK1* exon 5 (Figure 4-3 A-C). The extent of random integration correlated with the type and proportion of repetitive elements present in the homology arms of the donors. Random integration was assessed using donors for six genomic regions with known repetitive element compositions and by testing twelve sgRNAs. The loci evaluated include chromosome 1 *PINK1* exon 5, chromosome 4 *SNCA* exon 2, *SNCA* exon 3, chromosome 16 *CLN3* exon 5-8, *CLN3* exon 10-13, and *CLN3* exon 14-15 (Figure 4-3 G). Analysis of a linear optimization model was performed using the form $Ax=b$ (Figure 4-3 H). The matrix A corresponded to the frequency of repetitive elements in the homology arms (Figure 4-3 G). Vector x corresponded to both the type of repetitive elements present in the analyzed dataset (Figure 4-3 G) and a variable of all non-included repetitive elements (upsilon: υ). Vector b corresponded to the experimentally measured random integration level, given by the percentage of TagBFP^{pos} cells (Figure 4-3 A-F). Based on this, a model to predict random integration frequency intrinsic to the composition

of repetitive elements in the homology arms (Figure 4-3 H-I) was derived. The solution permitted the assignment of weight coefficients to each repetitive element. The value of each weight coefficient indicates which repetitive element contributes the most to the random integration frequency observed. The solution space is constrained for a maximum of 100% random integration and sequence length physical boundaries for each repetitive element. The optimization solution indicates that the most relevant repetitive elements correspond to the SINE family, specifically Alu and Mir (Figure 4-3 H-I). This result indicates that repetitive elements, especially from the SINE family, should be avoided in the homology arms used for genome editing.

Figure 4-3



Predicted random

$$PR = \alpha(RE1) + \beta(RE2) + \gamma(RE3) + \dots + \delta(REn) + C$$

$$PR = 10.0978(\text{SINE Alu}) + (0)(\text{LINE L4}) + (1.746)(\text{SINE Mir}) + (0)(\text{short repeats}) + (0)(\text{Line L1}) + (0)(\text{hAT charlie}) + (0)(u) + C$$

$$PR = 10.0978(\text{SINE Alu}) + (1.746)(\text{SINE Mir}) + C \quad \text{with } C=10.15$$

Figure 4-3. Repetitive elements reduce on-target genome editing efficiency by increasing random integration. **A.** Flow cytometry histogram for tagBFP *SNCA* exon 2 sgRNA 630 and 632. **B.** *SNCA* exon 3 sgRNA 634 and 636. **C.** *PINK1* exon 5 sgRNA 517 and 526. **D.** *CLN3* exon 14-15 sgRNA 788, 789 and 909. **E.** *CLN3* exon 5-8 sgRNA 781 and 783. **F.** *CLN3* exon 10-13 sgRNA 561 and 563. **G.** Distribution and type of repetitive elements in the homology arms of the dsDNA donors for *SNCA* exon 2, *SNCA* exon 3, *PINK1* exon 5, *CLN3* exon 5-6, *CLN3* exon 10-13 and *CLN3* exon 14-15. **H.** Predictive model for random integration. The predictive model PR uses the matrix of repetitive element frequency in the homology arms A, the repetitive elements vector x , and the observed incidence of tagBFP^{pos} random integration b . The mathematical model generates coefficients for each repetitive element and the constant of the system for random integration prediction. **I.** The space of non-zero coefficients derived from **H**: SINE Alu and SINE Mir, allows inferring expected random integration frequencies.

4-4 FACS purification increases speed and yield of isogenic derivation

As showed in **section 4-2**, the initial percentage of double-positive EGFP^{pos}/dTOMATO^{pos} cells ranged from a mean 2.15% for *SNCA* exon 2, 3.4% for *SNCA* exon 3 to 3.75% for *PINK1* exon 5 (Figure 4-2). One sorting step yields a population of up to $\sim 3 \times 10^5$ EGFP^{pos}/dTOMATO^{pos} cells (Figure 4-4 A). The gating position of the double-positive population afforded nearly complete purity with either only one sorting step or a two-stage sorting for yield and subsequently for purity (Figure 4-2). Purification and expansion yielded a biallelic targeted population EGFP^{pos}/dTOMATO^{pos} (Figure 4-4 B). Culture of such cells presented homogenous fluorescence (Figure 4-4 C). Sanger sequencing of biallelic targeted *SNCA* mutations demonstrated 1) the heterozygous integration of the pathogenic SNP rs104893878 (p.A30P) and rs104893877 (p.A53T) in each polyclone, 2) the homozygous integration of the edited PAM, and 3) the transition from genome to positive selection module (Figure 4-4 D-E). Isolation of single clones from the polyclonal populations and sequencing allowed the analysis of composition and a quantified assessment of the specificity of the process (Figure 4-4 F).

Figure 4-4

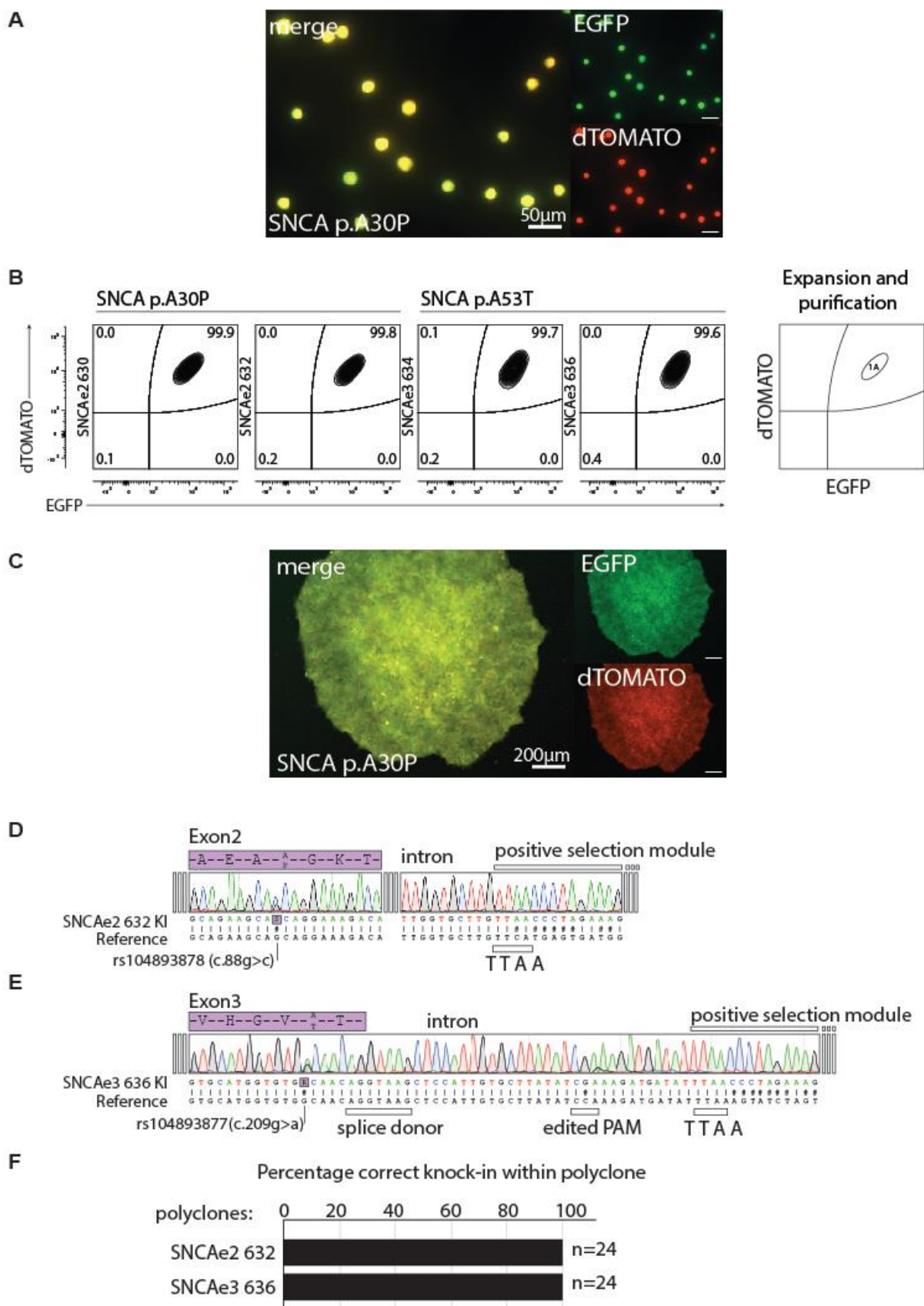


Figure 4-4. FACS purification increases speed and yield of isogenic derivation. **A.** Microscopy of post sorted EGFP^{pos}/dTOMATO^{pos} cells. Single cell gating structures yields high purity biallelic edited cells. Representative example for *SNCA* exon 2 p.A30P polyclone 632. Scale bar indicates 50µm. **B.** FACS analysis for yield-purity and purity-purity post-expansion cultures. Sorting of double-positive biallelic edited cells for *SNCA* exon2 and *SNCA* exon 3 using independent sgRNAs: sgRNA630, sgRNA632, sgRNA634 or sgRNA636. FACS plots are represented with 2% contour lines. **C.** Representative EGFP^{pos}/dTOMATO^{pos} culture after sorting. Biallelic edited cells generate homogenous knock-in cultures. Representative example for *SNCA* exon 2 p.A30P polyclone 632. Scale bar indicates 200µm. **D.** Sanger sequencing chromatogram of *SNCA* exon 2 p.A30P polyclone 632 knock-in. Knock-in (KI). **E.** Sanger sequencing chromatogram of *SNCA* exon 3 p.A53T polyclone 636 knock-in. **F.** Analysis of the respective polyclones composition.

4-5 Transposase-mediated generation of footprint-free isogenic lines

The positive selection modules in each EGFP^{pos}/dTOMATO^{pos} polyclone are flanked by internal terminal repeats from the piggybac transposon type. The positive selection modules were excised using a codon-optimized hyperactive and excision-only variant (R372A/K375A) of the piggybac transposase (Li et al., 2013b; Yusa et al., 2011) (Figure 4-5). Even though the excision-only variant presented an activity of 0.85 times that of wild type, it was used in all experiments as it lacks the reintegration cycle characteristic of the wild-type variant (Li et al., 2013a). The heterozygous *SNCA* exon 2 and *SNCA* exon 3 EGFP^{pos}/dTOMATO^{pos} polyclonal populations were transfected with excision-only transposase *in vitro*-transcribed mRNA. Subsequently, the excised EGFP^{neg}/dTOMATO^{neg} population was sorted (Figure 4-5 A). Sorting analysis demonstrated average excision efficiencies of 3.65% for *SNCA* exon 2, and 2.15% for *SNCA* exon 3 (Figure 4-5 A). A second sorting step to purify cells that underwent selection module removal yielded up to 2.5×10^6 EGFP^{neg}/dTOMATO^{neg} SNP knocked-in cells. Furthermore, FACS analysis showed transition states for single-copy excision and complete removal of both selection modules (Figure 4-5 A). A curved continuous population was observed shifting from the double-positive EGFP^{pos}/dTOMATO^{pos} quadrant to the double-negative EGFP^{neg}/dTOMATO^{neg} quadrant in all cases. These observations were confirmed by fluorescence microscopy when single-copy excision and complete removal states were identified (Figure 4-5 B). Sanger sequencing of the *SNCA*-targeted and transposed genomic region demonstrated the heterozygous integration of the pathogenic SNP rs104893878 (p.A30P) and rs104893877 (p.A53T) in each polyclone (Figure 4-5 C-D). Isolation of single cell-derived clones from the polyclones and sequencing permitted quantification of their composition. This allowed an overall assessment of the specificity of the process (Figure 4-5 E). In the selected polyclones and the composition analysis, the positive selection modules

were excised, the edited SNPs remained, and the edited PAM sites remained in the non-coding sequence (Figure 4-5 C-E).

Figure 4-5

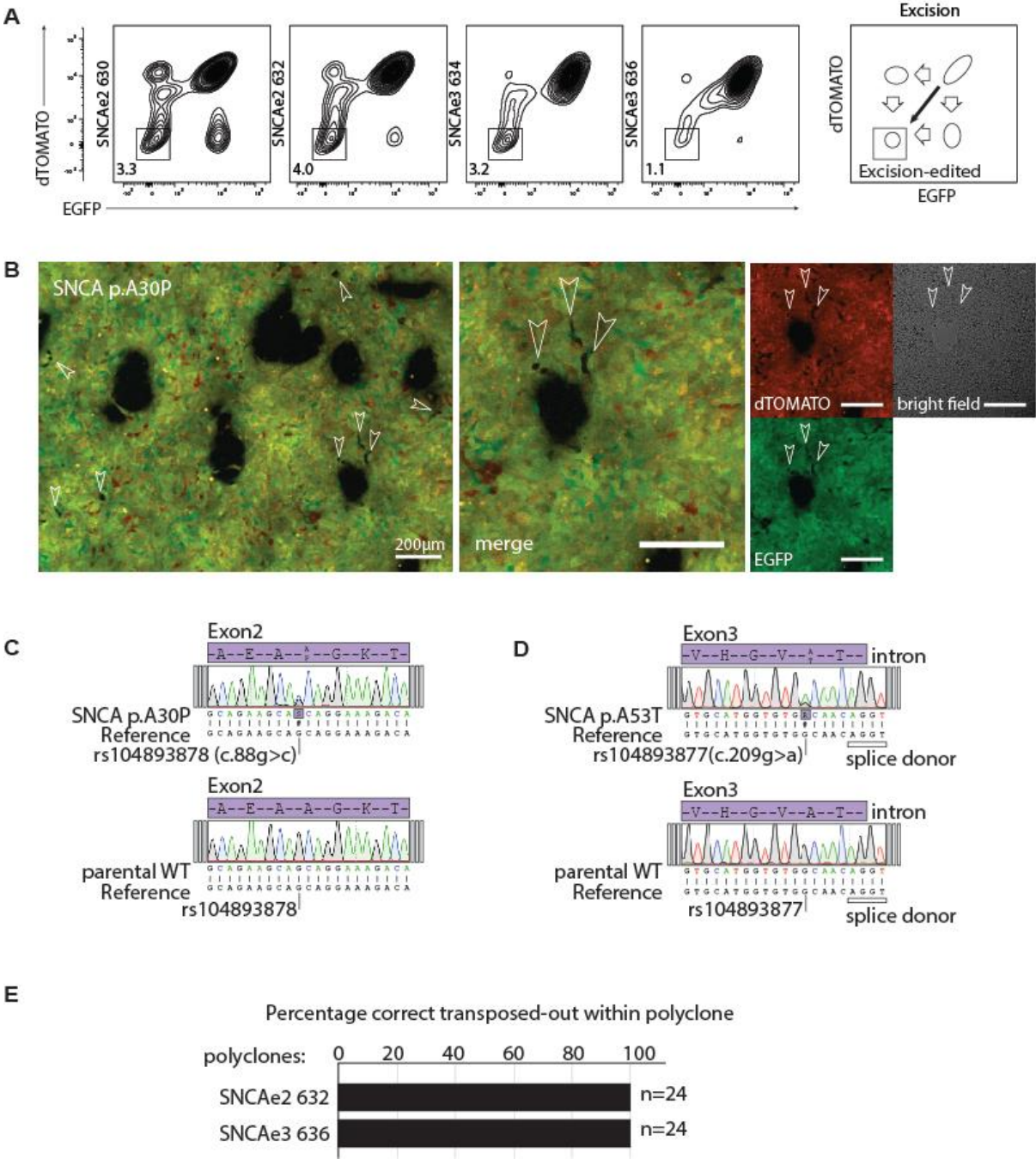


Figure 4-5. Transposase-mediated generation of footprint-free isogenic lines. **A.** FACS analysis for positive selection module removal. Two transfection steps of excision-only transposase for *SNCA* exon 2 and *SNCA* exon 3 polyclones. Purification gate of EGFP^{neg}/dTOMATO^{neg} used for edited lines is indicated. **B.** Cultures after transposase transfection for *SNCA* exon 2 present single and double-positive selection module removal events (in arrows). Merge and split channels are shown. Scale bar indicates 200µm. **C.** Sanger sequencing chromatogram of transposed *SNCA* exon 2 p.A30P polyclone 632 and parental wild-type control. **D.** Sanger sequencing chromatogram of transposed *SNCA* exon 3 p.A53T polyclone 636 and parental wild-type control. **E.** Analysis of the respective polyclones composition.

4-6 Edited polyclones preserve genome stability and pluripotency properties

Previous reports support the conclusion that isogenic lines with low incidence of genomic aberrations can be obtained after the use of genome-editing tools (Lorenz et al., 2017; Veres et al., 2014). Karyotype assessment of the edited polyclones demonstrated they lack significant alterations when compared to their parental control line (Figure 4-6 A-C). Assessment of the pluripotency state of polyclones demonstrated expression of the transcription factors OCT4 and SOX2 (Figure 4-6 D-F). TRA1-81 and SSEA4 are surface markers characteristic of human primed pluripotency state. The edited polyclones presented TRA1-81 and SSEA4 expression levels similar to their parental line (Figure 4-6 D-F). These results confirm that after the edition process cells maintained both the genomic stability and pluripotency state existent in the parental line.

Figure 4-6

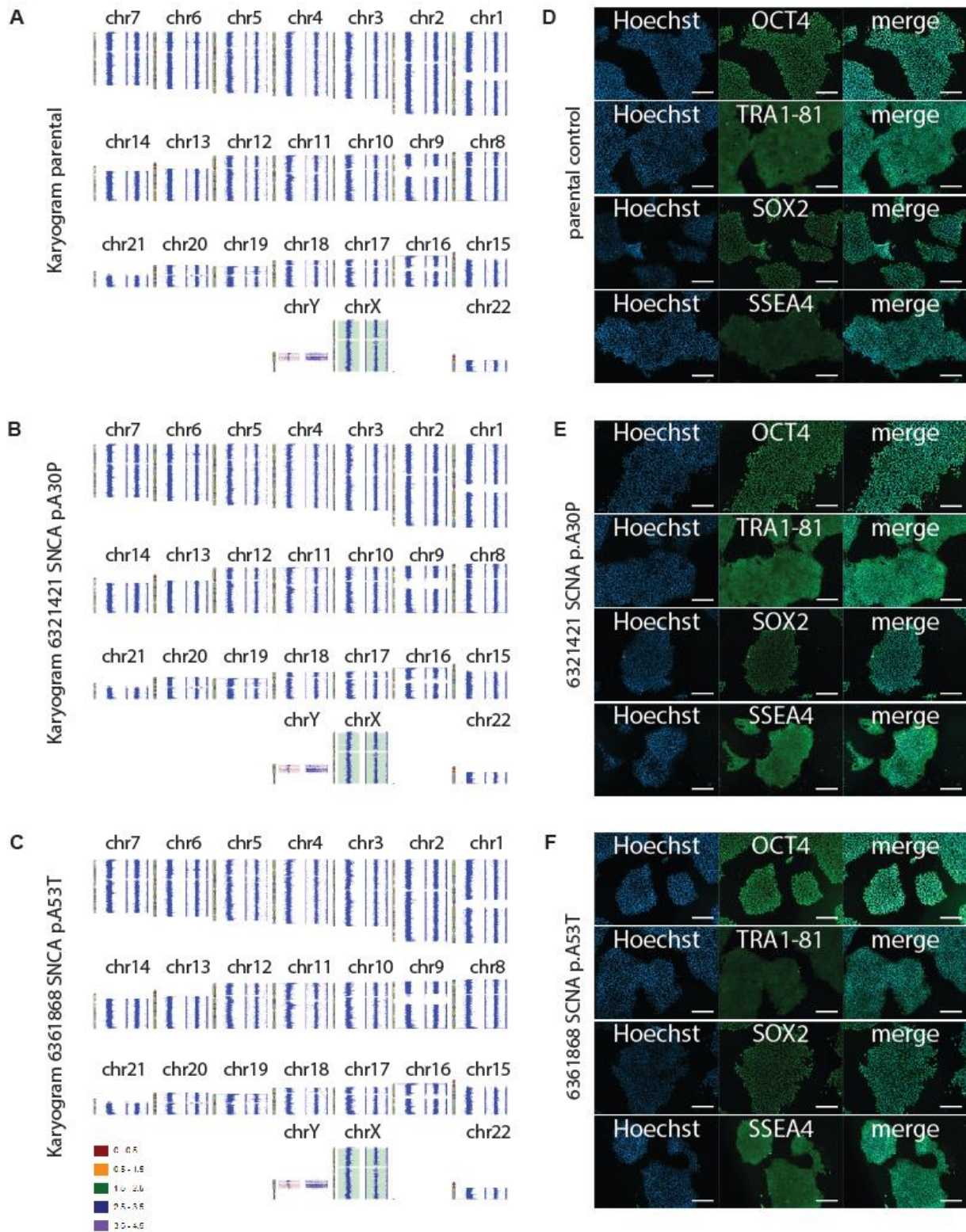


Figure 4-6. Edited polyclones preserve genome stability and pluripotency properties. **A.** Microarray karyotype analysis of the healthy control parental line before electroporation. **B.** Polyclone 6321421 SNCA p.A30P. **C.** Polyclone 6361868 SNCA p.A53T. **D.** Immunostaining for the pluripotency markers OCT4, TRA1-81, SOX2 and SSEA4 for parental control iPS cells. **E.** Polyclone 6321421 SNCA p.A30P. **F.** Polyclone 6361868 SNCA p.A53T. Scale bar indicates 200µm.

4-7 Human iPS cell derived NESC express α -Synuclein

NESCs are a versatile early neurodevelopmental model (Reinhardt et al., 2013). The isogenic iPS cells derived were differentiated into NESC with a set of small-molecules as previously described (Figure 4-7 A-B) (Reinhardt et al., 2013). Healthy control, SNCA p.A30P and SNCA p.A53T NESC expressed neuronal stem cell markers SOX2 and NESTIN (Figure 4-7 C). Microarray analysis of NESC demonstrated healthy control cells express *SNCA* transcript at 0.86 and 0.7 times the level of *GAPDH* and *TUBG1*, respectively (Figure 4-7 D-E). Western blot analysis indicated a similar protein expression level of monomeric α -Synuclein for all genotypes (Figure 4-7 F). These results demonstrate that NESC express *SNCA* at transcriptional and at protein level.

Figure 4-7

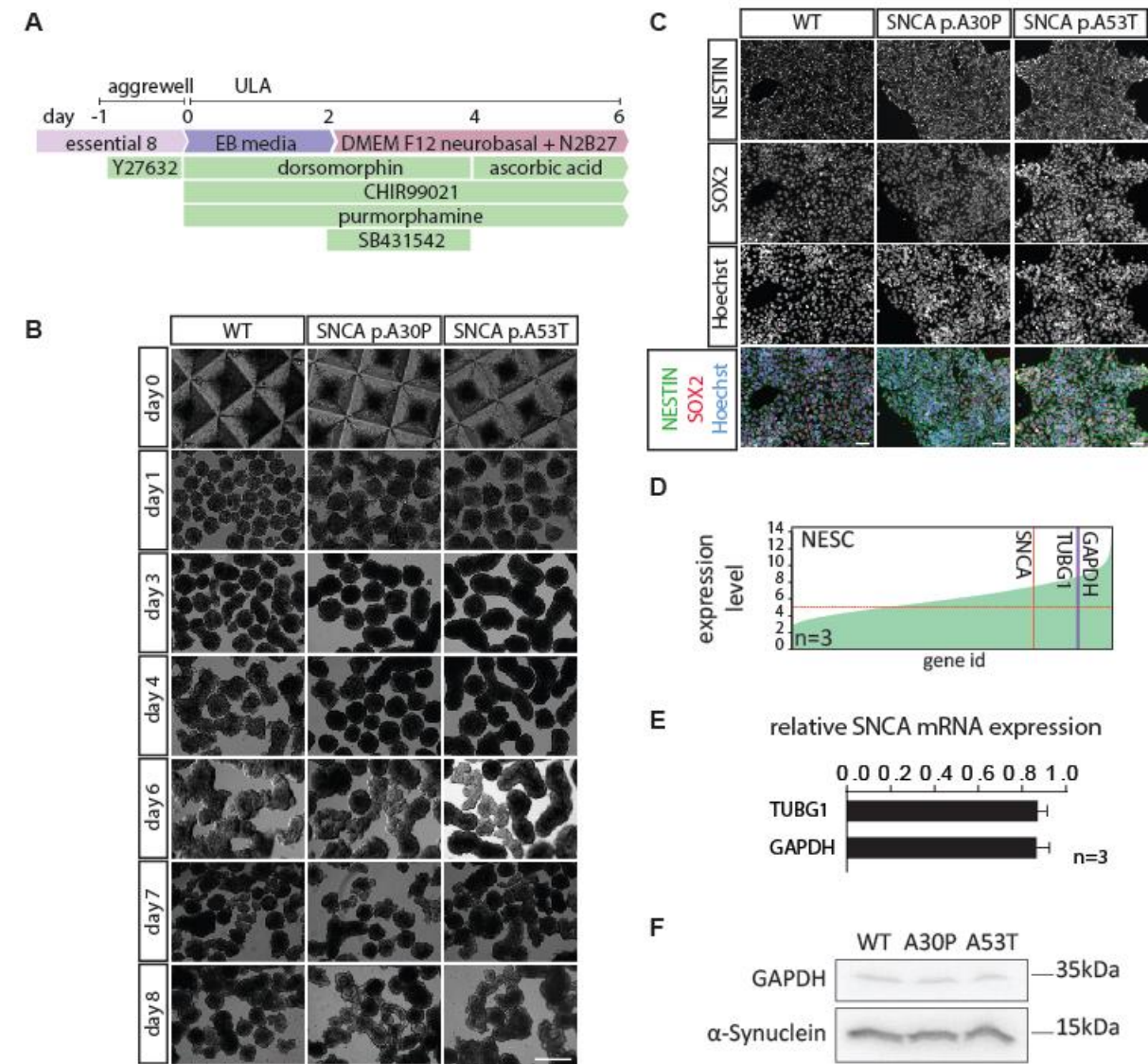


Figure 4-7. Human iPS cell derived NESCs express α -Synuclein. **A.** Overview of NESCs differentiation protocol. **B.** Differentiation of human iPS cells towards NESCs in 3D culture conditions as shown in **A**. Scale bar indicates 500 μ m. **C.** Immunostaining of NESCs for the neuroepithelial stem cell markers NESTIN and SOX2. Nuclear staining with Hoechst. Scale bar indicates 50 μ m. **D.** Microarray expression level for *SNCA*, *TUBG1*, and *GAPDH* in healthy control NESCs. **E.** Relative expression of *SNCA* mRNA with respect to *TUBG1* and *GAPDH* transcripts in the microarray expression analysis **D**. **F.** Western blot subsequent to denaturing SDS-PAGE for α -Synuclein and GAPDH, for NESCs.

4-8 SNCA mutants present reduced mitochondrial performance

Extracellular energy flux analysis is a widely accepted assay to define mitochondrial performance in neuronal models (Cooper et al., 2012; Ryan et al., 2013). Extracellular energy flux analysis was conducted for parental healthy NESC, patient-derived NESC for PINK1 p.I368N, mutant isogenic α -Synuclein p.A30P, and p.A53T NESC (Figure 4-8 A). Cells expressing the α -Synuclein mutation p.A53T showed a significantly reduced maximal respiration capacity compared to the parental isogenic control (Figure 4-8 B). Moreover, both the p.A30P and p.A53T α -Synuclein mutant NESC showed comparatively reduced energy performance. This was manifested by lower basal respiration, ATP production, and non-mitochondrial respiration (Figure 4-8 B). Fold change transformation of the absolute values with respect to the healthy control NESC allowed the visualization of the overall reduced mitochondrial performance of α -Synuclein mutants (Figure 4-8 C). Interestingly, the patient-derived PINK1 p.I368N mutant NESC presented significantly reduced mitochondrial metabolism performance for all features of extracellular energy flux analysis (Figure 4-8 B). PINK1 p.I368N corresponds to a loss of function mutant, consequently, the results observed are in agreement with reports that characterize *PINK1* knock-down disease models (Dagda et al., 2011).

Figure 4-8

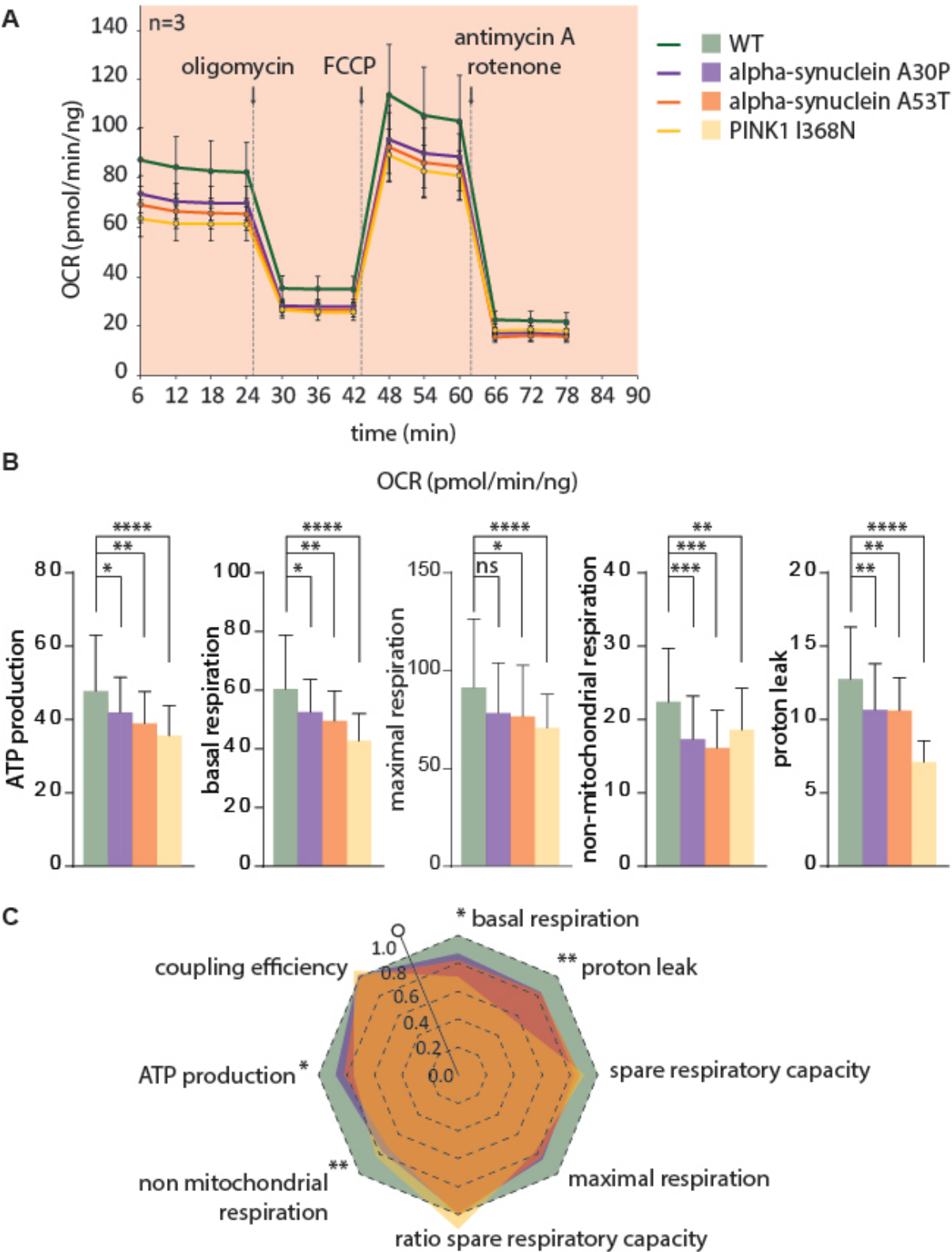


Figure 4-8. SNCA mutants present reduced mitochondrial performance. **A.** Wave plot of oxygen consumption rates for PINK1 patient and α -Synuclein isogenic set. Each wave corresponds to three biological replicates. SD of the sample is included. **B.** Maximal respiration, proton leak, basal respiration, ATP production, and non-mitochondrial respiration for the α -Synuclein isogenic set in **A.** **C.** Radar plot of fold changes for extracellular energy flux analysis performance in **A.** Significance levels correspond to the higher p-value assigned to a mutant per category. Significance determined by unpaired Student's t-test. Significance levels are * $p < 0.05$, ** $p < 0.01$ and *** $p < 0.001$

第五章

Chapter 5

結論及び考察 2

Conclusion & Discussion 2

Here, the development of genome-editing technology was leveraged to produce human PD models. Increasing demand for isogenic disease models highlights the need to develop methods that facilitate the genotyping endeavor. Overall, FACE constitutes a robust method to achieve deterministic genotype outcomes. The purification of biallelic editing events ensure a defined genotype. However, biallelic edition is restricted to non-essential genes, due to transient disruption of both coding sequences. The use of a fluorescent negative selection module to exclude random integration events achieves clearer sorting gating compared to similar approaches (Eggenschwiler et al., 2016). A potential limitation is that selection modules could be subjected to position-effect variegation. Nevertheless, usage of fluorescent markers expedite the selection, reducing the timescale in comparison to potential position-effect variegation (Norrman et al., 2010). It should be noted that editing approaches that use ssDNA or dsDNA could be subjected to cleavage within non-functional or functional sequences. The advantage of dsDNA approaches in comparison to ssDNA are its flexibility to carry larger cargos, in order to deposit designer-insertions, designer-deletions or selection modules. Conventional derivation of single-nucleotide mutations, not associated with a direct selection phenotype or selection marker, can require screening an average 911 ± 375 clones and using 8.8 ± 5.9 sgRNAs (Paquet et al., 2016). Conversely, early elimination of undesirable outcomes obviates the need to perform extensive colony screening and results in a faster, more efficient derivation process. Thus, FACE constitutes an attractive alternative to conventional methods. The efficiency of HDR is influenced by the length of the homology arms used (Hasty et al., 1991). The use of ~ 1 kbp homology arms provides a balance between efficiency and specificity (Soldner et al., 2011). The sequence conversion from endogenous genome to that carried in donor templates extend from ~ 400 bp in dsDNA donors (Elliott and Jasin, 2001; Elliott et al., 1998) and to ~ 30 bp in ssDNA donors (Paquet et al., 2016). Therefore,

it is of critical importance to include the edited bases close to the dsDNA break point and close to the positive selection module unit, independent of the length of homology arms or the type of template used. Post-knock-in and post-transposition clonal composition analysis confirmed that FACE enables the derivation of polyclones and significantly reduces the screening efforts if individual clones were preferred. On the other hand, the derivation of edited polyclones presents the advantage of avoiding the risk inherent with clone-specific biases. Extensive expansion, required for clonal derivation, is reported to subject cells to culture aberrations (Jahreiss et al., 2008; Ma et al., 2015; Martins-Taylor and Xu, 2012). It is widely accepted that single cell passaging for any type of cell culture application, including the here described process of FACS-based enrichment, imposes an unavoidable risk of genome instability (Chan et al., 2008). The derivation of polyclones reduces the culture time needed for each step, since sufficient material is available earlier. Karyotype analysis of the edited lines demonstrated that the process did not induce chromosomal abnormalities when compared with the parental line. Previous reports also support the possibility of achieving low incidence of modification with genome-editing tools (Lorenz et al., 2017; Veres et al., 2014).

In order to protect the dsDNA donor template from CRISPR-Cas9-induced linearization and to avoid post-integration cleavage of targeted sequences, silent mutations in the PAM sequences were introduced. This requires special attention to design in order to introduce the edited PAM in a non-coding sequence or as a silent mutation. This mechanistic insight was used to protect post-integration targeted sequences from secondary cleavage events (Inui et al., 2014; Paquet et al., 2016). Similarly, design considerations are needed to identify adjacent transposase excision sequences (TTAA), or to generate a *de novo* TTAA sequence in non-coding regions or by silent editions. Protocol optimization for the use of an excision-only transposase variant (Li et al., 2013b) allowed the derivation of footprint-free isogenic sets for

disease modeling. Transition states that represent the removal of one or both positive selection modules were observed. The transition populations presented a curve pattern that accounts for dissimilar stability of the fluorescent proteins (Snapp, 2009) and transcripts after the CDS module was removed.

The influence of repetitive elements on the efficiency of genome editing has been reported previously (Ishii et al., 2014). Recognizable repetitive elements constitute up to ~45% of the human genome (Lander et al., 2001). Repetitive elements in humans can be classified into four families: SINE, LINE, LTR retrotransposons and DNA transposons. Each category presents multiple sub-families. Using linear optimization modeling, it was determined that repetitive elements of SINE family, Alu and Mir, contribute the most to random integration events. These repetitive elements have 1.5 million copies and constitute ~13% of the human genome (Lander et al., 2001). Although this discrete dataset does not include all existing human repetitive elements, it demonstrates their direct contribution to random integration. Other aspects such as the composition of repetitive elements and distance to the dsDNA break point might modulate the frequency of random integration. This work confirms previous reports that repetitive elements act as templates for off-target homologous recombination (Ishii et al., 2014). These sequences should be avoided when designing homology arms in order to enhance the on-target recombination and edition.

In summary, here presents the generation of an isogenic set of human *SNCA* mutants for PD-specific cellular modeling. The set carries the *SNCA* disease-associated mutations p.A30P and p.A53T. Using the early neurodevelopment model of NESCs, energy metabolism phenotypes were observed as previously described for iPS-derived neurons with the *SNCA* p.A30P mutation (Ryan et al., 2013). Furthermore, such observations were also confirmed in the PD

patient-derived cells with the mutation PINK1 p.I368N. Previous reports demonstrate a reduced mitochondria energy performance in *PINK1* knock-down models (Dagda et al., 2011), similar to the loss of function PINK1 p.I368N mutant. This demonstrates the applicability of the described approach for the generation of disease relevant models. A future perspective is the use of FACE as an implementation for automated high-throughput genome editing, enabling fast phenotypic assessment *in vitro*.

第六章

Chapter 6

材料及び方法

Materials and Methods

6-1 Human iPS cell culture, electroporation and selection. ヒト iPS 細胞の培養、エレクトロポレーション及び選択

Human iPS cell line A13777 (Gibco cat no. A13777), from female cord blood-derived CD34^{pos} cells was used as healthy control. PD patient lines used were PINK1 p.I368N Coriell ID 40066, LRRK2 p.G2019S Coriell ID ND33879, and VPS35 p.D620N C66345. Cells were maintained in Essential-8 media (Thermo Fisher cat no. A1517001) in feeder free culture conditions on laminin 521 (BioLamina), Matrigel (BD) or Geltrex (Thermo Fisher cat no. A1413301). Cell passage and dissociation was performed with accutase (Thermo Fisher cat no. A11105-01). Cells were electroporated with a Lonza 4D-nucleofector system (Lonza V4XP-3024) according to the manufacturer's instructions. After passage or electroporation, cells were cultured with 10 μ M Y27632 ROCK inhibitor (Sigma cat no. Y0503) for 24h. Cells were subjected to positive selection with puromycin (Sigma cat no. P9620) at a concentration of 0.25 to 0.5 μ g/mL.

6-2 Polyclones composition characterization

Composition of polyclones was assessed by sub-cloning. Single cell clones were expanded and genomic DNA extracted using QuickExtract solution (Epicentre cat no. QE09050). Clones were genotyped for the left homology arm junction, right homology arm junction, and wild-type junction. PCR products of the left homology arm were used for Sanger sequencing of subclones of *SNCA* exon 3 p.A30P polyclone 632, and *SNCA* exon 3 p.A53T polyclone 636. The wild-type junction was used for Sanger sequencing of subclones of transposed *SNCA* exon 2 p.A30P polyclone 632, and transposed *SNCA* exon 3 p.A53T polyclone 636.

6-3 NESCs differentiation and culture.

Induced pluripotent stem cells were clustered on aggrewell plates (Stem cell technologies cat no. 27845) for 12 hours. Embryoid bodies were transferred to ultra-low attachment plates and subjected to differentiation. The cells were cultured on KO-DMEM (Gibco cat no. 10829018) supplemented with 20% knock-out serum replacement (Gibco cat no. A3181501), 1x non-essential amino acids (Gibco cat no. 11140035), 2mM glutamax (Gibco cat no. 35050061), 3 μ M CHIR99021 (Sigma cat no. SML1046), 1 μ M dorsomorphine (Sigma cat no. P5499) and 0.5 μ M purmorphamine (Sigma cat no. SML0868). From day three onwards, cells were cultured on DMEM-F12:neurobasal media (1:1) supplemented with 2mM glutamax, B27 minus vitamin A (Gibco cat no. 12587001) and N2 (Gibco cat no. 17502048). For day three and four, media was supplemented with 10 μ M SB431542 (Sigma cat no. S4317). From day five onwards, the culture was maintained with 3 μ M CHIR99021, 0.5 μ M purmorphamine, and 150 μ M ascorbic acid (Sigma cat no. A5960). At day six, embryoid bodies were dissociated with accutase and plated on matrigel coated plates.

6-4 Extracellular energy flux analysis

NESCs were plated on Seahorse XFe96 assay plates (Aglient) at a density of 65k cells per well and the oxygen consumption rate was quantified in a Seahorse XFe96 Analyzer. Four baseline measurements were performed before any treatment injection. Three measurements were performed after each injection as shown in **section 4-8**. Final concentrations of compounds were 1 μ M oligomycin (Sigma cat no. 75351), FCCP (Sigma cat no. C2920), antimycin A (Sigma cat no. A8674) and rotenone (Sigma cat no. R8875). DNA was quantified using CyQUANT kit

(Thermo Fisher cat no. C7026) and normalization based on DNA content as previously described (Silva et al., 2013).

6-5 Cloning of sgRNA containing vectors and donor vectors

CRISPR-Cas9 target sequences were designed to achieve high *in-silico* efficiency according to previous reports (Doench et al., 2014). Targeting sequences were cloned into pX330 vector (Addgene 42230) as previously described (Ran et al., 2013). Donor vectors used were pDONOR-SNCAe2-WT (Addgene 85845), pDONOR-SNCAe2-A30P (Addgene 85846), pDONOR-SNCAe3-WT (Addgene 85847), pDONOR-SNCAe3-A53T (Addgene 85848) and pDONOR-PINK1e5-I368N (Addgene 86154) in EGFP and dTOMATO containing versions. Homology arms were assembled by Gibson assembly according to conventional methods (Gibson, 2011). The scaffolds used for cloning were pDONOR-tagBFP-PSM-EGFP (Addgene 100603), and pDONOR-tagBFP-PSM-dTOMATO (Addgene 100604).

6-6 Autophagy and mitophagy reporter platform

The pH sensor fluorescent protein pHluorin included the CDS optimizations F64L, S65T, V193G and H231Q. Protein pHluorin CDS was fused to DsRED and the mitochondrial, or autophagosomal targeting sequence from ATP5C1 or LC3 as previously described (Sargsyan et al., 2015). The fusion CDS was introduced into the AAVS1 safe harbor locus as previously described (Hockemeyer et al., 2009) using the targeting donor (Addgene plasmid # 22075) and TALEN (Addgene plasmid #35432 and #35431).

6-7 In-vitro RNA transcription and mRNA transfection.

The CDS of codon-optimized hyperactive transposase Piggybac from *Trichoplusia ni* (Yusa et al., 2011) and the excision-only mutant (Li et al., 2013b) were amplified to incorporate the T7 promoter sequence gaaattaatacgaactcactataggg. The PCR product was used as template for *in vitro* transcription using a mMESSAGE mMACHINE T7 kit (Thermo Fisher cat no. AM1344). Subsequently, the transcript was poly-adenylated with a Poly(A) tailing kit (Thermo Fisher cat no. AM1350) and purified with a MEGAclean transcription clean-up kit (Thermo Fisher cat no. AM1908). The transcript quality was evaluated with a Bionalyzer RNA 6000 nano (Agilent cat no. 5067-1511). Finally, transfection was performed with Stemfect RNA transfection kit (Stemgent cat no. 00-0069).

6-8 Pathway contribution dissection

Reporter lines were treated with a set of compounds to dissect mitophagy and autophagy pathway steps. Basal levels for autophagy and mitophagy reporter lines were established, and then cells were treated with the compound set. Cells were imaged every thirty minutes for a period of three hours. For dissecting the contribution of autophagy and mitophagy pathways, cells were plated at a density of 600k/cm² for 8 or 12 hours and subjected to serial dilutions of the molecular modulators. Final concentration of modulators were: 8μM-31.5nM bafilomycin A1 (Enzo cat no. BML-CM110); 8μM-31.5nM CCCP (Sigma cat no. C2759); 300μM-75μM chloroquine (Sigma cat no. C6628); 160μM-675nM DFP (Sigma cat no. D0879); 20μM-675nM Oligomycin A (Sigma cat no. 75351); 160μM-675nM Rapamycin (Sigma cat no. R8781); 40μM-156nM thapsigargin (Sigma cat no. T9033); and 160μM-675nM valinomycin (Sigma cat no. V3639).

6-9 Lysosome quantification and nuclear contrast

Cells under basal conditions were treated with deep red lysotracker (Thermo cat no. L12492) at a dilution of 1:1000 for 30 minutes. Cells were stained with 20 μ M Hoechst 33342 for nuclear contrast.

6-10 FACS analysis. FACS 分析

FACS was conducted using sterile line sorting on a baseline and CST calibrated BD FACS ARIA III. Drop delay calibrations were ensured prior to each sample. For all human iPS cells an 85 μ m nozzle, a yield or purity-sorting mask and neutral density filter 2.0 were used. Cells were pre-separated with 35 μ m and 20 μ m strainers (Corning cat no. 352235 and Miltenyi cat no. 130-101-812). Sorting was conducted with single cell exclusive gating hierarchies on FSC and SSC wide and high. The use of strainers and single cell gating structures is highly recommended. For efficiency analysis, live cells were quantified by SYTOX Blue Dead Cell Stain (Thermo Fisher cat no. S34857).

6-11 Time-lapse live cell imaging. 経時的生細胞観察

Culture dynamics and time lapse imaging was evaluated in a spinning-disk CSU-X1 system (Zeiss) under controlled atmosphere. Reconstruction of 3D structures was performed with Imaris (Bitplane) image processing 7.0 system.

6-12 Microscopy for Rosella-LC3, ATP5C1-Rosella, and Lysotracker. Rosella-LC3、ATP5C1-Rosella 及び Lysotracker を用いた蛍光顕微鏡観察

Confocal images were acquired on an Opera QEHS spinning-disk microscope (Perkin Elmer) using a 60x water immersion objective (NA = 1.2). DsRED and pHluorin images were acquired in parallel using two cameras and binning 2. Channel pHluorin was excited with a 488 nm laser and channel DsRED with a 561 nm laser. A 568 dichroic mirror was used to deviate the emitted light towards the corresponding cameras. Emission for pHluorin was detected with a 520/35 bandpass filter, and emission for DsRED with a 600/40 bandpass filter. Lysotracker deep red was acquired independently, excited with a 640 nm laser, and detected with a 690/70 bandpass filter using camera binning 2. Five planes were set with 400nm z-steps for Rosella-LC3. Eleven planes were set with 400nm z-steps for ATP5C1-Rosella. Eleven planes were set with 400nm z-steps for lysotracker. Scale of 1 pixel corresponds to 0.2152µm in all the cases described.

6-13 Image analysis for Rosella-LC3 autophagy, ATP5C1-Rosella mitophagy assay and Lysotracker assay

An automated computational image analysis workflow for the resulting multichannel 3D images was implemented in Matlab (R2017a, Mathworks). Detailed description of the algorithm is provided in **section 2-5**, **section 2-6** and **section 2-7**.

6-14 mRNA Microarray

RNA was extracted from healthy control NESCes using quiazol (Qiagen cat no. 79306) and miRNeasy (Qiagen cat no. 217004). Samples were processed at the EMBL Genomics Core Facility using Affymetrix human Gene 2.0 arrays. Results were processed using GC-RMA analysis. Gene expression omnibus accession code is GSE101534.

6-15 Microarray Karyotype. Karyotype 核型分析

Genomic DNA samples from the pre-electroporation parental, and isogenic polyclones were purified using GenElute Blood genomic DNA Kit (Sigma cat no. NA2020). Samples were processed at Bonn Univesity Life&Brain genomics facility using Illumina iScan technology (Illumina).

6-16 Immunostaining. 免疫染色

Cells were fixed on PFA and permeabilized on PBS triton-X 0.2% for 10 minutes. For characterizing human iPS cells, primary antibodies used were SOX2 (Abcam cat no. ab97959) dilution 1:100, OCT4 (Santa cruz cat no. sc-5279) dilution 1:100, SSEA4 (Millipore cat no. MAB4304) dilution 1:50 and TRA1-81 (Millipore cat no. MAB4381) dilution 1:50. Secondary antibodies used were donkey anti-mouse alexa fluor 488 (Thermo Fisher cat no. A-21202) and donkey anti-rabbit alexa fluor 488 (Thermo Fisher cat no. A-21206), both at dilution 1:1000. For characterizing NESCes, primary antibodies used were NESTIN (BD cat no. 611659) dilution 1:600 and SOX2 (Abcam cat no. ab97959) dilution 1:200. Secondary antibodies used were donkey anti-mouse 488 (Thermo Fisher cat no. A-21202) and donkey anti-rabbit 647 (Thermo

Fisher cat no. A-31573), both at dilution 1:1000. For nuclear staining, Hoechst-33342 (Thermo Fisher cat no. 62249) was used at dilution 1:1000. Images were acquired in an inverted microscope (Zeiss Axio ObserverZ1).

6-17 Western Blotting. ウェスタン・ブロッティング

For western blot analysis of NESCs total protein, an antibody against α -Synuclein (C-20)-R (Santa cruz cat no. sc-7011) was used at a dilution of 1:100, and an antibody against GAPDH (abcam cat no. ab9485) was used at a dilution of 1:1000 overnight. Blots were developed using anti-rabbit IgG HRP-linked secondary antibody (GE Healthcare Life Sciences cat no. NA934V) and west-pico chemiluminescent substrate (Thermo Fisher cat no. 34080). Membranes were imaged in a Raytest Stells system with exposure of 30s for both α -Synuclein and GAPDH.

文献

Bibliography

1. Abreu, S., Kriegenburg, F., Gomez-Sanchez, R., Mari, M., Sanchez-Wandelmer, J., Skytte Rasmussen, M., Soares Guimaraes, R., Zens, B., Schuschnig, M., Hardenberg, R., *et al.* (2017). Conserved Atg8 recognition sites mediate Atg4 association with autophagosomal membranes and Atg8 deconjugation. *EMBO Rep* 18, 765-780.
2. Allen, G.F., Toth, R., James, J., and Ganley, I.G. (2013). Loss of iron triggers PINK1/Parkin-independent mitophagy. *EMBO Rep* 14, 1127-1135.
3. Ando, M., Fiesel, F.C., Hudec, R., Caulfield, T.R., Ogaki, K., Gorka-Skoczylas, P., Kozirowski, D., Friedman, A., Chen, L., Dawson, V.L., *et al.* (2017). The PINK1 p.I368N mutation affects protein stability and ubiquitin kinase activity. *Mol Neurodegener* 12, 32.
4. Aoki, K., Kiyokawa, E., Nakamura, T., and Matsuda, M. (2008). Visualization of growth signal transduction cascades in living cells with genetically encoded probes based on Forster resonance energy transfer. *Philos Trans R Soc Lond B Biol Sci* 363, 2143-2151.
5. Barker, R.A., Drouin-Ouellet, J., and Parmar, M. (2015). Cell-based therapies for Parkinson disease-past insights and future potential. *Nat Rev Neurol* 11, 492-503.
6. Bartels, T., Choi, J.G., and Selkoe, D.J. (2011). alpha-Synuclein occurs physiologically as a helically folded tetramer that resists aggregation. *Nature* 477, 107-110.
7. Bendor, J.T., Logan, T.P., and Edwards, R.H. (2013). The function of alpha-synuclein. *Neuron* 79, 1044-1066.
8. Berger, Z., Smith, K.A., and Lavoie, M.J. (2010). Membrane localization of LRRK2 is associated with increased formation of the highly active LRRK2 dimer and changes in its phosphorylation. *Biochemistry* 49, 5511-5523.
9. Bertolin, G., Jacoupy, M., Traver, S., Ferrando-Miguel, R., Saint Georges, T., Grenier, K., Ardila-Osorio, H., Muriel, M.P., Takahashi, H., Lees, A.J., *et al.* (2015). Parkin maintains mitochondrial levels of the protective Parkinson's disease-related enzyme 17-beta hydroxysteroid dehydrogenase type 10. *Cell Death Differ* 22, 1563-1576.
10. Bibel, M., Richter, J., Lacroix, E., and Barde, Y.A. (2007). Generation of a defined and uniform population of CNS progenitors and neurons from mouse embryonic stem cells. *Nat Protoc* 2, 1034-1043.
11. Bindels, D.S., Haarbosch, L., van Weeren, L., Postma, M., Wiese, K.E., Mastop, M., Aumonier, S., Gotthard, G., Royant, A., Hink, M.A., *et al.* (2017). mScarlet: a bright monomeric red fluorescent protein for cellular imaging. *Nat Methods* 14, 53-56.
12. Bozi, M., Papadimitriou, D., Antonellou, R., Moraitou, M., Maniati, M., Vassilatis, D.K., Papageorgiou, S.G., Leonardos, A., Tagaris, G., Malamis, G., *et al.* (2014). Genetic assessment of familial and early-onset Parkinson's disease in a Greek population. *Eur J Neurol* 21, 963-968.
13. Burdon, T., Stracey, C., Chambers, I., Nichols, J., and Smith, A. (1999). Suppression of SHP-2 and ERK signalling promotes self-renewal of mouse embryonic stem cells. *Dev Biol* 210, 30-43.
14. Cai, D., Cohen, K.B., Luo, T., Lichtman, J.W., and Sanes, J.R. (2013). Improved tools for the Brainbow toolbox. *Nat Methods* 10, 540-547.
15. Carvalho, M.C. (2013). Integration of analytical instruments with computer scripting. *J Lab Autom* 18, 328-333.
16. Chambers, S.M., Fasano, C.A., Papapetrou, E.P., Tomishima, M., Sadelain, M., and Studer, L. (2009). Highly efficient neural conversion of human ES and iPS cells by dual inhibition of SMAD signaling. *Nat Biotechnol* 27, 275-280.
17. Chambers, S.M., Qi, Y., Mica, Y., Lee, G., Zhang, X.J., Niu, L., Bilsland, J., Cao, L., Stevens, E., Whiting, P., *et al.* (2012). Combined small-molecule inhibition accelerates developmental

timing and converts human pluripotent stem cells into nociceptors. *Nat Biotechnol* 30, 715-720.

18. Chan, E.M., Yates, F., Boyer, L.F., Schlaeger, T.M., and Daley, G.Q. (2008). Enhanced plating efficiency of trypsin-adapted human embryonic stem cells is reversible and independent of trisomy 12/17. *Cloning Stem Cells* 10, 107-118.

19. Check Hayden, E. (2014). The automated lab. *Nature* 516, 131-132.

20. Chen, J.K., Taipale, J., Young, K.E., Maiti, T., and Beachy, P.A. (2002). Small molecule modulation of Smoothed activity. *Proc Natl Acad Sci U S A* 99, 14071-14076.

21. Chen, Y., and Dorn, G.W., 2nd (2013). PINK1-phosphorylated mitofusin 2 is a Parkin receptor for culling damaged mitochondria. *Science* 340, 471-475.

22. Chu, V.T., Weber, T., Wefers, B., Wurst, W., Sander, S., Rajewsky, K., and Kuhn, R. (2015). Increasing the efficiency of homology-directed repair for CRISPR-Cas9-induced precise gene editing in mammalian cells. *Nat Biotechnol* 33, 543-548.

23. Conti, L., and Cattaneo, E. (2010). Neural stem cell systems: physiological players or in vitro entities? *Nat Rev Neurosci* 11, 176-187.

24. Cookson, M.R. (2010). The role of leucine-rich repeat kinase 2 (LRRK2) in Parkinson's disease. *Nat Rev Neurosci* 11, 791-797.

25. Cookson, M.R. (2015). LRRK2 Pathways Leading to Neurodegeneration. *Curr Neurol Neurosci Rep* 15, 42.

26. Cooper, O., Seo, H., Andrabi, S., Guardia-Laguarta, C., Graziotto, J., Sundberg, M., McLean, J.R., Carrillo-Reid, L., Xie, Z., Osborn, T., *et al.* (2012). Pharmacological rescue of mitochondrial deficits in iPSC-derived neural cells from patients with familial Parkinson's disease. *Sci Transl Med* 4, 141ra190.

27. Dagda, R.K., Gusdon, A.M., Pien, I., Strack, S., Green, S., Li, C., Van Houten, B., Cherra, S.J., 3rd, and Chu, C.T. (2011). Mitochondrially localized PKA reverses mitochondrial pathology and dysfunction in a cellular model of Parkinson's disease. *Cell Death Differ* 18, 1914-1923.

28. de Vries, R.L., and Przedborski, S. (2013). Mitophagy and Parkinson's disease: be eaten to stay healthy. *Mol Cell Neurosci* 55, 37-43.

29. Dettmer, U., Newman, A.J., Soldner, F., Luth, E.S., Kim, N.C., von Saucken, V.E., Sanderson, J.B., Jaenisch, R., Bartels, T., and Selkoe, D. (2015a). Parkinson-causing alpha-synuclein missense mutations shift native tetramers to monomers as a mechanism for disease initiation. *Nat Commun* 6, 7314.

30. Dettmer, U., Newman, A.J., von Saucken, V.E., Bartels, T., and Selkoe, D. (2015b). KTEGV repeat motifs are key mediators of normal alpha-synuclein tetramerization: Their mutation causes excess monomers and neurotoxicity. *Proc Natl Acad Sci U S A* 112, 9596-9601.

31. Devine, M.J., Ryten, M., Vodicka, P., Thomson, A.J., Burdon, T., Houlden, H., Cavaleri, F., Nagano, M., Drummond, N.J., Taanman, J.W., *et al.* (2011). Parkinson's disease induced pluripotent stem cells with triplication of the alpha-synuclein locus. *Nat Commun* 2, 440.

32. Di Fonzo, A., Dekker, M.C., Montagna, P., Baruzzi, A., Yonova, E.H., Correia Guedes, L., Szczerbinska, A., Zhao, T., Dubbel-Hulsman, L.O., Wouters, C.H., *et al.* (2009). FBXO7 mutations cause autosomal recessive, early-onset parkinsonian-pyramidal syndrome. *Neurology* 72, 240-245.

33. Ding, Q., Lee, Y.K., Schaefer, E.A., Peters, D.T., Veres, A., Kim, K., Kuperwasser, N., Motola, D.L., Meissner, T.B., Hendriks, W.T., *et al.* (2013). A TALEN genome-editing system for generating human stem cell-based disease models. *Cell Stem Cell* 12, 238-251.

34. Do, C.B., Tung, J.Y., Dorfman, E., Kiefer, A.K., Drabant, E.M., Francke, U., Mountain, J.L., Goldman, S.M., Tanner, C.M., Langston, J.W., *et al.* (2011). Web-based genome-wide

association study identifies two novel loci and a substantial genetic component for Parkinson's disease. *PLoS Genet* 7, e1002141.

35. Doench, J.G., Hartenian, E., Graham, D.B., Tothova, Z., Hegde, M., Smith, I., Sullender, M., Ebert, B.L., Xavier, R.J., and Root, D.E. (2014). Rational design of highly active sgRNAs for CRISPR-Cas9-mediated gene inactivation. *Nat Biotechnol* 32, 1262-1267.

36. Edwards, T.L., Scott, W.K., Almonte, C., Burt, A., Powell, E.H., Beecham, G.W., Wang, L., Zuchner, S., Konidari, I., Wang, G., *et al.* (2010). Genome-wide association study confirms SNPs in SNCA and the MAPT region as common risk factors for Parkinson disease. *Ann Hum Genet* 74, 97-109.

37. Eggenschwiler, R., Moslem, M., Fraguas, M.S., Galla, M., Papp, O., Naujock, M., Fonfara, I., Gensch, I., Wahner, A., Beh-Pajoo, A., *et al.* (2016). Improved bi-allelic modification of a transcriptionally silent locus in patient-derived iPSC by Cas9 nickase. *Sci Rep* 6, 38198.

38. Elkabetz, Y., Panagiotakos, G., Al Shamy, G., Socci, N.D., Tabar, V., and Studer, L. (2008). Human ES cell-derived neural rosettes reveal a functionally distinct early neural stem cell stage. *Genes Dev* 22, 152-165.

39. Elliott, B., and Jasin, M. (2001). Repair of double-strand breaks by homologous recombination in mismatch repair-defective mammalian cells. *Mol Cell Biol* 21, 2671-2682.

40. Elliott, B., Richardson, C., Winderbaum, J., Nickoloff, J.A., and Jasin, M. (1998). Gene conversion tracts from double-strand break repair in mammalian cells. *Mol Cell Biol* 18, 93-101.

41. Evans, M., and Kaufman, M. (1981). Establishment in culture of pluripotential cells from mouse embryos. *Nature* 292, 154 - 156.

42. Frommer, W.B., Davidson, M.W., and Campbell, R.E. (2009). Genetically encoded biosensors based on engineered fluorescent proteins. *Chem Soc Rev* 38, 2833-2841.

43. Funayama, M., Hasegawa, K., Kowa, H., Saito, M., Tsuji, S., and Obata, F. (2002). A new locus for Parkinson's disease (PARK8) maps to chromosome 12p11.2-q13.1. *Ann Neurol* 51, 296-301.

44. Gafni, O., Weinberger, L., Mansour, A.A., Manor, Y.S., Chomsky, E., Ben-Yosef, D., Kalma, Y., Viukov, S., Maza, I., Zviran, A., *et al.* (2013). Derivation of novel human ground state naive pluripotent stem cells. *Nature* 504, 282-286.

45. Galluzzi, L., Bravo-San Pedro, J.M., Levine, B., Green, D.R., and Kroemer, G. (2017). Pharmacological modulation of autophagy: therapeutic potential and persisting obstacles. *Nat Rev Drug Discov* 16, 487-511.

46. Gehrke, S., Wu, Z., Klinkenberg, M., Sun, Y., Auburger, G., Guo, S., and Lu, B. (2015). PINK1 and Parkin control localized translation of respiratory chain component mRNAs on mitochondria outer membrane. *Cell Metab* 21, 95-108.

47. Genomes Project, C., Abecasis, G.R., Altshuler, D., Auton, A., Brooks, L.D., Durbin, R.M., Gibbs, R.A., Hurles, M.E., and McVean, G.A. (2010). A map of human genome variation from population-scale sequencing. *Nature* 467, 1061-1073.

48. Georgakopoulos, N.D., Wells, G., and Campanella, M. (2017). The pharmacological regulation of cellular mitophagy. *Nat Chem Biol* 13, 136-146.

49. Gibson, D.G. (2011). Enzymatic assembly of overlapping DNA fragments. *Methods Enzymol* 498, 349-361.

50. Goedert, M., Spillantini, M.G., Del Tredici, K., and Braak, H. (2013). 100 years of Lewy pathology. *Nat Rev Neurol* 9, 13-24.

51. Graeber, M.B., and Muller, U. (1992). The X-linked dystonia-parkinsonism syndrome (XDP): clinical and molecular genetic analysis. *Brain Pathol* 2, 287-295.

52. Greggio, E., Zambrano, I., Kaganovich, A., Beilina, A., Taymans, J.M., Daniels, V., Lewis, P., Jain, S., Ding, J., Syed, A., *et al.* (2008). The Parkinson disease-associated leucine-rich repeat kinase 2 (LRRK2) is a dimer that undergoes intramolecular autophosphorylation. *J Biol Chem* 283, 16906-16914.
53. Hamza, T.H., Zabetian, C.P., Tenesa, A., Laederach, A., Montimurro, J., Yearout, D., Kay, D.M., Doheny, K.F., Paschall, J., Pugh, E., *et al.* (2010). Common genetic variation in the HLA region is associated with late-onset sporadic Parkinson's disease. *Nat Genet* 42, 781-785.
54. Hasty, P., Rivera-Perez, J., and Bradley, A. (1991). The length of homology required for gene targeting in embryonic stem cells. *Mol Cell Biol* 11, 5586-5591.
55. Hatta, K., Tsujii, H., and Omura, T. (2006). Cell tracking using a photoconvertible fluorescent protein. *Nat Protoc* 1, 960-967.
56. Hernandez, D.G., Nalls, M.A., Ylikotila, P., Keller, M., Hardy, J.A., Majamaa, K., and Singleton, A.B. (2012). Genome wide assessment of young onset Parkinson's disease from Finland. *PLoS One* 7, e41859.
57. Hockemeyer, D., Soldner, F., Beard, C., Gao, Q., Mitalipova, M., DeKelver, R.C., Katibah, G.E., Amora, R., Boydston, E.A., Zeitler, B., *et al.* (2009). Efficient targeting of expressed and silent genes in human ESCs and iPSCs using zinc-finger nucleases. *Nat Biotechnol* 27, 851-857.
58. Hogervorst, F.B., Cornelis, R.S., Bout, M., van Vliet, M., Oosterwijk, J.C., Olmer, R., Bakker, B., Klijn, J.G., Vasen, H.F., Meijers-Heijboer, H., *et al.* (1995). Rapid detection of BRCA1 mutations by the protein truncation test. *Nat Genet* 10, 208-212.
59. Hoyer-Hansen, M., Bastholm, L., Szyniarowski, P., Campanella, M., Szabadkai, G., Farkas, T., Bianchi, K., Fehrenbacher, N., Elling, F., Rizzuto, R., *et al.* (2007). Control of macroautophagy by calcium, calmodulin-dependent kinase kinase-beta, and Bcl-2. *Mol Cell* 25, 193-205.
60. International Parkinson Disease Genomics, C., Nalls, M.A., Plagnol, V., Hernandez, D.G., Sharma, M., Sheerin, U.M., Saad, M., Simon-Sanchez, J., Schulte, C., Lesage, S., *et al.* (2011). Imputation of sequence variants for identification of genetic risks for Parkinson's disease: a meta-analysis of genome-wide association studies. *Lancet* 377, 641-649.
61. Inui, M., Miyado, M., Igarashi, M., Tamano, M., Kubo, A., Yamashita, S., Asahara, H., Fukami, M., and Takada, S. (2014). Rapid generation of mouse models with defined point mutations by the CRISPR/Cas9 system. *Sci Rep* 4, 5396.
62. Ishihara-Paul, L., Hulihan, M.M., Kachergus, J., Upmanyu, R., Warren, L., Amouri, R., Elango, R., Prinjha, R.K., Soto, A., Kefi, M., *et al.* (2008). PINK1 mutations and parkinsonism. *Neurology* 71, 896-902.
63. Ishii, A., Kurosawa, A., Saito, S., and Adachi, N. (2014). Analysis of the role of homology arms in gene-targeting vectors in human cells. *PLoS One* 9, e108236.
64. Jahreiss, L., Menzies, F.M., and Rubinsztein, D.C. (2008). The itinerary of autophagosomes: from peripheral formation to kiss-and-run fusion with lysosomes. *Traffic* 9, 574-587.
65. Jiang, P., and Mizushima, N. (2014). Autophagy and human diseases. *Cell Res* 24, 69-79.
66. Jin, S.M., and Youle, R.J. (2012). PINK1- and Parkin-mediated mitophagy at a glance. *J Cell Sci* 125, 795-799.
67. Jonckheere, A.I., Smeitink, J.A., and Rodenburg, R.J. (2012). Mitochondrial ATP synthase: architecture, function and pathology. *J Inherit Metab Dis* 35, 211-225.
68. Kalinderi, K., Bostantjopoulou, S., and Fidani, L. (2016). The genetic background of Parkinson's disease: current progress and future prospects. *Acta Neurol Scand* 134, 314-326.
69. Karanios, E., Walker, S.A., Okkenhaug, H., Manifava, M., Hummel, E., Zimmermann, H., Ahmed, Q., Domart, M.C., Collinson, L., and Ktistakis, N.T. (2016). Autophagy initiation by ULK

complex assembly on ER tubulovesicular regions marked by ATG9 vesicles. *Nat Commun* 7, 12420.

70. Kenworthy, A.K. (2001). Imaging protein-protein interactions using fluorescence resonance energy transfer microscopy. *Methods* 24, 289-296.

71. Khurana, E., Fu, Y., Chakravarty, D., Demichelis, F., Rubin, M.A., and Gerstein, M. (2016). Role of non-coding sequence variants in cancer. *Nat Rev Genet* 17, 93-108.

72. Kim, D.S., Lee, J.S., Leem, J.W., Huh, Y.J., Kim, J.Y., Kim, H.S., Park, I.H., Daley, G.Q., Hwang, D.Y., and Kim, D.W. (2010). Robust enhancement of neural differentiation from human ES and iPS cells regardless of their innate difference in differentiation propensity. *Stem Cell Rev* 6, 270-281.

73. Kim, I., Rodriguez-Enriquez, S., and Lemasters, J.J. (2007). Selective degradation of mitochondria by mitophagy. *Arch Biochem Biophys* 462, 245-253.

74. Kim, J., Kundu, M., Viollet, B., and Guan, K.L. (2011). AMPK and mTOR regulate autophagy through direct phosphorylation of Ulk1. *Nat Cell Biol* 13, 132-141.

75. Kitada, T., Asakawa, S., Hattori, N., Matsumine, H., Yamamura, Y., Minoshima, S., Yokochi, M., Mizuno, Y., and Shimizu, N. (1998). Mutations in the parkin gene cause autosomal recessive juvenile parkinsonism. *Nature* 392, 605-608.

76. Klionsky, D.J., Abdelmohsen, K., Abe, A., Abedin, M.J., Abeliovich, H., Acevedo Arozena, A., Adachi, H., Adams, C.M., Adams, P.D., Adeli, K., *et al.* (2016). Guidelines for the use and interpretation of assays for monitoring autophagy (3rd edition). *Autophagy* 12, 1-222.

77. Koyano, F., Okatsu, K., Kosako, H., Tamura, Y., Go, E., Kimura, M., Kimura, Y., Tsuchiya, H., Yoshihara, H., Hirokawa, T., *et al.* (2014). Ubiquitin is phosphorylated by PINK1 to activate parkin. *Nature* 510, 162-166.

78. Kriks, S., Shim, J.W., Piao, J., Ganat, Y.M., Wakeman, D.R., Xie, Z., Carrillo-Reid, L., Auyeung, G., Antonacci, C., Buch, A., *et al.* (2011). Dopamine neurons derived from human ES cells efficiently engraft in animal models of Parkinson's disease. *Nature* 480, 547-551.

79. Kruger, R., Kuhn, W., Muller, T., Woitalla, D., Graeber, M., Kosel, S., Przuntek, H., Epplen, J.T., Schols, L., and Riess, O. (1998). Ala30Pro mutation in the gene encoding alpha-synuclein in Parkinson's disease. *Nat Genet* 18, 106-108.

80. Kundu, M., Lindsten, T., Yang, C.Y., Wu, J., Zhao, F., Zhang, J., Selak, M.A., Ney, P.A., and Thompson, C.B. (2008). Ulk1 plays a critical role in the autophagic clearance of mitochondria and ribosomes during reticulocyte maturation. *Blood* 112, 1493-1502.

81. Kurian, M.A., Zhen, J., Cheng, S.Y., Li, Y., Mordekar, S.R., Jardine, P., Morgan, N.V., Meyer, E., Tee, L., Pasha, S., *et al.* (2009). Homozygous loss-of-function mutations in the gene encoding the dopamine transporter are associated with infantile parkinsonism-dystonia. *J Clin Invest* 119, 1595-1603.

82. Lander, E.S., Linton, L.M., Birren, B., Nusbaum, C., Zody, M.C., Baldwin, J., Devon, K., Dewar, K., Doyle, M., FitzHugh, W., *et al.* (2001). Initial sequencing and analysis of the human genome. *Nature* 409, 860-921.

83. Lautenschlager, J., Kaminski, C.F., and Kaminski Schierle, G.S. (2017). alpha-Synuclein - Regulator of Exocytosis, Endocytosis, or Both? *Trends Cell Biol.*

84. Lee, L.V., Kupke, K.G., Caballar-Gonzaga, F., Hebron-Ortiz, M., and Muller, U. (1991). The phenotype of the X-linked dystonia-parkinsonism syndrome. An assessment of 42 cases in the Philippines. *Medicine (Baltimore)* 70, 179-187.

85. Lei, Y., Guo, X., Liu, Y., Cao, Y., Deng, Y., Chen, X., Cheng, C.H., Dawid, I.B., Chen, Y., and Zhao, H. (2012). Efficient targeted gene disruption in *Xenopus* embryos using engineered

transcription activator-like effector nucleases (TALENs). *Proc Natl Acad Sci U S A* 109, 17484-17489.

86. Lesage, S., Anheim, M., Letournel, F., Bousset, L., Honore, A., Rozas, N., Pieri, L., Madiona, K., Durr, A., Melki, R., *et al.* (2013). G51D alpha-synuclein mutation causes a novel parkinsonian-pyramidal syndrome. *Ann Neurol* 73, 459-471.

87. Lesage, S., Condroyer, C., Klebe, S., Honore, A., Tison, F., Brefel-Courbon, C., Durr, A., Brice, A., and French Parkinson's Disease Genetics Study, G. (2012). Identification of VPS35 mutations replicated in French families with Parkinson disease. *Neurology* 78, 1449-1450.

88. Levine, B., and Kroemer, G. (2008). Autophagy in the pathogenesis of disease. *Cell* 132, 27-42.

89. Li, M.A., Pettitt, S.J., Eckert, S., Ning, Z., Rice, S., Cadinanos, J., Yusa, K., Conte, N., and Bradley, A. (2013a). The piggyBac transposon displays local and distant reintegration preferences and can cause mutations at noncanonical integration sites. *Mol Cell Biol* 33, 1317-1330.

90. Li, W., Sun, W., Zhang, Y., Wei, W., Ambasudhan, R., Xia, P., Talantova, M., Lin, T., Kim, J., Wang, X., *et al.* (2011). Rapid induction and long-term self-renewal of primitive neural precursors from human embryonic stem cells by small molecule inhibitors. *Proc Natl Acad Sci U S A* 108, 8299-8304.

91. Li, X., Burnight, E.R., Cooney, A.L., Malani, N., Brady, T., Sander, J.D., Staber, J., Wheelan, S.J., Joung, J.K., McCray, P.B., Jr., *et al.* (2013b). piggyBac transposase tools for genome engineering. *Proc Natl Acad Sci U S A* 110, E2279-2287.

92. Lill, C.M., Roehr, J.T., McQueen, M.B., Kavvoura, F.K., Bagade, S., Schjeide, B.M., Schjeide, L.M., Meissner, E., Zauft, U., Allen, N.C., *et al.* (2012). Comprehensive research synopsis and systematic meta-analyses in Parkinson's disease genetics: The PDGene database. *PLoS Genet* 8, e1002548.

93. Linshiz, G., Stawski, N., Poust, S., Bi, C., Keasling, J.D., and Hillson, N.J. (2013). PaR-PaR laboratory automation platform. *ACS Synth Biol* 2, 216-222.

94. Liou, C.W., Chuang, J.H., Chen, J.B., Tiao, M.M., Wang, P.W., Huang, S.T., Huang, T.L., Lee, W.C., Weng, S.W., Huang, P.H., *et al.* (2016). Mitochondrial DNA variants as genetic risk factors for Parkinson disease. *Eur J Neurol* 23, 1289-1300.

95. Livet, J., Weissman, T.A., Kang, H., Draft, R.W., Lu, J., Bennis, R.A., Sanes, J.R., and Lichtman, J.W. (2007). Transgenic strategies for combinatorial expression of fluorescent proteins in the nervous system. *Nature* 450, 56-62.

96. Lorenz, C., Lesimple, P., Bukowiecki, R., Zink, A., Inak, G., Mlody, B., Singh, M., Semtner, M., Mah, N., Aure, K., *et al.* (2017). Human iPSC-Derived Neural Progenitors Are an Effective Drug Discovery Model for Neurological mtDNA Disorders. *Cell Stem Cell*.

97. Lotharius, J., and Brundin, P. (2002). Pathogenesis of Parkinson's disease: dopamine, vesicles and alpha-synuclein. *Nat Rev Neurosci* 3, 932-942.

98. Luth, E.S., Bartels, T., Dettmer, U., Kim, N.C., and Selkoe, D.J. (2015). Purification of alpha-synuclein from human brain reveals an instability of endogenous multimers as the protein approaches purity. *Biochemistry* 54, 279-292.

99. Ma, H., Folmes, C.D., Wu, J., Morey, R., Mora-Castilla, S., Ocampo, A., Ma, L., Poulton, J., Wang, X., Ahmed, R., *et al.* (2015). Metabolic rescue in pluripotent cells from patients with mtDNA disease. *Nature* 524, 234-238.

100. Mali, P., Yang, L., Esvelt, K.M., Aach, J., Guell, M., DiCarlo, J.E., Norville, J.E., and Church, G.M. (2013). RNA-guided human genome engineering via Cas9. *Science* 339, 823-826.

- 101.** Martin, G.R. (1981). Isolation of a pluripotent cell line from early mouse embryos cultured in medium conditioned by teratocarcinoma stem cells. *Proc Natl Acad Sci U S A* **78**, 7634-7638.
- 102.** Martins-Taylor, K., and Xu, R.H. (2012). Concise review: Genomic stability of human induced pluripotent stem cells. *Stem Cells* **30**, 22-27.
- 103.** Mata, I.F., Wedemeyer, W.J., Farrer, M.J., Taylor, J.P., and Gallo, K.A. (2006). LRRK2 in Parkinson's disease: protein domains and functional insights. *Trends Neurosci* **29**, 286-293.
- 104.** McLelland, G.L., Lee, S.A., McBride, H.M., and Fon, E.A. (2016). Syntaxin-17 delivers PINK1/parkin-dependent mitochondrial vesicles to the endolysosomal system. *J Cell Biol* **214**, 275-291.
- 105.** Melton, C., Reuter, J.A., Spacek, D.V., and Snyder, M. (2015). Recurrent somatic mutations in regulatory regions of human cancer genomes. *Nat Genet* **47**, 710-716.
- 106.** Miesenbock, G., De Angelis, D.A., and Rothman, J.E. (1998). Visualizing secretion and synaptic transmission with pH-sensitive green fluorescent proteins. *Nature* **394**, 192-195.
- 107.** Miyaoka, Y., Chan, A.H., Judge, L.M., Yoo, J., Huang, M., Nguyen, T.D., Lizarraga, P.P., So, P.L., and Conklin, B.R. (2014). Isolation of single-base genome-edited human iPS cells without antibiotic selection. *Nat Methods* **11**, 291-293.
- 108.** Mizushima, N., and Klionsky, D.J. (2007). Protein turnover via autophagy: implications for metabolism. *Annu Rev Nutr* **27**, 19-40.
- 109.** Mizushima, N., Yamamoto, A., Hatano, M., Kobayashi, Y., Kabeya, Y., Suzuki, K., Tokuhi, T., Ohsumi, Y., and Yoshimori, T. (2001). Dissection of autophagosome formation using Apg5-deficient mouse embryonic stem cells. *J Cell Biol* **152**, 657-668.
- 110.** Mouton-Liger, F., Jacoupy, M., Corvol, J.C., and Corti, O. (2017). PINK1/Parkin-Dependent Mitochondrial Surveillance: From Pleiotropy to Parkinson's Disease. *Front Mol Neurosci* **10**, 120.
- 111.** Nalls, M.A., Pankratz, N., Lill, C.M., Do, C.B., Hernandez, D.G., Saad, M., DeStefano, A.L., Kara, E., Bras, J., Sharma, M., *et al.* (2014). Large-scale meta-analysis of genome-wide association data identifies six new risk loci for Parkinson's disease. *Nat Genet* **46**, 989-993.
- 112.** Narendra, D., Tanaka, A., Suen, D.F., and Youle, R.J. (2008). Parkin is recruited selectively to impaired mitochondria and promotes their autophagy. *J Cell Biol* **183**, 795-803.
- 113.** Nichols, J., and Smith, A. (2009). Naive and primed pluripotent states. *Cell Stem Cell* **4**, 487-492.
- 114.** Norrman, K., Fischer, Y., Bonnamy, B., Wolfhagen Sand, F., Ravassard, P., and Semb, H. (2010). Quantitative comparison of constitutive promoters in human ES cells. *PLoS One* **5**, e12413.
- 115.** Paisan-Ruiz, C., Guevara, R., Federoff, M., Hanagasi, H., Sina, F., Elahi, E., Schneider, S.A., Schwingenschuh, P., Bajaj, N., Emre, M., *et al.* (2010). Early-onset L-dopa-responsive parkinsonism with pyramidal signs due to ATP13A2, PLA2G6, FBXO7 and spatacsin mutations. *Mov Disord* **25**, 1791-1800.
- 116.** Paisan-Ruiz, C., Jain, S., Evans, E.W., Gilks, W.P., Simon, J., van der Brug, M., Lopez de Munain, A., Aparicio, S., Gil, A.M., Khan, N., *et al.* (2004). Cloning of the gene containing mutations that cause PARK8-linked Parkinson's disease. *Neuron* **44**, 595-600.
- 117.** Pankratz, N., Beecham, G.W., DeStefano, A.L., Dawson, T.M., Doheny, K.F., Factor, S.A., Hamza, T.H., Hung, A.Y., Hyman, B.T., Iverson, A.J., *et al.* (2012). Meta-analysis of Parkinson's disease: identification of a novel locus, RIT2. *Ann Neurol* **71**, 370-384.
- 118.** Pankratz, N., Wilk, J.B., Latourelle, J.C., DeStefano, A.L., Halter, C., Pugh, E.W., Doheny, K.F., Gusella, J.F., Nichols, W.C., Foroud, T., *et al.* (2009). Genomewide association study for susceptibility genes contributing to familial Parkinson disease. *Hum Genet* **124**, 593-605.

- 119.** Paquet, D., Kwart, D., Chen, A., Sproul, A., Jacob, S., Teo, S., Olsen, K.M., Gregg, A., Noggle, S., and Tessier-Lavigne, M. (2016). Efficient introduction of specific homozygous and heterozygous mutations using CRISPR/Cas9. *Nature* 533, 125-129.
- 120.** Pickrell, A.M., and Youle, R.J. (2015). The roles of PINK1, parkin, and mitochondrial fidelity in Parkinson's disease. *Neuron* 85, 257-273.
- 121.** Poillet-Perez, L., Despouy, G., Delage-Mourroux, R., and Boyer-Guittaut, M. (2015). Interplay between ROS and autophagy in cancer cells, from tumor initiation to cancer therapy. *Redox Biol* 4, 184-192.
- 122.** Polymeropoulos, M.H., Lavedan, C., Leroy, E., Ide, S.E., Dehejia, A., Dutra, A., Pike, B., Root, H., Rubenstein, J., Boyer, R., *et al.* (1997). Mutation in the alpha-synuclein gene identified in families with Parkinson's disease. *Science* 276, 2045-2047.
- 123.** Proukakis, C., Dudzik, C.G., Brier, T., MacKay, D.S., Cooper, J.M., Millhauser, G.L., Houlden, H., and Schapira, A.H. (2013). A novel alpha-synuclein missense mutation in Parkinson disease. *Neurology* 80, 1062-1064.
- 124.** Ramirez, A., Heimbach, A., Grundemann, J., Stiller, B., Hampshire, D., Cid, L.P., Goebel, I., Mubaidin, A.F., Wriekat, A.L., Roeper, J., *et al.* (2006). Hereditary parkinsonism with dementia is caused by mutations in ATP13A2, encoding a lysosomal type 5 P-type ATPase. *Nat Genet* 38, 1184-1191.
- 125.** Ran, F.A., Hsu, P.D., Lin, C.Y., Gootenberg, J.S., Konermann, S., Trevino, A.E., Scott, D.A., Inoue, A., Matoba, S., Zhang, Y., *et al.* (2013). Double nicking by RNA-guided CRISPR Cas9 for enhanced genome editing specificity. *Cell* 154, 1380-1389.
- 126.** Reinhardt, P., Glatza, M., Hemmer, K., Tsytsyura, Y., Thiel, C.S., Hoing, S., Moritz, S., Parga, J.A., Wagner, L., Bruder, J.M., *et al.* (2013). Derivation and expansion using only small molecules of human neural progenitors for neurodegenerative disease modeling. *PLoS One* 8, e59252.
- 127.** Requejo-Aguilar, R., Lopez-Fabuel, I., Fernandez, E., Martins, L.M., Almeida, A., and Bolanos, J.P. (2014). PINK1 deficiency sustains cell proliferation by reprogramming glucose metabolism through HIF1. *Nat Commun* 5, 4514.
- 128.** Rizzo, M.A., Davidson, M.W., and Piston, D.W. (2009). Fluorescent protein tracking and detection: applications using fluorescent proteins in living cells. *Cold Spring Harb Protoc* 2009, pdb top64.
- 129.** Roosen, D.A., and Cookson, M.R. (2016). LRRK2 at the interface of autophagosomes, endosomes and lysosomes. *Mol Neurodegener* 11, 73.
- 130.** Ruby, K.M., and Zheng, B. (2009). Gene targeting in a HUES line of human embryonic stem cells via electroporation. *Stem Cells* 27, 1496-1506.
- 131.** Ryan, S.D., Dolatabadi, N., Chan, S.F., Zhang, X., Akhtar, M.W., Parker, J., Soldner, F., Sunico, C.R., Nagar, S., Talantova, M., *et al.* (2013). Isogenic human iPSC Parkinson's model shows nitrosative stress-induced dysfunction in MEF2-PGC1alpha transcription. *Cell* 155, 1351-1364.
- 132.** Saad, M., Lesage, S., Saint-Pierre, A., Corvol, J.C., Zelenika, D., Lambert, J.C., Vidailhet, M., Mellick, G.D., Lohmann, E., Durif, F., *et al.* (2011). Genome-wide association study confirms BST1 and suggests a locus on 12q24 as the risk loci for Parkinson's disease in the European population. *Hum Mol Genet* 20, 615-627.
- 133.** Sankaranarayanan, S., De Angelis, D., Rothman, J.E., and Ryan, T.A. (2000). The use of pHluorins for optical measurements of presynaptic activity. *Biophys J* 79, 2199-2208.

- 134.** Sargsyan, A., Cai, J., Fandino, L.B., Labasky, M.E., Forostyan, T., Colosimo, L.K., Thompson, S.J., and Graham, T.E. (2015). Rapid parallel measurements of macroautophagy and mitophagy in mammalian cells using a single fluorescent biosensor. *Sci Rep* 5, 12397.
- 135.** Satake, W., Nakabayashi, Y., Mizuta, I., Hirota, Y., Ito, C., Kubo, M., Kawaguchi, T., Tsunoda, T., Watanabe, M., Takeda, A., *et al.* (2009). Genome-wide association study identifies common variants at four loci as genetic risk factors for Parkinson's disease. *Nat Genet* 41, 1303-1307.
- 136.** Seaman, M.N. (2004). Cargo-selective endosomal sorting for retrieval to the Golgi requires retromer. *J Cell Biol* 165, 111-122.
- 137.** Shaner, N.C., Steinbach, P.A., and Tsien, R.Y. (2005). A guide to choosing fluorescent proteins. *Nat Methods* 2, 905-909.
- 138.** Sharma, M., Ioannidis, J.P., Aasly, J.O., Annesi, G., Brice, A., Bertram, L., Bozi, M., Barcikowska, M., Crosiers, D., Clarke, C.E., *et al.* (2012a). A multi-centre clinico-genetic analysis of the VPS35 gene in Parkinson disease indicates reduced penetrance for disease-associated variants. *J Med Genet* 49, 721-726.
- 139.** Sharma, M., Ioannidis, J.P., Aasly, J.O., Annesi, G., Brice, A., Van Broeckhoven, C., Bertram, L., Bozi, M., Crosiers, D., Clarke, C., *et al.* (2012b). Large-scale replication and heterogeneity in Parkinson disease genetic loci. *Neurology* 79, 659-667.
- 140.** Sheerin, U.M., Charlesworth, G., Bras, J., Guerreiro, R., Bhatia, K., Foltynie, T., Limousin, P., Silveira-Moriyama, L., Lees, A., and Wood, N. (2012). Screening for VPS35 mutations in Parkinson's disease. *Neurobiol Aging* 33, 838 e831-835.
- 141.** Shen, Y., Rosendale, M., Campbell, R.E., and Perrais, D. (2014). pHuji, a pH-sensitive red fluorescent protein for imaging of exo- and endocytosis. *J Cell Biol* 207, 419-432.
- 142.** Shiina, T., Ota, M., Shimizu, S., Katsuyama, Y., Hashimoto, N., Takasu, M., Anzai, T., Kulski, J.K., Kikkawa, E., Naruse, T., *et al.* (2006). Rapid evolution of major histocompatibility complex class I genes in primates generates new disease alleles in humans via hitchhiking diversity. *Genetics* 173, 1555-1570.
- 143.** Silva, L.P., Lorenzi, P.L., Purwaha, P., Yong, V., Hawke, D.H., and Weinstein, J.N. (2013). Measurement of DNA concentration as a normalization strategy for metabolomic data from adherent cell lines. *Anal Chem* 85, 9536-9542.
- 144.** Simon-Sanchez, J., van Hilten, J.J., van de Warrenburg, B., Post, B., Berendse, H.W., Arepalli, S., Hernandez, D.G., de Bie, R.M., Velseboer, D., Scheffer, H., *et al.* (2011). Genome-wide association study confirms extant PD risk loci among the Dutch. *Eur J Hum Genet* 19, 655-661.
- 145.** Sinha, S., and Chen, J.K. (2006). Purmorphamine activates the Hedgehog pathway by targeting Smoothened. *Nat Chem Biol* 2, 29-30.
- 146.** Skylaki, S., Hilsenbeck, O., and Schroeder, T. (2016). Challenges in long-term imaging and quantification of single-cell dynamics. *Nat Biotechnol* 34, 1137-1144.
- 147.** Smukler, S.R., Runciman, S.B., Xu, S., and van der Kooy, D. (2006). Embryonic stem cells assume a primitive neural stem cell fate in the absence of extrinsic influences. *J Cell Biol* 172, 79-90.
- 148.** Snapp, E.L. (2009). Fluorescent proteins: a cell biologist's user guide. *Trends Cell Biol* 19, 649-655.
- 149.** Soldner, F., Laganieri, J., Cheng, A.W., Hockemeyer, D., Gao, Q., Alagappan, R., Khurana, V., Golbe, L.I., Myers, R.H., Lindquist, S., *et al.* (2011). Generation of isogenic pluripotent stem cells differing exclusively at two early onset Parkinson point mutations. *Cell* 146, 318-331.

- 150.** Solmaz, S.R., and Hunte, C. (2008). Structure of complex III with bound cytochrome c in reduced state and definition of a minimal core interface for electron transfer. *J Biol Chem* **283**, 17542-17549.
- 151.** Steger, M., Tonelli, F., Ito, G., Davies, P., Trost, M., Vetter, M., Wachter, S., Lorentzen, E., Duddy, G., Wilson, S., *et al.* (2016). Phosphoproteomics reveals that Parkinson's disease kinase LRRK2 regulates a subset of Rab GTPases. *Elife* **5**.
- 152.** Su, Y.C., and Qi, X. (2013). Inhibition of excessive mitochondrial fission reduced aberrant autophagy and neuronal damage caused by LRRK2 G2019S mutation. *Hum Mol Genet* **22**, 4545-4561.
- 153.** Sun, F., Huo, X., Zhai, Y., Wang, A., Xu, J., Su, D., Bartlam, M., and Rao, Z. (2005). Crystal structure of mitochondrial respiratory membrane protein complex II. *Cell* **121**, 1043-1057.
- 154.** Tabuchi, M., Yanatori, I., Kawai, Y., and Kishi, F. (2010). Retromer-mediated direct sorting is required for proper endosomal recycling of the mammalian iron transporter DMT1. *J Cell Sci* **123**, 756-766.
- 155.** Takahashi, K., Tanabe, K., Ohnuki, M., Narita, M., Ichisaka, T., Tomoda, K., and Yamanaka, S. (2007). Induction of pluripotent stem cells from adult human fibroblasts by defined factors. *Cell* **131**, 861-872.
- 156.** Takahashi, K., and Yamanaka, S. (2006). Induction of pluripotent stem cells from mouse embryonic and adult fibroblast cultures by defined factors. *Cell* **126**, 663-676.
- 157.** Takashima, Y., Guo, G., Loos, R., Nichols, J., Ficz, G., Krueger, F., Oxley, D., Santos, F., Clarke, J., Mansfield, W., *et al.* (2014). Resetting transcription factor control circuitry toward ground-state pluripotency in human. *Cell* **158**, 1254-1269.
- 158.** Takeshige, K., Baba, M., Tsuboi, S., Noda, T., and Ohsumi, Y. (1992). Autophagy in yeast demonstrated with proteinase-deficient mutants and conditions for its induction. *J Cell Biol* **119**, 301-311.
- 159.** Tang, F.L., Liu, W., Hu, J.X., Erion, J.R., Ye, J., Mei, L., and Xiong, W.C. (2015). VPS35 Deficiency or Mutation Causes Dopaminergic Neuronal Loss by Impairing Mitochondrial Fusion and Function. *Cell Rep* **12**, 1631-1643.
- 160.** Tanida, I., Ueno, T., and Uchiyama, Y. (2014). A super-ecliptic, pHluorin-mKate2, tandem fluorescent protein-tagged human LC3 for the monitoring of mammalian autophagy. *PLoS One* **9**, e110600.
- 161.** Theunissen, T.W., Powell, B.E., Wang, H., Mitalipova, M., Faddah, D.A., Reddy, J., Fan, Z.P., Maetzel, D., Ganz, K., Shi, L., *et al.* (2014). Systematic identification of culture conditions for induction and maintenance of naive human pluripotency. *Cell Stem Cell* **15**, 471-487.
- 162.** Tooze, S.A., and Yoshimori, T. (2010). The origin of the autophagosomal membrane. *Nat Cell Biol* **12**, 831-835.
- 163.** Tsukamoto, S., Kuma, A., Murakami, M., Kishi, C., Yamamoto, A., and Mizushima, N. (2008). Autophagy is essential for preimplantation development of mouse embryos. *Science* **321**, 117-120.
- 164.** Valastyan, J.S., and Lindquist, S. (2014). Mechanisms of protein-folding diseases at a glance. *Dis Model Mech* **7**, 9-14.
- 165.** Valente, E.M., Abou-Sleiman, P.M., Caputo, V., Muqit, M.M., Harvey, K., Gispert, S., Ali, Z., Del Turco, D., Bentivoglio, A.R., Healy, D.G., *et al.* (2004). Hereditary early-onset Parkinson's disease caused by mutations in PINK1. *Science* **304**, 1158-1160.
- 166.** Valente, E.M., Bentivoglio, A.R., Dixon, P.H., Ferraris, A., Ialongo, T., Frontali, M., Albanese, A., and Wood, N.W. (2001). Localization of a novel locus for autosomal recessive

early-onset parkinsonism, PARK6, on human chromosome 1p35-p36. *Am J Hum Genet* 68, 895-900.

167. van Duijn, C.M., Dekker, M.C., Bonifati, V., Galjaard, R.J., Houwing-Duistermaat, J.J., Snijders, P.J., Testers, L., Breedveld, G.J., Horstink, M., Sandkuijl, L.A., *et al.* (2001). Park7, a novel locus for autosomal recessive early-onset parkinsonism, on chromosome 1p36. *Am J Hum Genet* 69, 629-634.

168. Veres, A., Gosis, B.S., Ding, Q., Collins, R., Ragavendran, A., Brand, H., Erdin, S., Cowan, C.A., Talkowski, M.E., and Musunuru, K. (2014). Low incidence of off-target mutations in individual CRISPR-Cas9 and TALEN targeted human stem cell clones detected by whole-genome sequencing. *Cell Stem Cell* 15, 27-30.

169. Vilarino-Guell, C., Wider, C., Ross, O.A., Dachsel, J.C., Kachergus, J.M., Lincoln, S.J., Soto-Ortolaza, A.I., Cobb, S.A., Wilhoite, G.J., Bacon, J.A., *et al.* (2011). VPS35 mutations in Parkinson disease. *Am J Hum Genet* 89, 162-167.

170. Wang, H., Sun, H.Q., Zhu, X., Zhang, L., Albanesi, J., Levine, B., and Yin, H. (2015). GABARAPs regulate PI4P-dependent autophagosome:lysosome fusion. *Proc Natl Acad Sci U S A* 112, 7015-7020.

171. Wang, X., Winter, D., Ashrafi, G., Schlehe, J., Wong, Y.L., Selkoe, D., Rice, S., Steen, J., LaVoie, M.J., and Schwarz, T.L. (2011). PINK1 and Parkin target Miro for phosphorylation and degradation to arrest mitochondrial motility. *Cell* 147, 893-906.

172. Ward, A.J., and Cooper, T.A. (2010). The pathobiology of splicing. *J Pathol* 220, 152-163.

173. Wirdefeldt, K., Gatz, M., Pawitan, Y., and Pedersen, N.L. (2005). Risk and protective factors for Parkinson's disease: a study in Swedish twins. *Ann Neurol* 57, 27-33.

174. Woodard, C.M., Campos, B.A., Kuo, S.H., Nirenberg, M.J., Nestor, M.W., Zimmer, M., Mosharov, E.V., Sulzer, D., Zhou, H., Paull, D., *et al.* (2014). iPSC-derived dopamine neurons reveal differences between monozygotic twins discordant for Parkinson's disease. *Cell Rep* 9, 1173-1182.

175. Ying, Q.L., Wray, J., Nichols, J., Battle-Morera, L., Doble, B., Woodgett, J., Cohen, P., and Smith, A. (2008). The ground state of embryonic stem cell self-renewal. *Nature* 453, 519-523.

176. Yoshida, K., Taga, T., Saito, M., Suematsu, S., Kumanogoh, A., Tanaka, T., Fujiwara, H., Hirata, M., Yamagami, T., Nakahata, T., *et al.* (1996). Targeted disruption of gp130, a common signal transducer for the interleukin 6 family of cytokines, leads to myocardial and hematological disorders. *Proc Natl Acad Sci U S A* 93, 407-411.

177. Yoshikawa, S., Shinzawa-Itoh, K., Nakashima, R., Yaono, R., Yamashita, E., Inoue, N., Yao, M., Fei, M.J., Libeu, C.P., Mizushima, T., *et al.* (1998). Redox-coupled crystal structural changes in bovine heart cytochrome c oxidase. *Science* 280, 1723-1729.

178. Yu, J., and Thomson, J.A. (2008). Pluripotent stem cell lines. *Genes Dev* 22, 1987-1997.

179. Yu, W., Sun, Y., Guo, S., and Lu, B. (2011). The PINK1/Parkin pathway regulates mitochondrial dynamics and function in mammalian hippocampal and dopaminergic neurons. *Hum Mol Genet* 20, 3227-3240.

180. Yusa, K., Zhou, L., Li, M.A., Bradley, A., and Craig, N.L. (2011). A hyperactive piggyBac transposase for mammalian applications. *Proc Natl Acad Sci U S A* 108, 1531-1536.

181. Zarranz, J.J., Alegre, J., Gomez-Esteban, J.C., Lezcano, E., Ros, R., Ampuero, I., Vidal, L., Hoenicka, J., Rodriguez, O., Atares, B., *et al.* (2004). The new mutation, E46K, of alpha-synuclein causes Parkinson and Lewy body dementia. *Ann Neurol* 55, 164-173.

182. Zavodszky, E., Seaman, M.N., Moreau, K., Jimenez-Sanchez, M., Breusegem, S.Y., Harbour, M.E., and Rubinsztein, D.C. (2014). Mutation in VPS35 associated with Parkinson's disease impairs WASH complex association and inhibits autophagy. *Nat Commun* 5, 3828.

- 183.** Zhang, F., and Lupski, J.R. (2015). Non-coding genetic variants in human disease. *Hum Mol Genet* 24, R102-110.
- 184.** Zhu, J., Vinothkumar, K.R., and Hirst, J. (2016). Structure of mammalian respiratory complex I. *Nature* 536, 354-358.
- 185.** Zimprich, A., Benet-Pages, A., Struhal, W., Graf, E., Eck, S.H., Offman, M.N., Haubenberger, D., Spielberger, S., Schulte, E.C., Lichtner, P., *et al.* (2011). A mutation in VPS35, encoding a subunit of the retromer complex, causes late-onset Parkinson disease. *Am J Hum Genet* 89, 168-175.
- 186.** Zimprich, A., Biskup, S., Leitner, P., Lichtner, P., Farrer, M., Lincoln, S., Kachergus, J., Hulihan, M., Uitti, R.J., Calne, D.B., *et al.* (2004). Mutations in LRRK2 cause autosomal-dominant parkinsonism with pleomorphic pathology. *Neuron* 44, 601-607.

謝辭

Acknowledgment

This thesis is based on material contained in the following scholarly papers. 本博士論文は以下の学術論文に含まれる内容に基づいている。

著者名: **Jonathan Arias-Fuenzalida**, Javier Jarazo, Xiaobing Qing, Jonas Walter, Gemma Gomez-Giro, Sarah Louise Nickels, Holm Zaehres, Hans Robert Schöler & Jens Christian Schwamborn

題目: FACS を利用した CRISPR/Cas9 によるゲノム編集はパーキンソン病モデリングを容易にする

FACS assisted CRISPR-Cas9 genome editing facilitates Parkinson's disease modeling

論文誌: Stem Cell Reports, 巻 9 号 5 ページ 1-9, 年: 2017.

I would like to thank Prof. Yonehara and Prof. Hejna for their academic support and valuable feedback. I would like to acknowledge Prof. Berger, Prof. Bolognin and Prof. Hejna for feedback on the scientific articles. I would like to acknowledge Dr. Maeda, Dr. Barbuti and Dr. Wasner for their scientific feedback. This work was possible thanks to the scientific mentoring and guidance of Prof. Schwamborn. My studies were partially supported by the G30 Kyoto university tuition fee scholarship, and partially by the doctoral Chile government scholarship.

